Coherent Backscatter Enhancement from Finite Sized Aggregations of Scatterers

By

Adaleena Mookerjee

A dissertation submitted in partial fulfillment
of the requirements of the degree of
Doctor of Philosophy
(Mechanical Engineering)
in the University of Michigan
2017

Doctoral Committee:

Professor David R. Dowling, Chair
Professor Liliana Borcea
Professor Charles R. Doering
Professor Karl Grosh
Assistant Professor Eric Johnsen

Adaleena Mookerjee

adaleena@umich.edu

ORCID iD: 0000-0003-0808-1514

Dedication

Success is the ability to move on from failures with dignity and grace…

In loving memory of Shibani Ghosal and Jatilcoomar Mookerjee

ACKNOWLEDGEMENTS

I would like to start by expressing my sincere and heartfelt gratitude to my advisor and professor, Dr. David R. Dowling for his caring and patient guidance on my research. His unflagging support, sustained motivation, continuous encouragement and tireless efforts throughout the course of my graduate studies have helped me reach this significant milestone of my career. Additionally, his commitment to excellence and perfection, and his detailed and meticulous feedback have been a source of inspiration and a guiding force in this journey as a researcher. I am also thankful to Professor Dowling for allowing me to spend a summer away at the prestigious Los Alamos National Laboratory in New Mexico to enrich my research interests and experience.

I would like to take this opportunity to sincerely thank my committee members, Professors Liliana Borcea, Charles Doering, Karl Grosh and Eric Johnsen. They have contributed immensely to my learning in and outside the classroom. I greatly appreciate their willingness to be a part of my committee and providing valuable input to my thesis. I would also like to thank Dr. Kelly Benoit-Bird for providing me with the data necessary to make the comparisons between actual fish schools and her help in adding some biological insights into this dissertation. Additionally, I thank the Office of Naval Research for their financial support in my academic ventures and Advanced Research Computing at the University of Michigan for providing me with the computational resources to successfully perform these simulations.

I am forever grateful to my family who sustained me throughout my academic venture, especially my parents, Purusottam and Aninda Mookerjee. Both of them have been a tremendous support system for me through the triumphs and travails of my graduate studies. Always a phone call away, dropping everything at hand, they were ready with their advice and encouragement. My father often counseled me with his own experiences, while he was as a Ph.D. student years ago – that helped me develop a spirit of resilience through this journey. I also would like to thank my uncle, Anjan Ghosal, for egging me on throughout to realize my goals and dreams, and for letting me escape to Florida for a break when Michigan was too cold. Special thanks also go to my special cheerleaders and advocates, my aunt Reena Ghosal and my cousins, Sunil and Saurav Ghosal. I am grateful to my grandparents, Sandhyarani Mookerjee, Sujit Ghosal and Manisha Ghosal, and thank them for their love, support and continual prayers for my success.

Over my school and college years, I have made many good friends who continue to support and encourage me in many ways. A special mention is in order for Sarah Smith and Becci Meador, from my Cornell days, who were there to talk to me at any time. Moreover, I wish to thank Caroline Berglund, Heidi Chen, Brenton Clamor, Eric Wolff and Kristen Lau for their friendship. At the University of Michigan, I would like to thank the upper level graduate students to whom I looked up to: Simo Makiharju, Shima Abadi, Harish Ganesh, Pooya Movahed and Max Radin and then my peers: Marc Henry de Frahan, Brandon Patterson, Joel Hartenberger, Louise Lu McCarroll, Brian Worthmann, T.J. Flynn, Alex Douglass, Laura Williamson, Matt Van Overloop, and Jane Kim. I would also like to gratefully acknowledge Emily Davidson and Nasser Afzali, my friends from high school, who have been there for me even after so many years.

Finally, I would like to remember two very important people in my life who, though no longer alive, have had a strong influence in shaping and achieving my goals. They are my grandfather, the Late Dr. Jatilcoomar Mookerjee, and my great grandmother the Late Shibani Ghosal. From them, I acquired two essential qualities needed for doctoral studies. My grandfather, Jatilcoomar Mookerjee, was instrumental in inculcating in me the love and pursuit of knowledge, while from my great grandmother, Shibani Ghosal, I imbibed the qualities of perseverance, courage and an understanding that at the end, success is indeed the ability to move on from failures with dignity and grace. To both of them I dedicate this fruit of my labor, my Ph.D. research.

Table of Contents

List of Tables

List of Figures

radius is larger, ka = 32, and the radii of the backscatter-equivalent hard and soft spheres are both ka = 39.7. These results suggest that an increase in the aggregation size for fixed dimensionless scattering strength and scatterer spacing yields an increase in the multiple scattering effects (a more prominent CBE peak). Consequently, the aggregation is larger than the backscatter-equivalent hard and soft spheres in (a), but this size relationship switches in (b). 89

Figure 4-11: Same as Fig. 4-10, except ka = 16, $k\sigma_s^{1/2}$ = 1.5 and the average spacing between scatterers ks is varied between (a) and (b). In (a), ks is 6.4, and the radii of the backscatter-equivalent hard and soft spheres are ka = 6.9 and 6.7, respectively. In (b), ks is 2.9, and the radii of the backscatter-equivalent hard and soft spheres are ka = 16.6 and 16.9, respectively. A decrease in ks leads to an increase in the multiple scattering (a more prominent CBE peak). Consequently, as in Fig. 6, the aggregation is larger than the backscatter-equivalent hard and soft spheres in (a), but this size relationship switches in (b). 90

Figure 4-12: Same as Fig. 4-10, except ka = 16, ks = 3.2, and the dimensionless scatterer strength $k\sigma_s^{1/2}$ is varied between (a) and (b). In (a), $k\sigma_s^{1/2}$ is 0.38, and the radii of the backscatter-equivalent hard and soft spheres are ka = 4.6 and 4.3, respectively. In (b), $k\sigma_s^{1/2}$ is 3.0, and the radii of the backscatter-equivalent hard and soft spheres are ka = 25.0 and 24.8, respectively. An increase in the dimensionless scatterer strength yields an increase in the multiple scattering effects (a more prominent CBE peak). Here again, the aggregation is larger than the backscatter-equivalent hard and soft spheres in (a), but this size relationship switches in (b). 91

Figure 4-13: Backscattering ratio $\left\langle |p_s(0)|^2 \right\rangle / |p_s(0)|^2_{ideal}$ vs. $(ka)^{1/3}(ks)^{-1}(k\sigma_s^{1/2})^{1/2}$ for 20 different parameter sets involving spherical aggregations (circles) and spheroidal aggregations (squares). The filled symbols indicate parameter sets where no discernable CBE peak was found. The

List of Appendices

Abstract

When sound is projected into the ocean, the backscattered signal may provide information about the object(s) from which the sound has scattered. When the backscattered sound comes from an aggregation of strong scatterers, such as a school of fish at their swim bladder resonance frequency, a phenomenon known as the Coherent Backscatter Enhancement (CBE) may occur and this may aid in discriminating fish schools from other scatterers in the ocean water column. When CBE occurs, the addition of the in-phase path pairs enhances the scattered field by as much as a factor of two in the direction opposite to that of the incident wave. This thesis describes the results obtained from simulating aggregations of randomly placed omnidirectional point scatterers ($ka_s << 1$, where k = wave number of the illuminating wave and a_s = effective radius of the scatterers) using the Foldy (1945) multiple scattering equations and the conditions under which CBE may occur in the free space.

To ensure that the Foldy (1945) equations are implemented correctly, simulations are first verified and validated. The verification tasks include ensuring that the phasing of the scattering from a linear array of scatterers is correct and using the effective medium theory approximation also given in Foldy (1945). In both of the verification tests, the agreement between simulation and provided formulae is excellent. The validation was done by first ensuring that energy is conserved for the aggregation of scatterers. Here, the multiple scattering effects were gradually

increased by decreasing the average spacing between the scatterers and by increasing a scatterer's strength. In all cases, energy was conserved with numerical error up to $1/6^{th}$ of the

power incident on a single scatterer. The second test was through the replication of near field optics (Wolf et al., 1988) and acoustics (Bayer and Niederdränk, 1993) experiments. In both these experiments, a semi-infinite scattering medium is considered. After taking into account the differences in the resolution of the receivers and the sizes of the aggregation using a coherence function, the comparisons were good: the near field optics experiment replication yielded an enhancement of 1.030±0.005 via simulation (1.034 from experiment) and the near field acoustics experiment replication yielded an enhancement of 1.5 (1.5 from experiment).

In addition, simulations of far field CBE from spherical aggregations of scatterers are presented and compared with backscattering from ideal spherical scatterers. These results indicate that for high multiple scattering effects, the corresponding backscatter equivalent ideal spherical scatterer may be bigger than the spherical aggregation itself. Interestingly, a spherical aggregation consisting of strong scatterers with radius of ka = 32 may yield a backscattered equivalent sphere up to ka = 53.

To compare the CBE simulations with actual acoustic backscatter measurements from fish schools, the probability density function of the backscattered returns from aggregations of scatterers, a school of rockfish and small pelagics[1] are also considered as a method of classification. For an aggregation of scatterers, the distribution may be Rayleigh, using a $|p|/\langle|p|^2\rangle^{1/2}$ normalization. In the *in situ* measurements, the distribution is non-Rayleigh and instead, a Lorentzian-weighted smear of Rayleigh distributions is proposed for the backscatter returns from the schools considered.

[1] *In situ* measurements provided by Dr. Kelly Benoit-Bird of the Monterey Bay Aquarium Research Institute.

CHAPTER 1

Introduction

The acoustic signal from an active sonar source traveling in an underwater medium may be backscattered by targets, known environmental features, and ocean clutter. Scattering from unknown targets and clutter is easily confused and this leads to difficulties in sensing the acoustic environment. Typically, clutter consists of rough surface scattering from the ocean's surface or bottom, seaweed and other forms of plant life, and marine animals, particularly fish (Abraham et al., 2011). In the case of scattering from marine life, sound may be scattered in all different directions and statistical information from fish schools can be gathered from the active sonar returns in the backscattered direction. For aggregations of very strong scatterers, the interaction of sound bouncing between individual scatterers may result in an added enhancement in the intensity of the backscattered sound called the Coherent Backscatter Enhancement (CBE) (Akkermans et al., 1986). Knowledge of the scattering from marine life can be useful for remote sensing. In military applications, an understanding of the scattering behavior can aid in locating and detecting obstacles (Lurton, 2002) and targets (Zhu et al., 2005). Additionally, locations of the sources of nutrients for the plant life in the ocean can be obtained using acoustic backscattering from the biologics (Proni et al., 2008). Particularly, knowledge of the scattering behavior in the water column could help in environmental monitoring of the ocean and also help with fish population surveys (Jain et al., 2014, Andrews et al., 2011).

In order to classify and locate objects using remote sensing, there are two types of sonar which could be utilized. The first possibility is through the use of passive systems. In passive sonar, the system is only listening for receiving sounds from a target that radiates sound or that scatters sound from another source. In this case, hydrophones are stationed at known locations to listen to the sound coming from the target. The second case is to use an active sonar system, where a signal is transmitted and the incident signal is reflected from the target (Lurton, 2002). Here, the sending and the listening positions could be co-located (monostatic active sonar) or separated (bistatic active sonar) (Urick, 1983).

The work in this dissertation develops an understanding of the scattering characteristics that could be observed in active sonar signal returns from aggregations of pelagic fish to aid in the development of remote sensing techniques for the U.S. Navy. Such fish commonly have a gas-filled swim bladder having a non-negligible acoustic scattering cross section. Aside from pelagic fish in the underwater environment, there are also nonpelagic fish, other organisms, plant life, rough surfaces, and volume inhomogeneities in the ocean's water column and bottom. All of these may cause some amount of acoustic scattering, too. Consequently, active sonar returns can come from nearly any object or direction in the ocean environment. Additionally, this research may also provide information relevant to acoustic sampling of the fish populations (Benoit-Bird et al., 2013). Understanding backscattering from schools of fish may help with characterizing and classifying remote aggregations of marine life.

1.1: Fish Behavior and Model

In the underwater environment, fish typically travel in schools, or shoals, for protection against predators, for reducing the risk of being eaten, for spawning and for foraging for food

(Pitcher, 1993, Partridge, 1982). Typically shoals are in spherical or spheroidal geometries, depending on the fish school and the school behavior (Partridge, 1980). Similar findings were also seen by Hemelrijk and Hildenbrandt (2012), who also saw that fish schools tend to be in spheroidal or oblong geometries, and Misund (1993), who used a downward looking echosounder to experimentally observe the geometries of schools of herring, saithe and sprat. For this reason, since the primary aim in this research is to simulate schools of fish, spherical and spheroidal aggregation geometries are predominately considered, though rectangular and cubical aggregations are utilized in Chapter 3 for verification and validation.

Certain kinds of pelagic fish have swim bladders, which is a gas filled organ which helps fish remain neutrally buoyant. It has also been found that the swim bladder has acoustical properties. In 1980, Foote found that the acoustic scattering from the swim bladder produces about 90-95% of measured fish target strengths. Through both measurement and simulation, Reeder et al. (2004) found that the maximum scattering from a species of fish occur from the swim bladder and the skull. A similar finding was also observed by Jørgensen (2002), who found that the acoustic target strength for capelin depended on the length of the swim bladder. Consequently, and for simplicity, in this research effort the fish's swim-bladder is solely considered to represent the fish since it is the primary contributor in the scattering.

Since a fish's swim bladder consists of a volume of gas, it can be modeled as a bubble. In 1978, Love added a viscous outer shell to enclose the bubble and saw that at low frequencies, the shell does not contribute much scattering. Thus, fish flesh viscosity is not directly included into the work discussed in this thesis. Instead, in Chapter 5, it is included as the frequency dependent scattering and extinction cross sections. At an illuminating acoustic frequency near resonance in water, a gas bubble's volume may under large-amplitude damped oscillations. However, the

acoustic wavelength at resonance is much larger than the bubble's radius. Therefore, the scattered radiation is omnidirectional (Devin, 1959). Consequently, when sound illuminates a bubble, it could travel past the bubble without interaction or either be scattered or absorbed or both (Foldy, 1945). The portion of the sound that is scattered and absorbed is characterized by the extinction cross section, defined as the area of the incident field that carries the same acoustic power as that scattered and absorbed by a scatterer. The extinction cross section of an individual bubble in water is a function of the incident sound frequency, bubble size and the properties (density, surface tension, thermal conductivity and viscosity) of the water (Kinsler et al., 2000). While in Chapters 3, 4, 6 and part of 5, it is assumed that the scattering and extinction cross sections are equal, for the herring fish scattering simulations, the scattering and extinctions cross sections are based off the formula given in Love (1978). Therefore, they are not equal for those particular simulations.

In Chapter 5 of this thesis, omnidirectional point scatterers are considered with scattering and extinction cross sections which are that of the particular fish species using the forms of the Love (1978) model in Raveau and Feuillade (2015). These point scatterers are mainly arranged in aggregations which are in spherical and spheroidal geometries with an exclusion distance to account for the other anatomical features of the fish as well as the distance between fish in the school. It is assumed that the size of the swimbladder is much smaller than that of an acoustic wavelength.

1.2: Single Large Scatterer Model

In comparison to low-frequency scattering from a fish's swimbladder, the interaction between an incident acoustic wave of arbitrary frequency and a single scattering object is

potentially more complicated. Typically, an accurate model would require consideration of fluid-structure interaction via numerical techniques (Hou et al., 2012) or consideration of other effects such as surface or Franz waves through the use of the Watson transformation (Überall, 1985). Überall (1985) experimentally confirmed the equations to verify the physics scattering theory of solid elastic spheres and cylinders. Simpler techniques were also considered by van Bladel (1968) who studied an ideal spherical scatterer and neglected fluid structure interactions or any other waves impinging on it, aside from the acoustic wave. Pierce (2000) used the van Bladel (1968) equations, but assumed the wave number scaled radius to be much less than 1, $ka << 1$ and kept the first few terms in the series expansion. Additionally, Hay and Burling (1982) derived the equations for modeling a single large spherical scatterer with various different conditions pertinent to marine applications and compared the equations with experiment.

In this thesis, the equations from Morse and Ingard (1968) are considered to model a single large sphere to minimize the complexities of the scattering behavior and runtime. First, the van Bladel (1968) spheres with zero pressure gradient (hard) and pressure release (soft) boundary conditions are considered. These spheres are considered to compare the returns from a school of fish with a large bubble or manmade spherical object without considering fluid-structure interactions or expansion or contraction of the bubbles. The sizes of the sphere range from $ka = 12$ to 32 and, therefore, the form of the equations from Pierce (2000) is insufficient to model the single large scatterer. This sphere is oriented in the same configuration as the spherical aggregation of scatterers and then the far field radial intensity is approximated as a pressure magnitude squared using a far field ($ka^2/R << 1$, where k is the incident wave number, a is the radius of the aggregation and R is the distance the aggregation is from the receivers) receiving ring. In Chapter 4, the backscattered pressure magnitude squared from the sphere is matched

with the mean square pressure for an aggregation of scatterers. Second, a theoretical comparison with the sphere considered in Hahn (2007) is also performed in Chapter 4 for an aggregation of scatterers. This was done by considering the impedance boundary condition in Morse and Ingard (1968). Foldy's (1945) effective medium theory was used to determine the effective wave number, k_e, effective sound speed, c_e, for an aggregation of scatterers. These values, along with the effective density, ρ_e, were used to model a single sphere with properties k_e, ρ_e and c_e. In Chapter 4, comparisons are made between this ideal sphere as the magnitude backcatterered pressure, $|p|$, with an aggregation of scatterers as the magnitude of the average backscattered pressure, $|\langle p \rangle|$. The comparisons were done in dB and plotted as a function of the small parameter, $\left|4\pi(kg_1)^2/(ks)^3\right| << 1$, where (kg_1) is the wave number scaled scattering coefficient of each scatterer and (ks) is the dimensionless average spacing between scatterers. This small parameter was provided in Hahn (2007), though originally obtained in Frisch (1968). Additionally, in Chapter 5, the van Bladel (1968) equations are again considered by matching the aggregation radius with that of the hard and soft sphere.

1.3: Multiple Scattering

When an incident wave interacts with a scattering object, a portion of the incident wave scatters away from the object. When an aggregation of $N >> 1$ scatterers is considered, each scatterer is still illuminated by the incident wave, but now the scattered waves from all the other scatterers also impinge on each scatterer. When the scattered illumination is comparable to (or larger than) that of the incident field, multiple scattering effects are important. In this case, the overall scattering interaction is more complicated and can differ significantly from the field produced by a superposition of N isolated scatterers. In 1945, Foldy derived exact multiple

scattering equations that represent all scattering interactions between N omnidirectional point scatterers (Chapter 2 discusses the mathematical detail of the equations). To generate a solution, the equations are solved for the scattered field from each scatterer in the aggregation individually, excluding the scatterer itself and then for the field at the location of interest. These equations are particularly advantageous in that they work for any kind of incident wave that is a solution of the Helmholtz equation. The disadvantage of using these equations is that it typically involves an $N \times N$ matrix inversion that can be computationally taxing when N is large. In order to avoid this inversion, Foldy (1945) developed an approximate effective medium theory, which neglects some higher order scattering. This effective medium theory formula is briefly considered in Chapter 3 for verification purposes and in Chapter 4, in conjunction with modeling the Hahn (2007) sphere. Depending on the application and kind of wave considered, different studies have modified the formula modeling the effective medium theory accordingly (Ye and Ding, 1995). This was done as early as 1951 by Lax, who modified the effective medium theory for quantum waves and neutron scattering, in 1961 by Waterman and Truell, for electromagnetics and also in acoustics by Twersky in 1957, who considered scattering from rough surfaces (Lax, 1951, Lax 1952, Waterman and Truell, 1961, Twersky, 1957). While the effective medium theory is a way to obtain the configurational average of the pressure field from lower order scattering, in order to simulate the coherent backscatter enhancement, all orders of scattering is needed. Thus, much of this thesis predominately uses the exact form of the multiple scattering equations, though there are sections in Chapters 3 and 4, which utilize the effective medium theory, but are not used to simulate the coherent backscatter enhancement. Additionally, the parameters have been selected such that the $N \times N$ matrix inversion is possible to perform

(average spacing between the scatterers, ks, ranging from around 2π to a little less than π, and dimensionless scattering strength, $k\sigma_s^{1/2}$, is less than $2\pi^{1/2}$).

Particularly, in acoustics, the Foldy (1945) equations have since been used depending on the setup and purpose. Most of the time, the effective medium theory version of the Foldy (1945) equations are utilized and are appropriately modified based on the application of interest. In 1982, Tsang et al. used the effective medium theory equations from Twersky (1957) and modified it to include corrections when the medium consists of discrete spherical scatterers (Tsang et al., 1982). Additionally, Henyey (1999) also employed a correction term for Ye and Ding's (1995) formulation for bubble clouds which Hahn (2007) also further modified. Aside from its use in bubbles, Foldy's effective medium theory and possible corrections were also used by Linton and Martin (2006) for solid spheres, by Norris and Conoir (2011) for developing corrections for random assemblages of cylindrical rods, and by Derode et al. (2006), which also considered rods as the scattering medium and compared experimental findings with the theoretical effective medium corrections. Additionally, Raveau and Feuillade (2016) also considered the effective medium theory for fish school scattering and compared it to the full form of the multiple scattering equations. Ye et al. (1996) also used the effective medium theory formulae to model fish schools for forward scattering. Similar approximations, though not the Foldy's effective medium theory, were also done by Stanton (1983) where expressions for wave-fish interactions were considered up to the second order echo. While Foldy's effective medium theory is briefly considered in Chapter 3 of this dissertation as a verification technique, in order to sufficiently simulate the statistics of a fish school, the full form of the Foldy (1945) multiple scattering equations is needed and this approach is pursued in this thesis.

The full form of the Foldy (1945) equations in bubble acoustics have been used by Feuillade (1995), where the Foldy (1945) equations where modified to include bubble properties such as density, bubble radius, damped resonant frequency, and ratio of gas specific heats. These equations have been used in conjunction with the Love (1978) model to consider schools of fish as well taking the fish flesh viscosity into account in the damping (Feuillade et al., 1996) to model structured cubical arrangements of fish. Since then, these equations have been used in Nero (1996) to simulate small oblate spheroidal schools of yellowfin tuna, which had an assumed wave number scaled effective swimbladder size ranging from $ka_s \sim 0.0075\text{-}0.3$ for the frequencies considered, in Alfaro et al. (2015) to analyze the statistics of the target strength of dynamic unspecified fish schools, and in Raveau and Feuillade (2015) to study the forward scattering behavior from collections of fish, particularly sardines ($ka_s \sim 0.04$ (Machias and Tsimenides 1995)). In Chapter 5, the Foldy (1945) equations are used along with the Love (1978) model, like Raveau and Feuillade (2015). However, the focus here is on backscattered sound.

To compare the theoretical and simulated scattering behavior from fish schools, results are often compared with in situ measurements. In 2006, Jaffe used a multi-angle sensing system to theoretically sense the size of the swimbladder of a fish. The derivations were implemented in simulation and were compared with the data provided in Foote (1985) for a 31.5 cm pollack fish ($ka_s \sim 1.1\text{-}3.3$ for the frequencies considered). In 2011, Andrews et al. used a statistical Monte-Carlo model to numerically simulate a 2006 Gulf of Maine Experiment with schools consisting of Atlantic herring ($ka_s \sim 0.0015\text{-}0.0035$). The work described in this thesis also utilizes Monte Carlo techniques to simulate schools of fish and in Chapter 5, a school of herring is simulated at varying ocean depths, though the effects of the ocean waveguide are neglected.

Additional *in situ* measurements have also been done to obtain information on the scattering from fish schools. In 2014, Jain et al. used an ocean acoustic waveguide remote sensing system (OAWRS) to sense Atlantic cod in the Gulf of Maine to estimate the extent of the scattering from the sea floor. Charef et al. (2010) performed acoustic measurements in the East China Sea to classify the groups of the fish via discriminant function analysis and artificial neural networks. Additionally, Benoit-Bird et al. (2013) also obtained volumetric scattering data from schools of pollock (ka_s ~ 3.3-36) and zooplankton to determine the location of pollock schools. While the work in this thesis is primarily focused on simulation, part of Chapter 6 is based on *in situ* echo-sounder measurements obtained in 2012 that include the natural variability of the fish schools.

1.4: Backscattering

When a plane wave illuminates a scatterer, the backscatter direction is the opposite of the incident wave propagation direction. In 1980, Foote derived the theory behind averaging target strength (backscattering cross section in dB) for fish schools and compared it with computational examples of cod, saithe and pollack at frequencies of 38 kHz and 120 kHz. Additionally, in 2003, Towler et al. simulated backscattering of walleye pollock (ka_s ~ 7.0-22) and capelin (ka_s ~ 0.8-2.5) using a Kirchoff-ray mode (KRM) model to predict the anatomy of the fish and the fish behavior. Using a similar approach, McClatchie and Ye (2000) also obtained the target strength for orange roughy fish and compared findings with *in situ* measurements, which is also done in Chapter 6 of this thesis, though probability distribution functions of normalized pressure magnitude squared in dB and normalized echo amplitude are considered. Additionally, Gorska and Ona (2003) also performed a similar study as McClatchie and Ye (2000) but with a deformed cylinder model from Stanton (1989) and Reeder et al. (2004) using KRM and a Fourier

matching model for alewife fish. The work herein also considers simulation though via the Foldy (1945) equations for a school of fish where the wave number scaled effective swim bladder radius is significantly less than 1.

Acoustic surveys have also been done which measured the backscattering from schools of fish as well. In 2003, Melvin et al. used multi and single beam sonar to obtain area and volumetric backscattering strength in dB for different pings for a herring fish school ($ka_s \sim 5.9$). Similarly, Kang et al. (2002) used volumetric backscattering strength and target strength as well to identify fish (primarily walleye pollock ($ka_s \sim 7.0$ and 22.0) and zooplankton for frequencies of 38 kHz and 120 kHz. Additionally, Yasuma et al. (2003) calculated target strength of different species of lanternfish (mainly $ka_s \sim 0.002$) with different swimbladder sizes. Lastly, Benoit-Bird et al. (2013) studied schools of walleye pollock ($ka_s \sim 3.3\text{-}36$) using volumetric scattering strength to determine the spatial heterogeneity. In Chapter 6 of this thesis, acoustic survey measurements of fish schools using volumetric scattering strength are considered to extend the distribution functions from the backscattered returns of an aggregation of scatterers obtained via simulations and factor in the natural variability of the fish schools in the water column. Unlike the aforementioned simulation models used to model backscattering from a fish, this thesis will discuss backscattering from fish schools via the Foldy (1945) equations, assuming that the wave number scaled effective swim bladder radius is significantly less than 1. Thus, the findings discussed in this document would be most applicable to the acoustic survey results obtained by Yasuma et al. (2003).

1.5: Coherent Backscatter Enhancement

The coherent backscatter enhancement (CBE) was first observed in the 1980s as an optics finding, notably by Kuga and Ishimaru in 1984 as an experimental study. Upon its finding, it was studied extensively by van Albada (1987, 1988), Wolf and Maret (1985), Akkermans et al. (1986, 1988) and Wolf et al. (1988). Gradually, the interest in CBE shifted over to acoustics with experimental studies done by Bayer and Niederdränk (1993) and Sakai et al. (1997).

In perfect backscatter, the incident wave number vector and the backscattered wave number vector are equal and opposite. In this situation, scattering paths within the scattering medium may be traced forward and backward by different portions of the single wave front so that wave pairs emanating from the scattering medium are in phase, and add coherently. When the scattering locations are random, different scattering paths lead to random phases and will be uncorrelated. However, in the precise backscatter direction, scattering path pairs are correlated leading to an intensity enhancement of up to a factor of two. This factor of two enhancement is known as the coherent backscatter enhancement (CBE) and has been observed in several different wave propagation applications in optics (Kuga and Ishimaru, 1984), acoustics (Sabra, 2010) and quantum mechanics (Jendrzejewski et al, 2012) in simulation (Weaver and Burkhardt, 1994, Margerin et al, 2001), experiments (Wolf and Maret, 1985, Wolf et al., 1988, Derode et al., 2005, Aubry et al., 2007, Lobkis and Weaver, 2008) and theory (Akkermans et al., 1986, Akkermans et al., 1988, Garnier and Sølna, 2008, de Hoop et al., 2012).

1. Optical Coherent Backscatter Enhancement

The study of the coherent backscatter enhancement originally started in optics in the 1980s and later transitioned over to acoustics in the mid 1990s. In 1984, Kuga and Ishimaru were

one of the first studies to consider experiments involving coherent backscattering using latex microspheres as scatterers illuminated with laser light. However, they found an enhancement of just 15%. Akkermans et al. (1988) later determined that this may have been due to the experimental resolution of the setup. Based on the Kuga and Ishimaru (1984) experimental setup, Wolf and Maret (1985) and Wolf et al. (1988) performed an experiment illuminating an aqueous solution of polystyrene spheres, resulting in an enhancement of a factor of 1.7 for varying diameter beads. These experiments are discussed in greater detail in Chapter 3 as part of a validation procedure for the simulations. Additional experiments were done by van Albada et al. (1987) and van Albada et al. (1988) where effects of anisotropy were considered in a finite slab, as well as polarization effects resulting when light is the incident wave. These two issues are not present in the acoustical coherent backscattering studied here.

Optical coherent backscatter enhancement was considered extensively by Akkermans et al. (1986) and Akkermans et al. (1988). A result in the Akkermans et al. (1986) paper provides a description of the CBE peak as a function of mean free path, l, incident wave number, k, and scattering angle, which they defined as θ (not to be confused with the polar angle, θ, which is the convention used in this dissertation). Akkermans et al. (1986) used this formula along with the experimental results from Wolf and Maret (1985) to compare experiment with theory. In the Akkermans et al. (1988) paper, this formula is described further and modified for absorption effects, varying scales and polarization. Like Akkermans et al. (1986) which compared a theoretical derivation to Wolf and Maret (1985), the work presented in Chapter 3 also considers the experiments from Wolf and Maret (1985) and Wolf et al. (1988), particularly the scattering medium. However, it considers the simulation techniques via the Foldy (1945) equations, instead of the Akkermans et al. (1986) formula.

Optical coherent backscatter enhancement simulations have been minimal. In 2002, Picard et al. used the Foldy-Lax equations via iterative techniques to predict backscattering for wheat canopies, which were modeled as cylinders. Like Picard et al. (2002), the Foldy-Lax equations are considered in this dissertation, but the actual matrix inversion is performed. Additionally, Eddowes et al. (1995) performed Monte Carlo simulations of biological tissues to obtain the angular dependence of intensity and compared it with Akkermans et al. (1986) for different indices of refraction. In this thesis, a similar approach is undertaken, though with acoustic scalar waves and omnidirectional point scatterers via the Foldy (1945) equations. While electromagnetics are not considered here, the simulations could certainly be extended to these applications. For this reason, all length scales have been rendered dimensionless by incident wave number, k, and pressure fields have been nondimensionalized by incident amplitude.

Though the work discussed in this dissertation involves acoustics, a significant portion of Chapter 3 focuses on optics as a part of the validation of the codes, particularly Wolf and Maret (1985), Wolf et al. (1988) and Akkermans et al. (1986). Here, the wave number scaled spacings and mean free paths are nominally matched to that of Wolf and Maret (1985) and Wolf et al. (1988) for the smallest sized beads considered by them. The results from this undertaking appear in Mookerjee and Dowling (2015).

2. Acoustical Coherent Backscatter Enhancement

Nearly ten years after one of the first optical CBE studies, CBE started to move into the field of acoustics. Bayer and Niederdränk (1993) experimentally found CBE with an enhancement of 1.5 using gravel stones and brass rods at a 2 MHz center frequency. As a part of the validation technique, this experiment is discussed in detail in Chapter 3. Since then, Sakai et

al. (1997) experimentally found acoustic coherent backscattering as well with polystyrene beads and showed Schlieren images of the phenomenon. Similarly, Tourin et al. (1997) also considered acoustic scattering from rods using a center frequency of 3.5 MHz and observed an enhancement of a factor of two. Other ultrasound experiments were done by Lobkis and Weaver (2008), which observed localization effects using ultrasound on a plate with dense multiple scatterers; by Larose et al. (2007), which considered a plate, an array of sources and a distant receiver; by Derode et al. (2005), which used CBE to characterize human trabeculas structure; and by Aubry et al. (2007), which used plane wave beamforming to find coherent backscattering from rods. In Chapter 3 of this thesis, like Aubry et al. (2007), a linear receiving array and plane wave beamforming is utilized. However, the scattering medium consists of omnidirectional point scatterers and not rods.

Coherent backscattering in acoustics has also been observed in cavities and waveguides, without the explicit presence of discrete scatterers. Sabra (2010) observed an enhancement at mid-frequencies (3-4 kHz) and saw a 3dB increase of the reverberation level in the exact backscatter direction from an experiment done in July 2004 in the ocean near Italy. Additionally, Gallot et al. (2011) considered coherent backscattering from cavities experimentally and numerically and studied the dependence of peak height with symmetry of the cavity and found the results to be positive. Another experimental study has been done in a seismological context by Larose et al. (2004), where the scattering medium includes geological inhomogeneities at a volcano, resulting in a backscatter enhancement of up to two for different frequency bands. While all these documented findings are interesting, the work in this thesis does not consider waveguides or cavities and instead focuses on the coherent backscatter enhancement and the

wave physics from an aggregation of many discrete scatterers only. Extension of the current effort to waveguides or cavities is suggested as a potential for future work.

Theoretical formulations of coherent backscattering in acoustics have also been provided. In 2008, Garnier and Sølna derived a general set of equations for random perturbations in an acoustic waveguide via a separation of scales technique and were able to mathematically show enhanced backscattering. Interestingly, in 1994, Weaver and Burkhardt (1994) proved theoretically and numerically that the potential exists that under some conditions an enhancement may exceed a factor of two and could be as high as three in reverberation rooms. A similar finding has also been seen and discussed in Chapter 3 of this thesis. Lastly, de Hoop et al. (2012) also considered backscattering enhancement using a waveguide which consists of three media for acoustic scalar surfaces. The waveguide occupied the region $z \in (z_i(\boldsymbol{x}),0)$. For $z > 0$ (top surface), the surrounding medium has a wave number of k_1 and density of 0 and on the bottom surface ($z \leq z_i(\boldsymbol{x})$), the surrounding medium has a wave number of k_0 and density of ρ_0. Inside the waveguide, the medium consists of a wave number of $k_1/(1+v_k(z, \boldsymbol{x}))$ and density ρ_1, where $v_k(z, \boldsymbol{x})$ is modeled as the medium fluctuations. Using these conditions, they were able to derive an expression for the enhanced backscattered intensity. In this thesis, an aggregation of omnidirectional scatterers is considered without the presence of a waveguide. An extension of the simulation capabilities to simulate an aggregation of omnidirectional point scatterers with an ocean wave guide is proposed as future work.

Simulation studies of acoustic coherent backscattering have been few. One of the aims of the work in this thesis is to show that acoustic coherent backscatter enhancement can be simulated via the Foldy (1945) equations. Aside from Weaver and Burkhardt (1994), which was discussed earlier, other simulation studies have been done in the seismological context or by

using simple geometries involving cavities. In 2011, Catheline et al. simulated 1D, 2D and 3D cavities and compared the simulated results with experiments. They, too, found that depending on the geometry and dimensions of the cavity, the intensity of enhancement can exceed a factor of two, even up to as high as 3.55. Via simulation, in this thesis, it is also shown that the enhancement can exceed a factor of two, possibly up to 3.5, depending on the simulation setup. However, in this thesis, this is shown with a scattering medium consisting of omnidirectional point scatterers and not through the use of a cavity or waveguide. Similarly, Margerin et al. (2001) also considered simulations, though in a seismological context via Monte Carlo simulations of random walks, and compared their findings with theory. They also found that the enhancement is up to a factor of two and plotted the enhancement over time for different ranges. The work discussed in this thesis also considers Monte Carlo simulations through the random generation of scatterer positions and repeatedly evaluating the Foldy (1945) equations to obtain the pressure.

In this thesis, Chapters 3 to 5 consider acoustic coherent backscatter enhancement using Monte Carlo simulations of the Foldy (1945) equations for finite sized aggregations of randomly placed omnidirectional point scatterers. In Chapter 3, simulations are validated by simulating existing optics and acoustics experiments (Wolf and Maret, 1985, Wolf et al., 1988, Bayer and Neiderdränk, 1993). Additionally, in Chapter 4, acoustic CBE is simulated for aggregations of scatterers with different spacings, sizes and strengths for single frequency signals. Lastly, in Chapter 5, a similar study is performed though with broadband pulses in frequency ranges which may be of interest to the US Navy.

1.6: Probability Distribution Function

In this thesis, two statistical techniques are considered in classifying schools of fish. Chapters 3-5 consider the coherent backscatter enhancement, which requires use the ensemble average of realizations for a wide range of angles, and Chapter 6 involves generating a probability distribution function using only the returns in the backscatter direction. While the work in this thesis is the first to show the distribution function using the Foldy (1945) equations, use of the probability distribution function in the backscattering returns from schools of fish has been of interest as early as the 1980s by Huang and Clay and has been considered as recently as 2014. In 1980, Huang and Clay studied the echo amplitude and target strength distributions for a single shiner fish suspended to a tether illuminated at a frequency of 220kHz ($ka_s \sim 6.5$). They found that the distribution of the echoes is Rayleigh and the target strength distribution is a product of exponentials. The normalized echo amplitude and the target strength are algebraically related. Thus, via Billingsley (1995) and the formula given in Huang and Clay (1980) for converting between probability distribution functions, this finding is not surprising. Additionally, in 1986, Stanton and Clay analyzed normalized echo (or backscattered pressure) amplitude ($|p|/<|p|^2>^{1/2}$) distributions which appeared Rayleigh or Ricean via downward looking sonar using frequencies of 3.5-200kHz of an unspecified fish type. Like Huang and Clay (1980), MacLennan and Menz (1996) also studied target strength distributions, though they considered distributions from of *Diplotaxodon spp*. fish (fish swimbladder volume information, unavailable) in Lake Malawi (as opposed to a fish tethered in a pool) at 120kHz frequency. In 2004, Stanton et al. considered acoustic backscattering at frequencies of 45-85kHz of zooplankton, perwinkle, alewife fish ($ka_s \sim 0.94$-1.8) and shrimp and siphonophore and studied the resulting statistics. It

was found that the distribution, though close to being Rayleigh, was actually non Rayleigh, depending on the orientation of the fish. Demer et al. (2009) performed an acoustic survey as well and observed a form of a Ricean distribution for rockfish at frequencies of 18, 38, 70, 120 and 200kHz (ka_s ~ 2.3-25.6). Like Demer et al. (2009), Chapter 6 of this thesis also considers rockfish at those frequencies as well, but considers a weighted continuous sum of Rayleigh distributions to describe the distribution of the normalized echo amplitude. Lastly, Stanton and Chu (2010) conducted acoustic surveys with different patches of herring fish schools using frequencies of 2-4kHz (ka_s ~ 0.006-0.12) and found that while the distribution is like Rayleigh for normalized echo amplitude, the actual fitted probability distribution is a mixture distribution. This is in agreement with the finding in Chapter 6 when *in situ* measurements were considered in the ocean for rockfish and small pelagics. However, unlike the aforementioned studies, Chapter 6 uses a continuous weighted sum of Rayleigh distributions to sufficiently model the normalized echo amplitude distribution functions for the fish schools. Additionally, with the exception of the measurements considered by Stanton and Chu (2010), the Foldy (1945) omnidirectional scattering approximations do not hold.

Theoretical approaches have also been attempted to model the distribution of fish schools. In 2002, Moszynski formulated two different simple scenarios (a moving vessel and fish stationary and vice versa) to derive expressions for the probability distribution function of target strength for the school, assuming that the angular positions of the fish are known and the fish are uniformly distributed in the school. These theoretical expressions were compared with acoustic survey results and the findings were consistent. Additionally, Chu and Stanton (2010) derived a general expression of an echo probability distribution function from an aggregation of randomly placed scatterers in a directional beam, assuming direct paths. In doing so, they found that for a

large number of scatterers, the distribution appears more Rayleigh for normalized echo amplitude, compared to a smaller number of scatterers. Formulations were also done taking beam pattern effects into account. Lastly, Abraham et al. (2011) also proposed different models for fitting distributions resulting from clutter. In their paper, they suggested a mixture of Rayleigh or exponential model to fit the in situ measurement distribution. In this thesis, in situ measurements are considered. Unlike Abraham et al. (2011), rather than using a mixture model for the distribution, a weighted continuous sum (integral) of Rayleigh distributions is considered to describe the natural variability of the fish schools.

Simulation studies to understand the echo statistics of fish schools have also been performed, though there have been significantly fewer than acoustic surveys. In 1985, Stanton performed computer simulations using iterative techniques and found that the echo amplitude distribution appeared Rayleigh. *In situ* measurement comparisons were also made. Additionally, Jones et al. (1994) also considered statistical analysis via simulation using an ocean waveguide, though neglecting higher orders of multiple scattering. They also observed that the distribution of the normalized echo amplitude is Rayleigh, but often appears non-Rayleigh depending on the conditions. This was also seen by Lee and Stanton (2014). In Chapter 6, using the Foldy (1945) equations, it is shown that the distribution of the normalized echo amplitude is Rayleigh, regardless of aggregation size, spacing and strength of the individual omnidirectional point scatterers as long as these parameters are unchanged over the realizations. Since in acoustic survey measurements, the geometry of the school and spacing between the fish, is constantly changing, this has not been previously observed or reported.

In particular, in Chapter 6, the statistics of the backscattered returns is evaluated and the probability distribution function is obtained. In the first half of Chapter 6, probability distribution

functions for the backscattered returns of an aggregation of scatterers via the Foldy (1945) equations is obtained for different kinds of aggregation properties. As in the aforementioned studies, the distribution when considering backscattered normalized echo amplitude ($\psi = |p|/\langle|p|^2\rangle^{1/2}$) is found to be Rayleigh. Additionally, when considering a decibel normalization ($\Psi = 10\log_{10}(|p|^2/\langle|p|^2\rangle)$) for the backscattered returns, the distribution is a product of exponentials (extreme value distributed). As in Huang and Clay (1980), since this decibel normalization is algebraically related to the backscattered normalized echo amplitude ($\Psi = 10\log_{10}(\psi^2)$), the probability distribution of the normalized echo amplitude, PDF(ψ) to the probability distribution function of the decibel normalization, PDF(Ψ) can easily be obtained (Billingsley, 1995). Here, all orders of multiple scattering are considered, though an ocean waveguide is not included in the simulation, unlike in Jones et al. (1994). The expected standard deviation is used to determine how few samples are needed to classify an aggregation of scatterers with 95% confidence. The second half of Chapter 6 focuses on analyzing the backscatter statistics from *in situ* measurement from various schools of fish in the ocean and a special probability distribution function is obtained to model the distribution of the normalized echo amplitude from fish schools.

1.7: Thesis Goals and Organization

The goal of this research is to determine if acoustic backscattering characteristics can be used to remotely classify schools of fish from other objects which might primarily be of interest to the U.S. Navy. Knowledge of the acoustic scattering behavior of aggregations of marine life is valuable for Navy sonar applications (Myrberg 1990, Simmonds and Lopez-Jurado, 1991). Additionally, knowledge of the backscattering signature from schools of fish could also help in gaining more insight into the marine ecosystem and determining the location and distribution of the population of fish in the ocean's water column (Makris et al., 2010, Benoit-Bird and Lawson,

2016). The same simulations can also be utilized for bubble clouds (Hwang and Teague, 2000, Hahn, 2007) In this thesis, two techniques are considered to aid in solving the classification problem: (1) the coherent backscatter enhancement, which previously has been primarily used for optics and acoustic ultrasound or seismological purposes, and (2) through analysis of the probability distribution functions for normalized echo (or backscattered pressure) amplitude, $|p|/\langle|p|^2\rangle^{1/2}$, and $10\log_{10}(|p|^2/\langle|p|^2\rangle)$, standard deviation and uncertainty analysis. In the current literature, the coherent backscatter enhancement has mainly been used in optics, electromagnetics, ultrasound and seismological contexts. The work in this thesis explores the possibility of exploiting the coherent backscatter enhancement for schools of fish for the purpose of remote sensing and fisheries acoustics. Additionally, while the current studies thus far have utilized the probability distribution function to analyze the statistics of the backscatter returns from a school of fish, this is the first to determine the distribution function for an aggregation of omnidirectional point scatterers simulated via the Foldy (1945) equations. Lastly, it also gives a weighted probability distribution function to model the returns from an actual school of fish which has not been previously considered in the echo statistics literature.

In this thesis, the following assumptions are made: (*i*) The simulation input parameters have been selected such that the $N \times N$ matrix is invertible. In particular, the dimensionless scattering strength of each scatterer, $k\sigma_s^{1/2}$, is less than $2\pi^{1/2}$ and the scatterers are randomly placed with a minimum exclusion distance apart. (*ii*) Since the speed a fish travels is much less than the speed of sound, Doppler effects or effects of fish motion are not considered in these simulations. (*iii*) Based on Reeder et al. (2004), it was found that much of the scattering from a fish comes from the fish's swimbladder. Consequently, here, each fish is approximated by an omnidirectional point scatterer with properties of a fish's swimbladder. (*iv*) In order to

effectively make comparisons between the spherical aggregations of scatterers with the backscatter equivalent spheres via van Bladel (1968), it is assumed that the sphere is an ideal soft (pressure release boundary conditions) or hard sphere. Thus, fluid-structure interactions are not considered in this dissertation.

This document is organized into six additional chapters. The next chapter describes the mathematical foundations of multiple scattering and scattering from isolated spheres, along with the postprocessing techniques considered. Particularly, it begins by showing the Foldy (1945) multiple scattering equations and how the omnidirectional point scatterers can be modeled as individual fish via the Love (1978) model. It, then, proceeds to present the formulae for a single isolated sphere based on the expressions derived in Morse and Ingard (1968). For this single isolated sphere, boundary conditions such as the pressure gradient set to zero at the surface of the sphere (hard) and pressure release at the surface of the sphere (soft) are applied to yield the van Bladel (1968) equations. Additionally, an impedance boundary condition is also applied where the medium within the sphere has an wave number of k_e, which is the effective wave number obtained from Foldy (1945)'s effective medium theory. This formulation is discussed thoroughly in Hahn (2007). In addition to the scattering formulae, postprocessing techniques upon acquiring the pressure field, such as plane wave beamforming, Fourier transform definitions based on the conventions defined in Foldy (1945) and van Bladel (1968), and the formula for converting between one probability distribution function to another when the random variables are algebraically related are discussed. Lastly, the chapter concludes by describing the mathematical derivations involved in the coherent backscatter enhancement, which is also explained in Sabra (2010).

The study in the third chapter discusses the verification and validation techniques used to determine whether the Foldy (1945) equations can be used to simulate an aggregation of scatterers and acquire the information on the backscatter statistics. CBE simulations are considered, but in the near field. Verification techniques include comparisons by evaluating the Bragg scattering formula for different spacings with the results obtained via simulating a linear arrangement of scatterers using the Foldy (1945) equations and comparison of the results from simulating the exact multiple scattering equations for an aggregation of scatterers with Foldy (1945)'s effective medium theory. These two comparisons are considered verification techniques, because the simulation results can be readily checked with formulae available in the literature or through simple derivations. Validation techniques involve checking that energy is indeed conserved for an aggregation of scatterers (Foldy has already shown that energy is conserved for a single scatterer interacting with an incident wave) via numerical integration and a visual representation of the interaction between an aggregation of scatterers with an incident wave, and replicating existing optics (Wolf et al. 1988) and acoustics (Bayer and Niederdränk, 1993) experiments via simulation. These checks are considered validation techniques since it ensures that the Foldy (1945) equations can be used to simulate the coherent backscatter enhancement and bring to light the limitations in the selections of the input parameters when simulating. Additionally, a near field parametric scaling is proposed which is a function of the strength of the scatterer and the average spacing between scatterers for a three dimensional rectangular aggregation when the receiving array is a wave number scaled distance $kR = 18.2$ away.

The work in Chapter 4 considers single-frequency simulations in the far field and compares the coherent backscatter enhancement simulation results with returns obtained from an

idealized comparable single scatterer in order to aid in the classification problem. This single scatterer is spherical in geometry and the formulae to model the scattering from the object is from Morse and Ingard (1968), van Bladel (1968) and Hahn (2007). Comparisons are done by matching backscattered mean square pressure, $<|p(0)|^2>$, from an aggregation of scatterers with the pressure magnitude squared, $|p(0)|^2$, for the hard and soft van Bladel (1968) spheres. Interestingly, in performing this comparison, for strong multiple scattering effects, there are instances where the corresponding hard and soft van Bladel (1968) spheres exceed that of the aggregation size. From this finding, the parametric scaling in Chapter 3 is improved upon to consider the effective aggregation radius. An additional comparison is also done by matching aggregation sizes, spacings and dimensionless scattering strengths for an idealized sphere with an effective wave number, k_e, and density ρ_e, which is assumed to be the same as the surrounding medium. The comparison is done by considering the ratio of the backscattered magnitude average pressure from an aggregation of scatterers, $|<p_s(0)>|$, to the backscattered magnitude pressure from this idealized sphere, $|p_s(0)|$.

The fifth chapter builds on the results from Chapter 4 to consider broadband pulses (frequency sweep) as the incident signal instead of a harmonic illumination signal. Aggregations of ideal scatterers, along with scatterers with the size of swimbladders and fish flesh viscosity from herring at varying depths, are considered. Comparisons are made between the original illuminating signal with the backscattered signal from the aggregation of scatterers, along with the returns from the van Bladel (1968) sphere with the backscattered signal from the aggregation of scatterers. Due to the complexity of the simulations, these comparisons are done by matching aggregation radii (radius of the aggregation geometry and the radius of the van Bladel (1968) spheres are the same).

Chapter 6 considers the backscatter statistics and uses it to show that the probability distribution function of the backscattered returns can be used in classifying schools of fish from other objects and is a more robust statistical method compared to the use of the coherent backscatter enhancement. Simulation results are extended to *in situ* measurements with the natural variability of actual fish schools in the ocean's water column. Lastly, the final chapter summarizes the findings and discusses the overall conclusions and potential directions for future work.

CHAPTER 2

Mathematical Formulation and Foundations

This chapter provides the mathematical foundations for this investigation into the acoustic coherent backscatter enhancement from aggregations of scatterers when multiple scattering is prevalent. It provides the formulations of the Foldy (1945) equations, the limitations in using the Foldy (1945) equations and the Love (1978) model, and the equations used to model idealized spheres (Morse and Ingard, 1968, van Bladel, 1968, Hahn, 2007). It also presents some definitions (Fourier transforms, statistical quantities), and describes techniques used for post processing the simulation results, such as plane wave beamforming.

2.1: Foldy (1945) Equations

The Foldy (1945) multiple scattering equations for omnidirectional point scatterers are a direct solution to the Helmholtz equation (shown in Appendix A) and are a self consistent formulation for the acoustic interactions of the discrete scatterers with an incident field and with the scattered field from each other. In the formulation considered here, the scatterers are all the same and thus have the same scattering coefficient, g_1. Additionally, each j^{th} scatterer is located at a position $\vec{r}_j$ and $G(\vec{r},\vec{r}_j,\omega)$ is the free space Green's function for acoustic propagation from $\vec{r}$ to $\vec{r}_j$. The two field simulation equations on which this research is based on are:

$$P(\vec{r},\omega) = P_o(\vec{r},\omega) + \sum_j g_1 P_j(\vec{r}_j,\omega) G(\vec{r},\vec{r}_j,\omega), \text{ and} \tag{2-1}$$

$$P_j(\vec{r}_j,\omega) = P_o(\vec{r}_j,\omega) + \sum_{j'\neq j} g_1 P_{j'}(\vec{r}_{j'},\omega) G(\vec{r}_j,\vec{r}_{j'},\omega). \tag{2-2}$$

While both (2-1) is similar to (2-2), there are distinct differences. Whereas (2-1) is the field at the receiving location, (2-2) models the scattered field from a scatterer by all other scatterers at the position of the j^{th} scatterer. Thus, $j \neq j'$ in (2-2). The field scattered from the j^{th} scatterer is assumed to be proportional to the field that would exist at the location of the j^{th} scatterer if that scatterer were absent. The equation for the multiple scattered field at the receiver (2-1) is a superposition of the incident field, $P_o(\vec{r},\omega)$, and the scattered field from each scatterer, which is the sum involving the $G(\vec{r},\vec{r}_j,\omega)$. These equations are suitable for any scalar wave, not just acoustic waves, provided that $P_o(\vec{r},\omega)$ and the summation involving $G(\vec{r},\vec{r}_j,\omega)$ solve the Helmholtz equation and the scatterers are small compared to a wavelength = $2\pi/k$. This formulation is akin to the direct boundary-integral formulation in computational acoustics with one computation element assigned to each scatterer (Kirkup, 2007).

The free space Green's function for a point scatterer is obtained by solving the equation (2-3), where $k = \omega/c$ is the wave number and c is the speed of sound:

$$\nabla^2 G + k^2 G = -4\pi\delta(\vec{r} - \vec{r}_j). \tag{2-3}$$

Using a time dependence of $e^{i\omega t}$ and the Sommerfeld radiation condition, the solution to this equation is the free space Green's function in three dimensions, where $i = \sqrt{-1}$:

$$G(\vec{r},\vec{r}_j,\omega)=\frac{\exp\left(-ik\left|\vec{r}-\vec{r}_j\right|\right)}{\left|\vec{r}-\vec{r}_j\right|} \tag{2-4}$$

The scattering coefficient g_1 was obtained by Foldy (1945) by considering the interaction of an incident plane wave and single scatterer using the radial intensity. Since the power is related to the intensity as an integral over the surface area of the enclosing surface, the power for the scatterer can be obtained. When the acoustic energy is conserved, the net power Π from the scatterer is 0. Using this requirement for acoustic energy conservation, the scattering coefficient for a single omni-directional scatterer is (2-5). The derivation of g_1 is discussed in Appendix B.

$$g_1=\sqrt{\frac{\sigma_s}{4\pi}-\frac{k^2\sigma_e^2}{16\pi^2}}-i\frac{k\sigma_e}{4\pi} \tag{2-5}$$

For ideal scatterers, the scattering, σ_s, and the extinction, σ_e, cross sections are assumed to be equal. Values for k and the scattering and extinction cross sections can be any value, as long as the real and imaginary parts of g_1 exist.

In order to generalize the results, in this dissertation, all formulae have been rendered dimensionless and normalized. Length scales are rendered dimensionless using the incident wave number, k, and pressures by division with the incident pressure amplitude, A ($p = P/A$). The dimensionless form of the Foldy (1945) equations (2-6) and (2-7) and scattering coefficient (2-8) are:

$$p(k\vec{r})=p_o(k\vec{r})+\sum_j kg_1p_j(k\vec{r}_j)\frac{G(k\vec{r},k\vec{r}_j)}{k} \tag{2-6}$$

$$p_j(k\vec{r}_j)=p_o(k\vec{r}_j)+\sum_{j'\neq j} kg_1p_{j'}(k\vec{r}_{j'})\frac{G(k\vec{r}_j,k\vec{r}_{j'})}{k} \tag{2-7}$$

$$kg_1 = k\sqrt{\sigma_s}\left[\sqrt{\frac{1}{4\pi} - \frac{\left(k\sqrt{\sigma_s}\right)^2}{16\pi^2}} - i\frac{k\sqrt{\sigma_s}}{4\pi}\right] \tag{2-8}$$

These equations are implemented in the simulations, where the input parameters are the wave number scaled positions of the scatterers $k\vec{r}_j$ are randomly generated from a seed value corresponding to the realization and $k\sqrt{\sigma_s}$, which is the dimensionless scattering strength of an individual scatterer. Using the value for the dimensionless scattering strength, the dimensionless scattering coefficient (2-8) can be determined. A constraint on (2-8) is that both real and imaginary parts are required (see Appendix B). Thus, $k\sqrt{\sigma_s}$ has an upper bound of $[4\pi]^{1/2} \approx$ 3.5449. The solution to (2-8) is utilized in (2-7), to yield the normalized pressure for the scatterer-scatterer interactions. Together with (2-8), (2-7) is inputted in (2-6) to yield the normalized pressure at a particular receiving location of interest. Modifications to these equations to include fish properties are discussed in the next section.

In order to simplify the exact formulation, Foldy (1945) computed a configurational average (or ensemble average) of the multiple scattering equations over all possible random placements of the scatterers. This configurational average leads to a formula for the average field <*p*>, and to Foldy's equation for the effective medium properties, shown in normalized form as (2-8).

$$\left(\frac{k_e}{k}\right)^2 = 1 + \frac{4\pi k|g_1|}{(ks)^3} \tag{2-9}$$

Here, k_e is the effective wave number inside the aggregation of scatterers, ks is the average wave number scaled spacing between the scatterers and $k|g_1|$ is the result given by (2-7). Frisch (1968) finds that this relationship provides a valid description of <p> when

$$\left|\frac{4\pi(kg_1)^2}{(ks)^3}\right| << 1. \tag{2-10}$$

1. Love (1978) fish model

In order to adequately incorporate fish properties into the simulation, the Love (1978) model needs to be considered. The form of the fish model equations considered here are similar to that of Raveau and Feuillade (2015). Parameters specific to the fish needed in the Love (1978) model are the viscosity of the fish flesh, ξ, and the swim bladder radius, ka_s. The model is applicable at low frequencies and assumes a spherical swim bladder with the gas inside of it to have the same properties of air. It consists of a shell surrounding the spherical swim bladder that is composed of a viscous Newtonian fluid with fish flesh properties. When testing this model with different swimbladder bearing fish, Love (1978) noted that the damping due to thermal effects is negligible (Love 1978, Raveau and Feuillade 2015). Thus, this parameter is neglected.

While most of the aforementioned Foldy (1945) equations are the same, the main change to the aforementioned formulae is with equation (2-8). The scattering coefficient equation, taking into account the Love (1978) model, is:

$$kg_1 = \frac{ka_s}{\left(\omega_o^2/\omega^2\right) - 1 + i\delta}. \tag{2-11}$$

Here, ω_o is the resonant frequency of the swimbladder, ω is the frequency of the incident wave, and δ is the damping constant which consists of the radiation and viscous terms. The damping term can be expressed as (2-12), with H_r and H_v defined by (2-13) and (2-14), respectively with ρ = water density (1000kg/m^3) and c = nominal speed of sound in water (1500m/s):

$$\delta = \frac{1}{H_r} + \frac{1}{H_v} \tag{2-12}$$

$$H_r = \frac{1}{ka_s} \tag{2-13}$$

$$H_v = \frac{\rho c (ka_s)^2}{2k\xi} \tag{2-14}$$

The resonance frequency of the swim bladder is a function of the ambient pressure, P_A, along with the swimbladder radius, ratio of the specific heats, γ, and density of water (Minnaert 1933):

$$\frac{\omega_o}{k} = \frac{1}{ka_s}\sqrt{\frac{3\gamma P_A}{\rho}} \tag{2-15}$$

These equations are a simple modification to (2-6) to approximately incorporate fish-flesh properties into the simulations. The other Foldy (1945) equations and definitions are the same.

2-2: Single Spherical Scatterer Equation – van Bladel (1968), Morse and Ingard (1968) and Hahn (2007)

In order to compare the returns from a spherical geometry school of fish from a large bubble or a manmade object, a single idealized spherical scatterer is used as the model. For the work in this thesis, three different scenarios are considered for predicting the backscattering from ideal spheres: (1) hard surface boundary condition, (2) pressure release boundary condition, and

(3) fluid-filled sphere with properties that match the effective density and sound speed predicted from Foldy's effective medium theory for the corresponding aggregation of point scatterers. The spheres considered here are called ideal because they do not move (no fluid-structure interaction) and do not have any internal structure. The scattered sound field p_s from such spheres can be predicted from the formulae in van Bladel (1968), Morse and Ingard (1968), or Hahn (2007):

$$p_s(k\vec{r}) = \sum_{m=0}^{\infty} -i^m (2m+1) P_m(-\cos(\varphi)) h_m^{(1)}(k\vec{r}) \left[\frac{j_m'(ka) + i\beta_m j_m(ka)}{[h_m^{(1)}(ka)]' + i\beta_m h_m^{(1)}(ka)} \right]. \tag{2-16}$$

Here, φ is the angle measured with respect to the incident wave direction, ka is the wave number scaled radius of the sphere, kR is the wave number scaled receiving range (shown in Fig. 2-1), m is the summing index, $h_m^{(1)}$ is the m^{th} spherical Hankel function of the first kind, j_m is the m^{th} spherical Bessel function, P_m is the m^{th} Legendre polynomial, and the prime denotes differentiation of a function with respect to its argument.

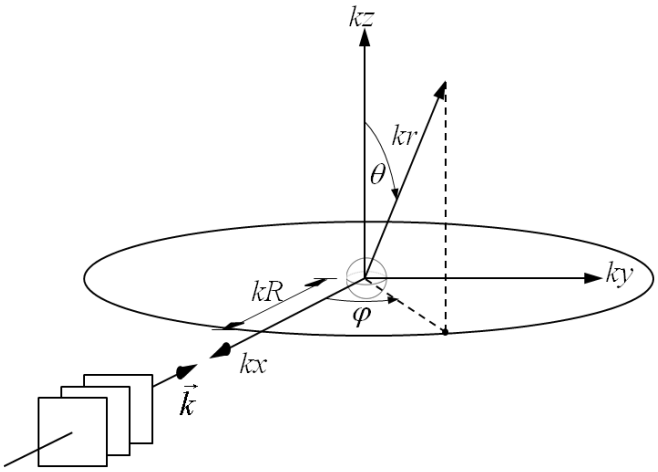

Figure 2-1: Geometry used to model the scattering from the sphere considered in Morse and Ingard (1968)

The term β_m is the impedance contrast of the spherical scatterer from the surrounding medium and is defined in (2-17), where ρ, c, k are the density, speed of sound and wave number,

respectively, of the medium surrounding the sphere and ρ_e, c_e, k_e are the density, speed of sound and the wave number of the medium, respectively, within the sphere:

$$\beta_m = i\frac{\rho c j_m'(k_e a)}{\rho_e c_e j_m(k_e a)}. \tag{2-17}$$

For the spherical Bessel and Hankel function derivatives, the following identities were used:

$$j_m'(x) = \frac{m}{x} j_m(x) - j_{m+1}(x) \tag{2-18}$$

$$[h_m^{(1)}(x)]' = \left[\frac{m}{x} h_m(x) - h_{m+1}(x)\right] \tag{2-19}$$

In order to predict scattering from the sphere considered in Hahn (2007), c_e and k_e are values obtained via the Foldy effective medium theory (2-9). For the concentration of the scatterers considered, the effective density, ρ_e, was nearly the same as ρ so for the calculations completed for this thesis, $\rho_e = \rho$. The van Bladel (1968) hard sphere formula results when β_m tends to 0 and the van Bladel (1968) soft sphere expression occurs when β_m is very large and tends to infinity.

Since the summation of the terms in (2-16) are from $m = 0$ to $m \to \infty$, evaluating these expressions is computationally infeasible. As a result, a convergence study has been done to determine how many terms are needed for the sum to level off. At $ka = 32$, the magnitude of the summand term for $m = 38$ was 1% of the total, so, to ensure convergence when evaluating (2-16), the upper limit of the sums was set to 100.

In order to verify that these equations have been implemented correctly into the codes, two replication tests were completed by (1) comparing approximate results from Pierce (2000)

for small *ka* and a rigid sphere and (2) comparing results from already available codes online. In Pierce (2000), the approximation for the scattered pressure for a small (*ka* << 1) hard sphere is:

$$\left[p(k\vec{r})\right] \approx \frac{-(ka)^3 \exp(-ik\vec{r})}{3k\vec{r}} - \frac{1}{2}\frac{(ka)^3 \cos(\varphi)\exp(-ik\vec{r})}{k\vec{r}} \tag{2-20}$$

Comparing expression (2-20) with (2-15) for a sphere with radius $ka = 1\times10^{-2}$ in the far field with the same receiving range *kR*, yields the Figure 2-2. Here, a relative error is calculated, defined as the difference in the pressure magnitude squared for the result obtained by (2-16), denoted as $|p_{vb}|^2$, between the pressure magnitude squared for the result obtained via (2-19), denoted as $|p_P|^2$ divided by $|p_P|^2$. Here, the relative error is of order 10^{-5}, likely due to the numerical errors in obtaining this approximation.

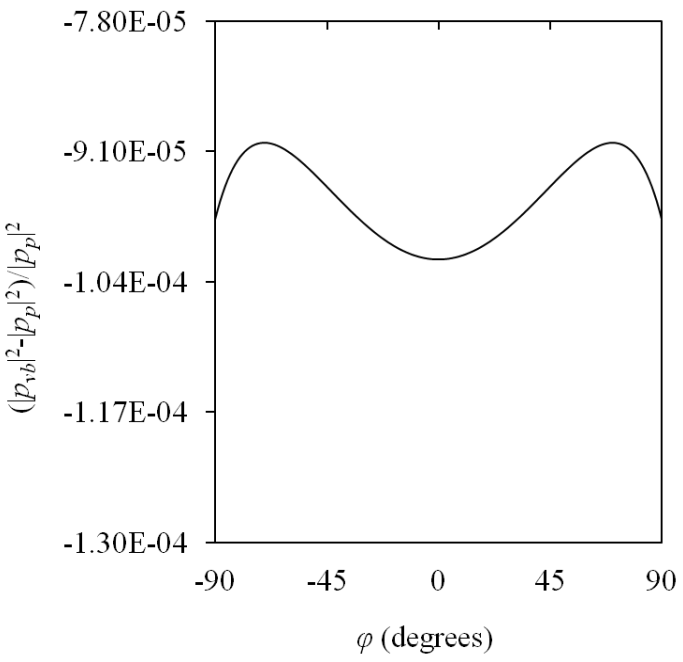

Figure 2-2: Relative error in pressure magnitude square between Pierce (2000) and van Bladel (1968) for $ka = 1\times10^{-2}$

While this comparison does show that the expression is correct for the hard sphere, (2-15) still needs to be verified for the soft sphere. In order to do this, existing imaging results of the intensity available from (Turley, 2006) were replicated for a soft sphere with ka = 15.7. Results obtained from the calculation were comparable and the error for the formula of the soft sphere and the imaging results obtained online (Turley, 2006) gave zero. Thus, the van Bladel (1968) equations can be used to model both a soft and hard sphere and have been successfully implemented to draw comparisons between the returns from an aggregation of scatterers and a single ideal scatterer.

To verify that the Hahn (2007) sphere formulae have been implemented correctly, results from (2-15) were compared with the result obtained using the Foldy (1945) equation for an aggregation of weak scatterers, $k\sigma_s^{1/2}$ = 0.01. This value was selected due to Frisch (1968)'s

requirement for the effective medium approximation, shown in (2-10). For $k\sigma_s^{1/2} = 0.01$ and a spacing $ks = 3.2$, $|4\pi(kg_1)^2/(ks)^3|$ is 3.1×10^{-6}. Figure 2-3 shows the results from comparing an aggregation of scatterers with dimensionless scattering strength $k\sigma_s^{1/2} = 0.01$ for a spherical aggregation with radius $ka = 16$ and $ks = 3.2$ with the Hahn (2007) implementation of (2-16). For an aggregation of weak scatterers, the magnitude of the average pressure over the realizations $|\langle p_s(\varphi)\rangle|$ should be nearly the same as $|p_s(\varphi)|$ from the Hahn (2007). While there are deviations of the simulations from the Hahn (2007) sphere, it would likely resolve with more realizations.

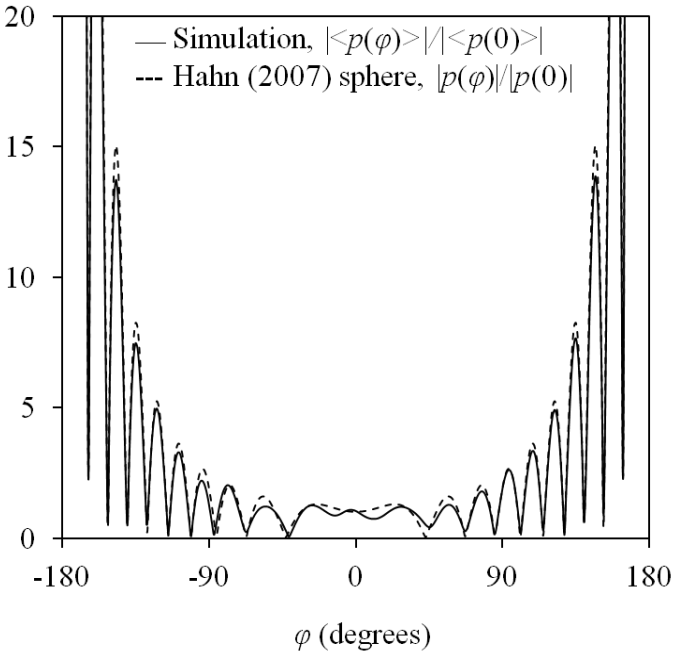

Figure 2-3: Comparison of the normalized average scattered field amplitude $|\langle p(\varphi)\rangle|/|\langle p(0)\rangle|$ from many realizations of a random aggregation of weak scatterers (solid line) with the normalized scattered field amplitude from the Hahn (2007) sphere $|p(\varphi)|/|p(0)|$ (dashed line) for $k\sigma_s^{1/2} = 0.01$, $ks = 3.2$ and $ka = 16$

2-3: Postprocessing Techniques

After the Foldy (1945) or the van Bladel (1968) equations have been evaluated for the simulation of interest, different techniques discussed in this thesis were implemented to analyze the results. In the latter part of Chapter 3, plane wave beamforming is used to obtain intensity and draw comparisons between near field acoustics simulations with near field optics and acoustics experiments. When considering broadband pulses in Chapter 5, the Fourier transform is needed to obtain time domain pressure results for pulses. Lastly, in Chapter 6, in order to perform the statistical analysis for comparisons with ocean experiments, a probability density function is needed and required to convert between different random variables. This section will discuss some of the formulae in order to perform these postprocessing calculations.

1. Plane wave beamforming and the coherence function

To obtain the angular dependence of intensity, plane wave beamforming can be utilized. Plane wave beamforming is an array signal processing technique which involves a signal arriving at a steering angle with respect to the center of the array (Jensen et al., 2011). Delays are applied for each receiving element and then summed to yield a beam pattern. When the magnitude of the beam pattern is squared, the beamformed intensity is obtained. This technique is first employed for CBE purposes by Aubry et al. (2007) in their experiment. This section discusses plane wave beamforming and how, through algebraic manipulation, a spatial coherence function can be defined which will be used to connect results between different receiving resolutions in Chapter 3.

Consider a linear array of N_r receiver elements with length kL spaced $k\Delta y$ apart shown in Figure 2-4.

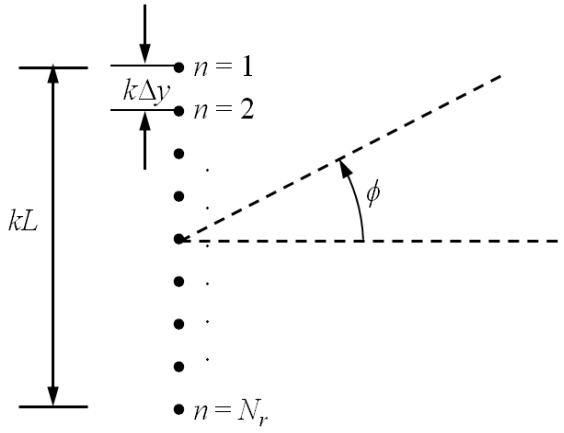

Figure 2-4: A linear receiving array of length kL consists of N_r receiving elements which are spaced $k\Delta y$ apart. The steering angle, ϕ, is measured with respect to the center of the receiving array and the beamformed intensity, $B(\phi)$, is evaluated at each steering angle.

With respect to the first receiver element in the receiving array, the time delay, τ, can be defined as follows:

$$\tau = (n-1)k\Delta y \sin(\phi) \tag{2-20}$$

Here, n denotes the n^{th} receiver element in the linear receiving array and ϕ is the steering angle. To obtain the beamformed intensity, $B(\phi)$, the following formula is used:

$$B(\phi) = \left| \sum_{n=1}^{N_r} p(k\vec{r}_n) \exp(i\tau) \right|^2 \tag{2-21}$$

Here, $p(k\vec{r}_n)$ is the scattered pressure field obtained from evaluating (2-6) at the n^{th} receiving element. Through algebraic manipulation, (2-21) can be expressed as (2-22) when the receiving array is parallel to y-axis:

$$B(\phi) = \sum_{l=1}^{N_r} \sum_{m=1}^{N_r} p^*(ky_l)\, p(ky_m) \exp(ik(y_l - y_m)\sin(\phi)) \tag{2-22}$$

When the receiving array is a continuous line array, the summations can be replaced by integrals. For the simulations, for multiple realizations, (2-22) can be written as follows where < > denote the ensemble average operation:

$$\langle B(\phi) \rangle = \sum_{l=1}^{N_r} \sum_{m=1}^{N_r} \langle p^*(ky_l)\, p(ky_m) \rangle \exp(ik(y_l - y_m)\sin(\phi)) \tag{2-23}$$

The spatial coherence function, $\Gamma(k\Delta y)$, is represented as the normalized pressure terms within the < > in (2-23). In Chapter 3, the coherence function is expressed as the sum of a diffuse field and a backscattered field. The diffuse portion of the coherence function is a sinc function (Walker and Buckingham, 2012, Singer et al., 2005) and the backscattered part of the coherence function represented by $f(k\Delta y)$ for now. The selection of $f(k\Delta y)$ will be discussed in greater detail in Chapter 3. Thus, $\Gamma(k\Delta y)$ is hypothesized to have the following form:

$$\Gamma(k\Delta y) = A_d \frac{\sin(k\Delta y)}{k\Delta y} + A_b f(k\Delta y) \tag{2-24}$$

Here, A_d is the amplitude of the pressure in the diffuse field and A_b is the amplitude of the pressure in the backscattered field. Selection of the values of the coefficients will be discussed in Chapter 3.

2. Fourier Transform

In Chapter 5, broadband chirps in the time domain are considered as the illuminating signal, $s(t)$ with Fourier transform $S(\omega)$. In this thesis, the Fourier transform definition considered for the Foldy (1945) equations is:

$$S(\omega) = \frac{1}{2\pi} \int_{-\infty}^{\infty} s(t) \exp(i\omega t) dt \tag{2-25}$$

For the convention in van Bladel (1968), the complex conjugate of (2-24) is considered. The Foldy (1945) and van Bladel (1968) equations are evaluated at the frequencies which compose the signal's spectrum and the outcome, $p(\vec{r}, \omega)$, is weighted by the Fourier transform of the pulse, $S(\omega)$, to yield $p_w(\vec{r}, \omega)$:

$$p_w(\vec{r}, \omega) = p(\vec{r}, \omega) S(\omega) \tag{2-26}$$

In order to return back to acoustic pressure in the time domain, the inverse Fourier transform is evaluated. When the Foldy (1945) equations are considered, the inverse Fourier transform definition is (2-27) and for the van Bladel (1968) equations, the complex conjugate of (2-27) is the inverse Fourier transform definition to be used, due to the differences in convention of the incident signals.

$$p(\vec{r}, t) = \int_{-\infty}^{\infty} p_w(\vec{r}, \omega) \exp(-i\omega t) d\omega \tag{2-27}$$

In Chapter 5, comparisons of the returns from a school of fish using the Foldy (1945) equations with a single large ideal scatterer with the scattering modeled via the van Bladel (1968) are performed in the free space by considering time domain signals. Comparisons showing angular and time dependence will be shown.

3. Statistical Analysis

In Chapter 6, a technique involving the backscattered probability distribution function is considered to determine whether a school of fish or an single isolated object is present. This

technique involves considering the statistical realizations of the backscatter direction only and normalizing these results to generate a probability density function. To do this, the Foldy (1945) equations are evaluated using equations (2-5) and (2-6) in just the backscatter direction. Samples of pressure magnitude squared or pressure magnitude, obtained from evaluating the Foldy (1945) equations, are considered and sorted into a histogram.

The backscattered pressure magnitude samples were first normalized by the average backscattered pressure magnitude, $\psi = |p|/\langle|p|^2\rangle^{1/2}$, and then, the histogram is normalized to have unit area to yield a probability density function, $PDF(\psi)$:

$$PDF(\psi) = \frac{H(\psi)}{Area(H(\psi))} \tag{2-28}$$

Here, $H(\psi)$ is the histogram of the normalized backscattered pressure and $Area(H(\psi))$ is the area under the histogram (Smith, 1997).

The probability density function (2-28) can also be converted to a decibel (($\Psi = 10\log_{10}(|p|^2/\langle|p|^2\rangle)$, in dB) independent variable or to other variables s which are a function of the pressure. To convert to a different probability density function, $PDF(\Psi)$, the following formula can be used (2-29) (Billingsley 1995):

$$PDF(\Psi) = PDF(\psi(\Psi))\left|\frac{d\psi}{d\Psi}\right| \tag{2-29}$$

Here, it is assumed that the derivative is defined and that Ψ is defined and single valued. Ultimately, the area under (2-28) is the same as the area of (2-29).

In Chapter 6, the backscattered probability distribution function will be generated for an aggregation of omnidirectional point scatterers simulated using the Foldy (1945) equations. It

will show that the distribution when considering a $\psi = |p|/\langle|p|^2\rangle^{1/2}$ normalization is always Rayleigh distributed and extreme value distributed when considering a $\Psi = 10\log_{10}(|p|^2/\langle|p|^2\rangle)$ normalization, regardless of average aggregation spacing, dimensions and strength of the scatterers making up the aggregation. However, interestingly, when *in situ* measurements are considered, the backscattered probability distribution function is non-Rayleigh and is better described as the sum of the product of a Rayleigh distribution and a weighting function for varying means.

Chapter 3

Verification and Validation

This section describes the verification and validation tests done to ensure that the Foldy (1945) equations have been implemented correctly and that they meet the constraints for simulating far field acoustic coherent backscatter enhancement discussed in Chapters 4 and 5, and for performing the statistical analysis in Chapter 6. Here, verification is defined as ensuring that the computational implementation is done correctly and validation is defined as the determination that the model has a range of accuracy for the intended application (Sargent 2003, Schlesinger et al. 1979). It is expected that the Foldy (1945) equations are: energy conserving for an aggregation of scatterers with minimal error, can properly model the physics of the waves, and are an exact solution to the Helmholtz equation without neglecting higher order terms so that the coherent backscatter enhancement can be simulated. In order to ensure that the Foldy (1945) equations do satisfy these constraints, several tests have been done. The verification tests considered here ensure that: the phasing of the scattered waves is correct via Bragg scattering for a linear arrangement of scatterers, and that the Foldy's (1945) effective medium theory formula for an ideal aggregation of scatterers correctly predicts the effective wave number. Validation tests include: (1) ensuring energy is conserved for an aggregation of scatterers for different levels of multiple scattering effects, and (2) replicating two near field experiments (one in optics and one in acoustics). An extension of the near field simulations by considering parametric scaling to

predict peak heights is also considered and discussed. Findings from this chapter appear in Mookerjee and Dowling (2015).

3-1: Verification

The verification simulations performed use Bragg scattering from a structured, linear arrangement of scatterers and also compares results with the effective medium theory that was also proposed in Foldy's (1945) paper. The first half of this section will describe the Bragg scattering simulations and the second half of this section will consider the results obtained from the full form of the Foldy (1945) equations and from the effective medium theory. These simulations are considered verification tests since the results from these simulations can readily be checked with established formulae from physics.

In Bragg scattering, a wave interacts with a structured arrangement of scatterers. The scattered waves from the scatterers can add constructively or destructively, resulting in strong radiation (Bragg peaks) at certain angles. The angles where the peaks occur can be predicted using trigonometric formula and basic geometry. The predicted angles, φ_m, where these peaks are expected is shown by the formula (3-1) where *ks* is the wave number scaled spacing between the scatterers and *m* is any integer such that $0 \le 2\pi m / ks \le 2$ (Bragg 1913):

$$\varphi_m = \cos^{-1}\left(\frac{2\pi m}{ks} - 1\right) \tag{3-1}$$

The location of the Bragg peaks vary depending on the wave number scaled spacing.

The simulation geometry is shown as Figure 3-1. Here, a linear array of scatterers are placed along the –x axis, denoted as dots in the figure, and the incident plane wave with wave

number $\vec{k}$ traveling into the page illuminates these scatterers. A receiving ring in the far field located at $\theta = 90°$ with wave number scaled radius *kR* records the returns in the form of a far field normalized scattered intensity in dB ($10\log_{10}(|p(\varphi)|^2/|p(0)|^2)$). For these simulations, there were 13 scatterers with a dimensionless scattering strength of $k\sqrt{\sigma_s} = 3.5$. In order to check for consistency, two different wave number scaled spacings were considered: *ks* = 3.2 and 8.4.

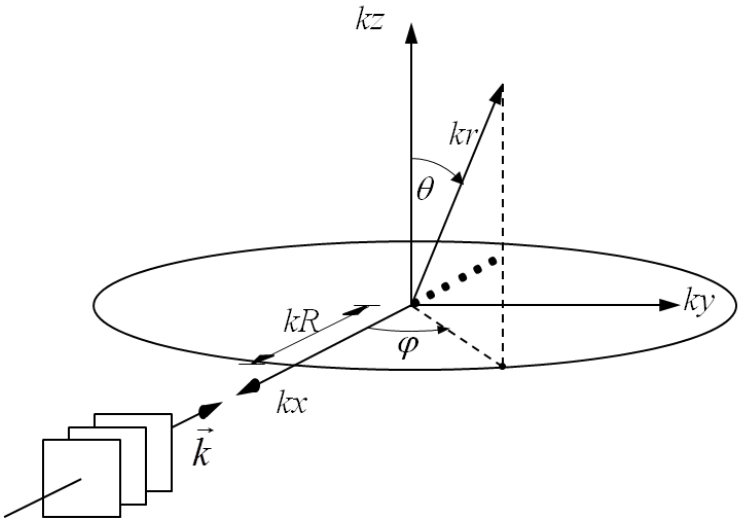

Figure 3-1: Geometry used for the Bragg scattering simulations: Thirteen scatterers (black dots) are placed along the negative x-axis. The scatterers have a scattering strength of $k\sqrt{\sigma_s} = 3.5$ and a spacing of *ks* = 3.2 and 8.4. A plane wave with wave number $\vec{k}$ illuminates the scatterers. The mean square pressure is evaluated on a ring with radius $kR = 8.38\times10^4$ for varying φ and $\theta = \pi/2$. The backscattered direction is $\varphi = 0$ and $\theta = \pi/2$.

Figure 3-2 shows the results of the Bragg scattering angles via simulation and through the use of (3-1) for the two different spacings. Here, a solid black line (—) is the normalized scattered intensity in dB as a function of angle φ obtained via simulation and (----) is the location of the expected Bragg peaks obtained via equation (3-1). For a spacing of *ks* = 3.2 two Bragg peaks result at φ_m = 15.5 and 180 degrees. From evaluating the Foldy (1945) equations, Figure 3-

2(a) show peaks at the same location. Similarly, for a spacing of ks = 8.4, Bragg scattering peaks occur at three different locations: 60, 104.5 and 180 degrees. From simulation, Figure 3-2(b) show peaks at the same location. This agreement suggests that the scattered field obtained from the simulations matches the expected scattering physics since the phasing of the scattered waves is consistent with results expected from theoretical Bragg scattering formulae.

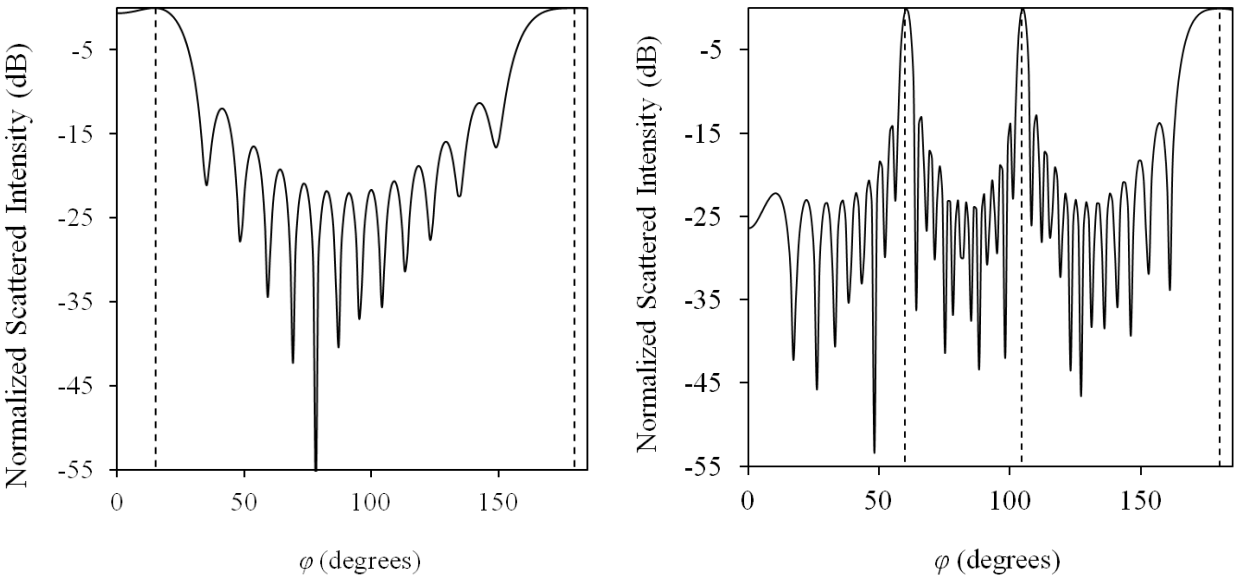

(a) (b)

Figure 3-2: Simulation results for Bragg scattering simulations (—) and expected angles from theory (----) for (a) ks = 3.2 and (b) ks = 8.4. The Bragg peaks at the scattering angles are in agreement.

Since it seems that the Foldy (1945) equations follow Bragg scattering, the simulations are compared with the effective medium theory also discussed in Foldy's (1945) paper. In this paper, Foldy (1945) used the multiple scattering equations discussed in Chapter 2, made a simplifying approximation, and took an ensemble average to obtained a relation between the wave number inside the scattering medium, k_e, and the incident wave number, k, that includes the

average spacing between the scatterers, *ks*, and the dimensionless scattering coefficient $k|g_1|$. This equation is nondimensionalized and provided here as (2-8). In this section, a cube of scatterers is considered and the acoustic field is sampled inside the cube to determine the ratio k_e/k from the simulation and comparing that value with that predicted by (2-8).

The aggregation of interest for this effective medium theory comparison was a cubical aggregation with wave number scaled dimensions $kX = kY = kZ = 43$. The number of scatterers considered was 3900, resulting in an average spacing between scatterers of $ks = 2.7$. The wave number scaled scattering strength of each scatterer was $k\sqrt{\sigma_s} = 0.21$. The acoustic field was sampled inside of a cylinder with diameter $kW = 22$ that passes through the center of the aggregation. The sample points are wave number spaced by $kd = 0.8$ in the *ky* and *kz* directions and $k\delta x = 0.049$ in the *kx* direction. The simulation setup is shown in Figure 3-3.

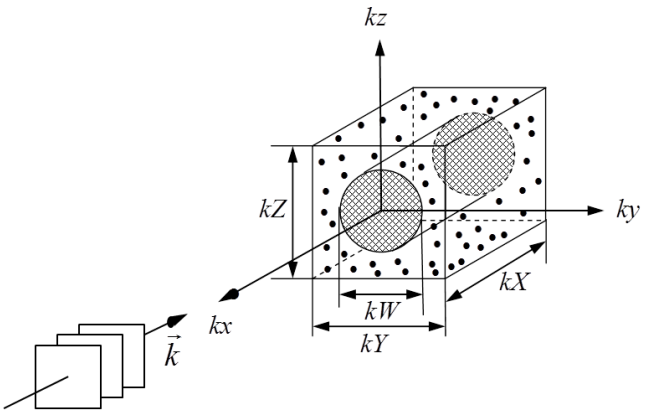

Figure 3-3: Geometry used for simulations of Foldy's effective medium theory. Scatterers (denoted as black dots) are placed in a 3D cubical aggregation. A plane wave with wave number $\vec{k}$ illuminates the scatterers. Receiver elements are in a cylinder with diameter $kW = 22$ and the pressure is evaluated at varying depths into the aggregation. The 3900 scatterers have a scattering strength of $k\sqrt{\sigma_s} = 0.21$. The aggregation dimensions are $kX = kY = kZ = 43$.

In these simulations, the field values obtained from the sample points are averaged in the *ky* and *kz* directions to obtain the coherent field <*p*> as a function of distance *kx* into the aggregation. The resulting plot from this verification test is shown as Figure 3-4 where the real part of <*p*> (solid curve) and the real part of the incident plane wave p_o (dashed curve) are plotted as a function of wave number scaled distance, *kx* < 0, into the aggregation. Here, as expected, the presence of scatterers increases the effective wave number inside of the scattering aggregation. For the conditions of these simulations, the ratio k_e/k from (2-8) is 1.0182 and the value of this ratio determined from the simulations is 1.0183. This is in good agreement and suggests that the Foldy (1945) equations have been implemented correctly for these simulations.

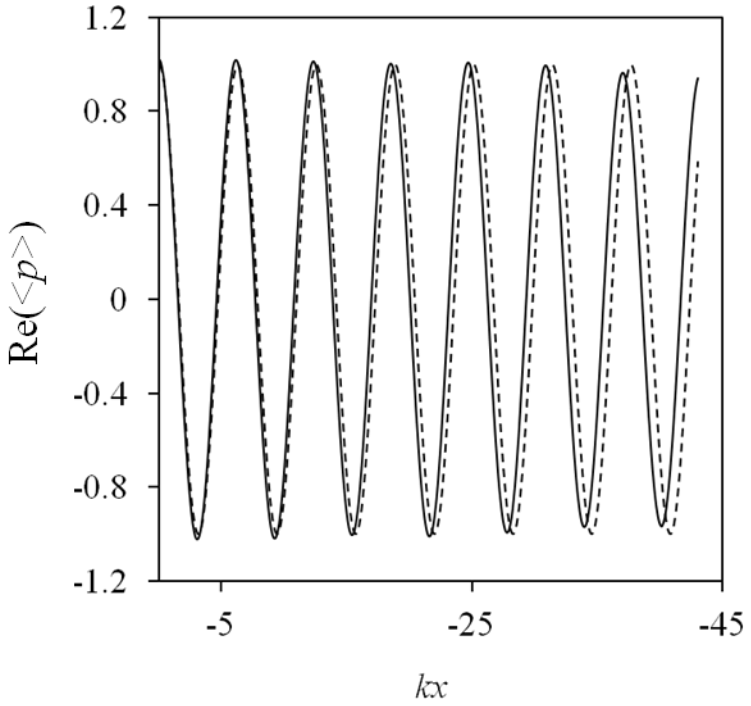

Figure 3-4: Effective medium theory verification test results for a 43 by 43 by 43 cube with Re(<p>) as the solid curve and Re(p_o) as the dashed curve.

Both of the tests discussed successfully verify the simulations. The Bragg scattering simulations show that Bragg peaks occur at angles expected by the Bragg scattering formulae. This suggests that the phasing of the scattered waves appear to be in agreement with expectations from the scattering physics. Additionally, the Foldy effective medium theory also holds and the simulation results are in agreement with the formula proposed by Foldy (1945). As a result, the Foldy (1945) equations have been properly implemented and can be used for further validation testing.

3-2: Validation

Since it seems that the Foldy (1945) equations have been correctly implemented into the codes and passes all verification checks, the simulations are now validated and tested to see if the Foldy (1945) equations are suitable to simulate the coherent backscatter enhancement and perform statistical analysis for sonar and remote sensing applications. The validation tests done involve: considering if the scattering aggregation is energy conserving, and replicating existing experimental results. The first half of this section will discuss conservation of acoustic energy and analyzing intensity maps to visualize the physics of the interactions between an incident wave and an aggregation of scatterers. Here, a preliminary verification test is initially done by considering the interaction of an incident wave with a single scatterer to ensure that it is in agreement with Foldy (1945)'s assumptions in the derivation of g_1 (see Appendix B). The additional energy conservation checks involving varying the parameters to increase the multiple scattering effects are considered validation checks. In this case, variations are made in the number of scatterers (or the average spacing between scatterers), and the strength of each scatterer to determine if energy is still conserved for the aggregation and if the resulting net power is sufficiently negligible to confirm the accurate use of the Foldy (1945) equations for simulating the coherent backscatter enhancement. The second half of this section describes existing near field CBE experiments and the current attempts to replicate these results. Part of the second half of the section considers replicating a near field optics experiment from Wolf et al. (1988) and the remainder will focus on replicating a near field acoustics experiment from Bayer and Niederdränk (1993).

1. Conservation of Energy

The Foldy (1945) equations assume that energy is conserved for a plane wave interacting with a single scatterer. However, it does not require energy to be conserved for an aggregation of scatterers. In order to check this, a preliminary verification test was done for only a plane wave with no scatterers present, and for a single scatterer interacting with an incident plane wave to ensure that the power calculation was done correctly and to determine the extent of numerical error for varying dimensionless scattering strengths. Then, the same calculations were done for 100 and 3900 scatterers for varying dimensionless scattering strengths as a validation effort. In this section, the result from a single realization is considered for each of the calculations. In order to visualize the physics of the wave interacting with the scatterer(s), Mercator projected intensity maps are shown.

The first step in this validation test is to recognize that the Foldy (1945) equations have a limitation imposed on the wave number scaled scattering strength. This is discussed in extensive detail in Appendix B. The wave number scaled scattering strength can be any value such that $0 < k\sqrt{\sigma_s} < 2\sqrt{\pi}$. If the wave number scaled scattering strength is larger than $2\sqrt{p}$, then the scattering cannot be omnidirectional. This region for the wave number scaled scattering strength is defined by acoustic energy conservation for a single scatterer interacting with an incident harmonic plane wave. However, this constraint does not directly require acoustic energy conservation for a large number of interacting point scatterers.

The second step in this validation test is to numerically compute the integral of the radial intensity I_r over a spherical surface that completely encloses the aggregation to determine the net power Π from the aggregation (Figure 3-5):

$$\Pi = \int_{sphere} I_r dA = \int_{sphere} (I_r - I_{r,o}) dA \tag{3-2}$$

Here, $I_{r,o}$ is the radial intensity of the incident plane wave and its contribution to Π is zero. In order to increase the numerical accuracy of the final determination of Π when the scattering was weak and I_r is nearly equal to $I_{r,o}$, $I_{r,o}$ is subtracted from I_r. For this validation effort, (3-2) was computed using two-dimensional Romberg integration.

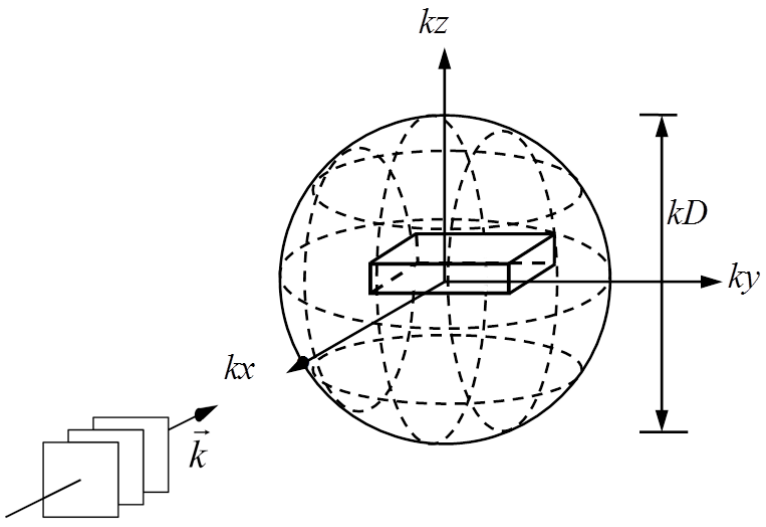

Figure 3-5: Simulation Geometry for the Acoustic Energy Calculation Validation Effort

The aggregation considered is a 3D rectangular geometry with dimensions kX = 64, kY = 100 and kZ = 20. The number of scatterers in the rectangular geometry is increased (ks decreased) from N = 1 to 100 to 3900 scatterers. Additionally, the scatterer's dimensionless

scattering strength is increased from $k\sqrt{\sigma_s} = 0.21$ to 1 to 3.5. All these values for the dimensionless scattering strength are within the regime where energy is conserved for a single scatterer interacting with an incident plane wave so it would be expected that the power for a single scatterer would be zero. However, since the calculation is performed numerically, there may be some numerical error in the power evaluation.

In order to visualize the wave-aggregation interactions, a Mercator projected radial intensity map was generated. As a baseline, Figure 3-6 shows the radial intensity of a plane wave entering and exiting a sphere with kR = 100. Since the radial intensity is normalized by the theoretical intensity of a plane wave, by convention, the wave entering into the sphere is shown in blue as -1 and the wave exiting the sphere is shown in red as +1. This radial intensity map is as expected.

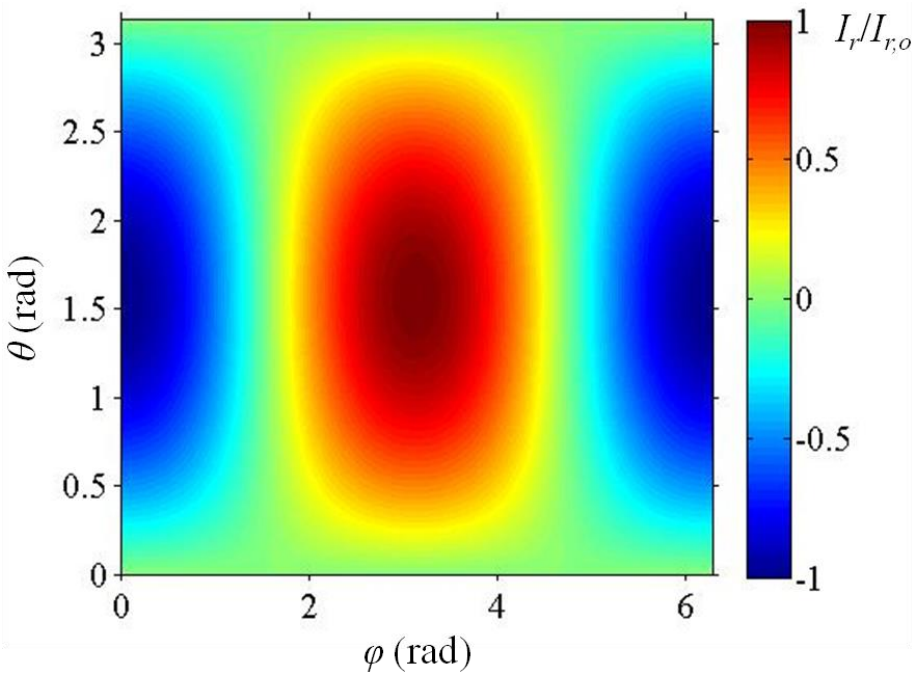

Figure 3-6: Mercator projected radial intensity map for a plane wave entering and exiting a sphere

Since the intensity map for a plane wave is as expected, intensity maps are considered for an increase in the multiple scattering effects. This occurs when $k\sqrt{\sigma_s}$ approaches its upper limit and *ks* decreases. Table 3-1 shows the effect of increasing the multiple scattering effects by increasing the scattering strength (horizontal changes) and also increasing the number of scatterers (vertical changes). The rectangular structure shown at the center of the intensity maps for $k\sqrt{\sigma_s} = 3.5$ and 100 scatterers, and the 3900 scatterer simulations is the acoustic shadow produced by the aggregation. Interestingly, the intensity map for 3900 scatterers and $k\sqrt{\sigma_s}$ = 3.5 shows that the incident wave is unable to penetrate the aggregation very far and much of the wave is deflected by the edges of the aggregation. Thus, while the scattering coefficient constraint given by Foldy (1945) does ensure energy conservation for a single scatterer, there is an upper limit for $k\sqrt{\sigma_s}$ and *N* for the wave to fully enter and exit the aggregation.

For perfect energy conservation Π from (3-2) should be zero so when Π is nonzero, it indicates error within the simulations and/or the evaluation of (3-2). The extent and significance of such errors were assessed through simulations with widely varying *N* and $k\sqrt{\sigma_s}$ via the ratio $\left|\Pi / \Pi_{ref}\right|$ where

$$\Pi_{ref} = N\sigma_s I_{x,o} \tag{3-3}$$

is the total power of the incident plane wave that would be scattered by the aggregation if each scatterer were separately illuminated with the incident plane wave intensity $I_{x,o}$.

Results for the ratio $\left|\Pi / \Pi_{ref}\right|$ are also shown above the intensity maps in Table 3-1 for the situation shown in Figure 3-5 with a fixed wave number scaled aggregation size of *kX* = 64,

kY = 100 and *kZ* = 20 and a fixed enclosing sphere with wave number scaled diameter *kD* = 167.6 when $k\sqrt{\sigma_s}$ = 0.21, 1.0 and 3.5 and *N* = 1, 100 and 3900. Additional energy conservation calculations have also been done and are tabulated in Table 3-1 and in Mookerjee and Dowling (2015), as Table 3-2. For all cases, Π is less than $1/6^{th}$ of the power incident on a single scatterer. Thus, the simulations, while imperfect, do approach the ideal energy conservation condition and this validation test was considered successful.

Table 3- 1: Intensity maps and power calculation results for vary number of scatterers and dimensionless scattering strengths.

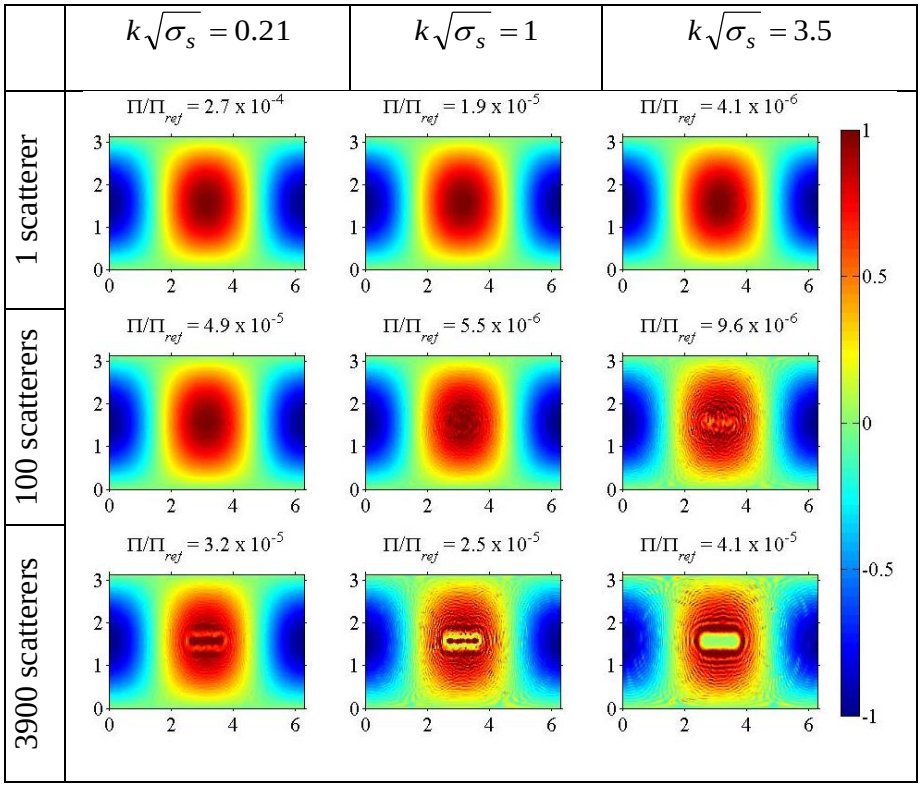

Table 3- 2: Ratio of acoustic powers from (3-2) and (3-3) for different numbers of scatterers and for different scattering cross sections

Condition	1 scatterer	10 scatterers	100 scatterers	1000 scatterers	3900 scatterers
$k\sqrt{\sigma_s} = 0.21$	2.7×10^{-4}	6.3×10^{-4}	4.9×10^{-5}	5.7×10^{-5}	3.2×10^{-5}
$k\sqrt{\sigma_s} = 1$	1.9×10^{-5}	7.6×10^{-6}	5.5×10^{-6}	5.9×10^{-7}	2.5×10^{-5}
$k\sqrt{\sigma_s} = 3.5$	4.1×10^{-6}	1.5×10^{-5}	9.6×10^{-6}	4.5×10^{-5}	4.1×10^{-5}

2. Replication of Near Field Experiments – Optics (Wolf et al., 1988)

As a final validation of the simulations, comparisons between prior experiments were made with the simulations. Given the limitation of the Foldy (1945) equations (scalar waves, point scatterers, omnidirectional scattering) and the experimental history of CBE in optics and acoustics, both optics and acoustics experiments were considered. In both cases, the simulations parameters were matched – to the extent possible – to those of the available experiments. Thus, the optics measurement chosen for comparison was the smallest bead experimental results reported by Wolf and Maret (1985) and Wolf et al. (1988). The most relevant experimental result for this comparison reported in Wolf et al. (1988) is for the smallest optical scatterers, d = 0.109μm diameter polystyrene sphere suspended in water and illuminated with green laser light (λ = 0.5145μm in air) so kd = 1.77. Here, some discrepancy with point scatterer simulations is anticipated since the Foldy (1945) equations assume omnidirectional point scatterers where kd << 1. Additionally, multiple realizations are considered and an ensemble average is taken over the realizations. The volume fraction of the spheres was 10% leading to wave number scaled spacing of ks = 3.1 and a wave number scaled optical mean free path of kl = 925. Given that the scattering and geometrical cross sections of a scatterer may not be equal, a Mie scattering

calculation was performed by Wolf et al. (1988) to determine $k\sqrt{\sigma_s} = 0.23$. The size of the optical scattering aggregation (1mm by 1cm by 1cm) corresponds to wave number scaled dimensions of $kX \approx 16000$ and $kY = kZ \approx 160000$ and the peak to null angular resolution of the goniometer used for directional optical intensity measurements was 0.5 milli-radians.

The simulations were nominally matched to the experiments using a wave number scaled spacing of $ks = 3.2$ and a mean free path of $kl = 926$. The scattering strength was adjusted such that the wave number scaled mean free path and the spacing were near the experimental values, to yield a strength of $k\sqrt{\sigma_s} = 0.21$. The size of the scattering aggregation was significantly smaller than that of the experimental optical aggregation with dimensions initially oversized. A wave number scaled thickness of $kt = 3.2$ was removed from each face of the oversized aggregation, ultimately yielding an aggregation with dimensions, $kX = 64$, $kY = 100$ and $kZ = 20$, to ensure that the aggregation was statistically homogeneous. In order to make the aggregation appear as a semi-infinite medium, a linearly decreasing taper was added to the back of the rectangular aggregation from $-84 \leq kX \leq -64$ to prevent a structured reflection from the back surface of the aggregation. This linear tapering added 350 scatterers to the rear of the rectangular aggregation (not depicted in Figure 3-7). The backscattered sound was sampled at 81 locations placed a distance kR in front of the aggregation and having an overall length of $kL = 64$. The peak-to-first-null angular resolution of this linear receiving array ($2\pi/kL$) was 98 mrd (5.6°).

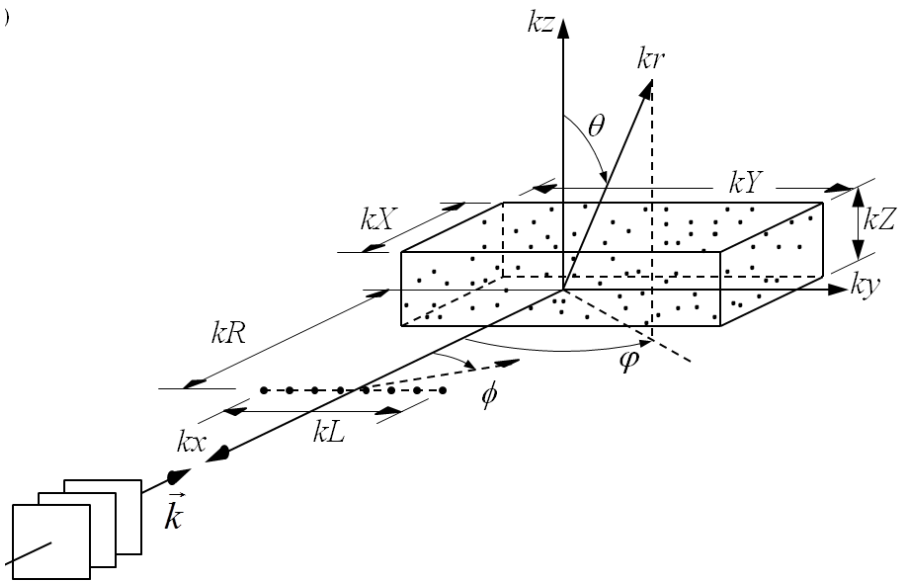

Figure 3-7: Simulation geometry used to replicate the existing experiments

The simulation results were assembled as an ensemble average of realizations of the beamformed scattered intensity $B(\phi)$ normalized by its value $[B(\phi)]_{not\ peak}$, near but not within the CBE peak. In this situation, $B(\phi)$ is related to the scattered field's coherence function $\Gamma(\vec{r}-\vec{r}\,') = \left\langle p_s(\vec{r})\, p_s^{\,*}(\vec{r}\,') \right\rangle$, through a discrete finite-domain double Fourier transform:

$$B(\phi) = \left\langle \left| \sum_{j=1}^{J} \frac{p_s(\vec{r}_j)}{A} \exp\{-iky_j \sin\phi\} \right|^2 \right\rangle = \sum_{j=1}^{J}\sum_{j'=1}^{J} \left\langle p_j\, p_{j'}^{*} \right\rangle \exp\{ik(y_{j'} - y_j)\sin\phi\} \tag{3-4}$$

$$\cong \frac{(J-1)^2}{(kL)^2} \int_{ky'=-kL/2}^{kL/2} \int_{ky=-kL/2}^{kL/2} \Gamma(ky-ky') \exp\{i(ky-ky')\sin\phi\}\, d(ky)\, d(ky'),$$

The angle brackets denote an ensemble average, A is the amplitude of the incident plane wave, J is the number of receivers, and $p_j = P_s(\vec{r}_j)/A$ is the normalized complex pressure at the j^{th} receiving-array element located at (kR, ky_j, 0) using the Cartesian coordinates shown in Fig. 3-8). The approximate equality of (3-4) holds when there are sufficient array elements to mimic a

continuous line receiver. Since the receiving array is parallel to the *ky*-axis, only the *ky*-coordinates of the receiver locations are listed in (3-4).

Simulated CBE results for $B(\phi)/[B(\phi)]_{not\ peak}$ from directly evaluating the first equality of (8) for the geometry shown in Fig. 3-7 are shown in Fig. 3-8, when the linear receiving array is located at wave number scaled distances of kR = 5 (••••••••••), 8.2 (- • - • - • -), 11.2 (– – – –), 13.2 (- - - - -), 15.2 (– • – • –), and 18.2 (- - - - -). Here the angular width of the CBE peaks is set by the resolution of the linear receiving array because the coherence width (or length) of the CBE contribution to Γ is greater than kL. The heights of the simulated CBE peaks shown in Fig. 3-8 decline monotonically with decreasing kR, and this is a geometrical effect of the finite size aggregation used in the simulations. Since the simulated aggregation is smaller than the experimental aggregation, in order for the simulated aggregation to appear infinite when viewed from the receiving array, the receiving array must be brought closer to the *x*-*y* plane, the beam steering angle between the center of the receiving edge of the aggregation is $\phi_{\max}(kR) = \tan^{-1}(kY/2kR)$ (Figure 3-8). When kR decreases for fixed kY and kZ, the angular ranges from which scattered sound can be received by the array increase and this raises the level of $[B(\phi)]_{not\ peak}$. In the combined limits $kZ/kR \to \infty$ and $kY/kR \to \infty$, the second of which implies $\phi_{\max}(kR) \to 90°$, the aggregation appears to be infinite when viewed from the array, and this is the nominal geometric circumstance of the optics experiments. Thus, the limiting form of the simulation output for $kR \to 0$ is needed for comparison with the optical CBE measurement.

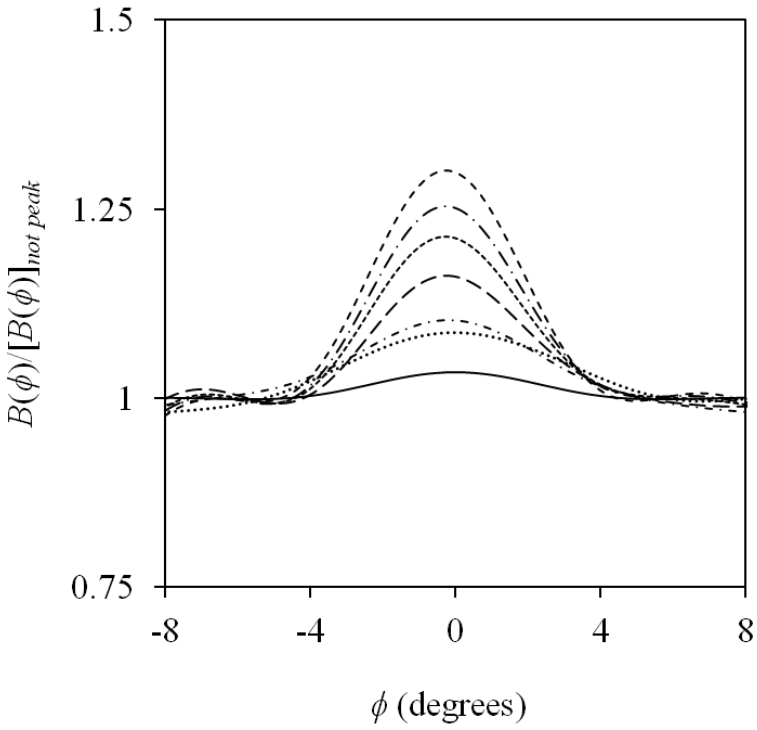

Figure 3-8: Simulation results for replicating the existing optics experiments for varying ranges: kR = 5 (••••••••••), 8.2 (- • - • - • -), 11.2 (– – – –), 13.2 (- - - - -), 15.2 (– • – • –), and 18.2 (- - - -)

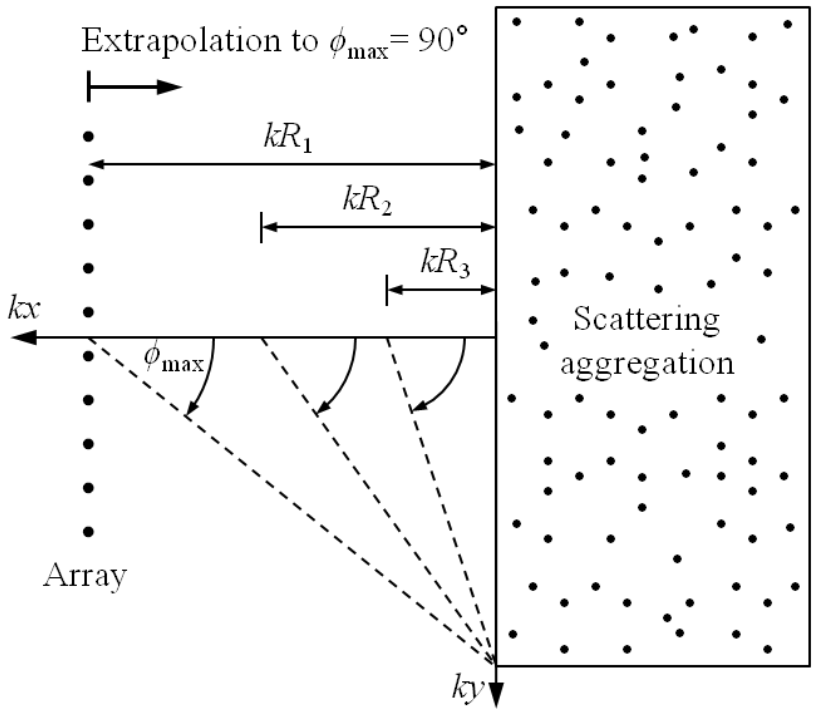

Figure 3-9: Simulation geometry for varying the range from kR_1 to kR_3

This limiting form of the simulation results is shown as the solid curve in Fig. 3-8. The CBE peak height of this extrapolated curve was obtained by the extrapolation shown on Fig. 3-10, where simulated values of $B(0)/[B(\phi)]_{not\ peak}$ (circles) are plotted vs. $\phi_{max}(kR)$. The limit $\phi_{max}(kR) \to 90°$, achieved via $kR \to 0$, is difficult to take in the simulation since the *1/r* singularity near any scatterer causes convergence problems when the receiving array approaches the aggregation too closely. Therefore, quadratic and power law extrapolations to the simulation results are shown as short and long dashed curves. At $\phi_{max}(kR)$ = 90º, these fits yield $B(0)/[B(\phi)]_{not\ peak}$ = 1.04 and 1.02, respectively. The lone triangle data point on Fig. 3-10, $B(0)/[B(\phi)]_{not\ peak}$ = 1.030 ± 0.005 at $\phi_{max}(kR)$ = 90º, is the average of these fitted values and it sets the CBE peak value of the extrapolated curve on Fig. 3-10.

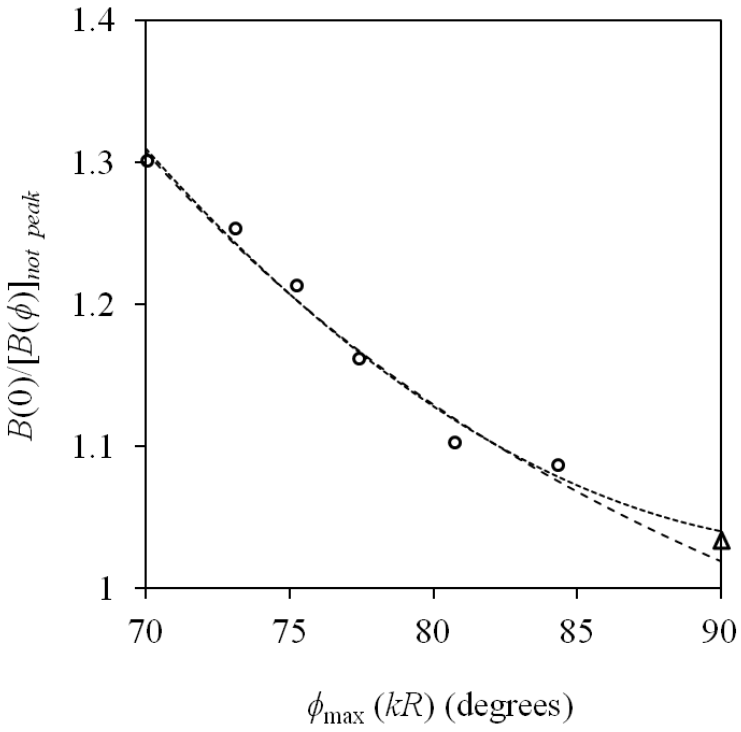

Figure 3-10: Simulated CBE Peak ratios (circles) from Fig. 3-8 vs. $\phi_{\max}(kR)$, the angle to the edge of the scattering aggregation. For comparison, the expected peak ratio from the beamformed output of the proposed coherence function is also indicated at 90 degrees (triangle). Quadratic (- - - - -) and power law (– – – –) fits to the peak ratios for the different angles are shown. By extrapolating, the enhancement at 90 degrees is 1.030±0.005. The enhancement obtained from the coherence function is at 1.034.

To overcome angular-resolution differences, the extrapolated acoustic simulation CBE results are compared with experimental optics CBE results via a postulated coherence function that is appropriately integrated to separately match the different angular resolutions of the simulations and the experiments. This postulated coherence function was composed of an omndirectional diffuse-field component represented by a sinc function, and a CBE component, represented by a Lorentzian, a functional form used to model the CBE component since it leads to a reasonable match with the peak shapes reported in Wolf et al. (1988):

$$\Gamma(k\Delta y) \equiv \left\langle p_j p^*_{j'} \right\rangle = A_d \frac{\sin(k\Delta y)}{k\Delta y} + A_b \left(1 + \left(k\Delta y / k\sigma_y\right)^2\right)^{-1} \tag{3-5}$$

where $\Delta y = y - y'$. Here, the diffuse and CBE component coefficients, A_d and A_b, respectively, were first adjusted to match the extrapolated results from the acoustic simulations, and then along with $k\sigma_y$, the width parameter, all three parameters were fine tuned to match both the results from the optics experiments as well as the acoustics simulations. Additionally, because of the polarization effects in the optics experiments, only the Δy dependence of Γ is considered. The resulting parameter values are $A_d = 1.85\times10^{-2}$, $A_b = 3.2\times10^{-5}$, and $k\sigma_y = 400$, and they allow (3-5) to be used in the integral form of (3-4) to determine $B(\phi)$. By evaluating (3-4) for J = 81 (kL = 64), the solid extrapolated CBE curve on Fig. 3-8 is produced where $B(0)/[B(\phi)]_{not\ peak}$ = 1.034. Thus, (3-5) is consistent with the simulation results extrapolated to an effectively infinite aggregation.

To determine if (3-5) was also consistent with the experimental optics CBE results, it was combined with (3-4) and numerically evaluated for an array length (kL = 12,566) and angular resolution (0.5 mrd, half width) equivalent to that of the goniometer used in the optics experiments. The diffuse portion of the coherence function (the sinc term) gives the upward shift by A_d and the backscattered portion (Lorentzian) sets the peak height by A_b. Here, $kL >> k\sigma_y$, so the width of the CBE peak is primarily set by the backscattered field. The resulting plot is similar in shape to that reported in Wolf and Maret (1985) and Wolf et al. (1988). In addition, the theoretical predictions provided in Akkermans et al. (1986) correspond to the resolution, $kL \to \infty$. So, by appropriately choosing kL, (3-4) and (3-5) facilitate quantitative comparisons of all three types of CBE results.

This overall comparison is provided in Fig. 3-11 where $B(\phi)/[B(\phi)]_{not\ peak}$ is plotted versus the beam steering angle ϕ for the CBE measurements of Wolf et al. (1988) (long dash curve), for the theoretical result of Akkermans et al. (1986) (short dash curve), and for the postulated coherence function (3-5) integrated to match the resolution of the optics experiments using (3-4) (solid curve). The optics measurement and the coherence function results agree well and suggests that the current acoustic CBE simulations are consistent with the prior optical measurements. The small difference between the measured-optical and coherence-function CBE peaks is likely due to the effect of absorption, finite scatterer size and directional scattering which were present in the experiments but were absent in the simulations. In addition, Fig. 3-11 also shows that the theoretical CBE peak is somewhat taller and narrower than the other two, a discrepancy also noted by Wolf et al. (1988) that is not resolved in this thesis either.

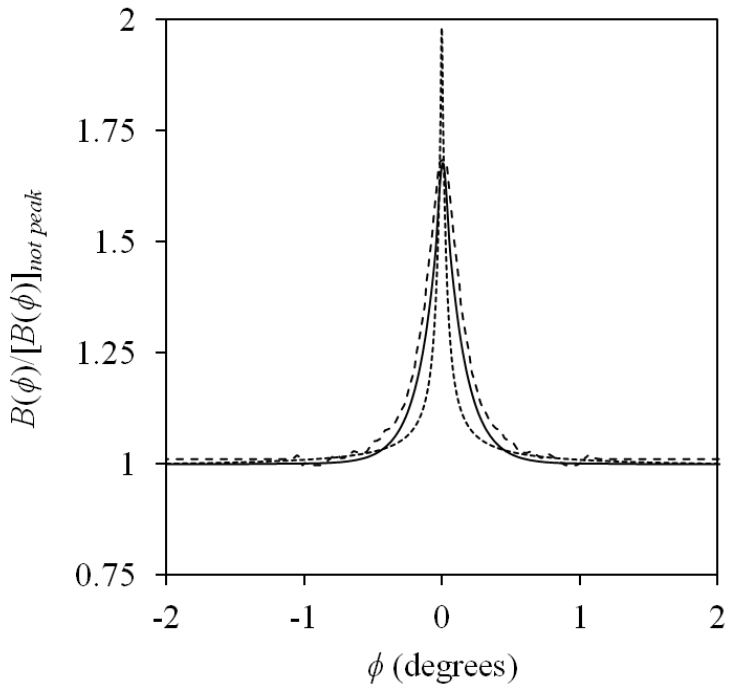

Figure 3-11: Normalized beamformed intensity vs. steering angle using the proposed coherence function at kL = 12566 (———), experimental results from Wolf et al. (1988) (– – – –) and theoretical results from Akkermans et al. (1986) (- - - - -). The close correspondence of the results from the proposed coherence function and the optical experimental suggests that the coherence function is consistent with both the current simulations and the prior experiments.

3. Replication of Near Field Experiments – Acoustics (Bayer and Niederdränk 1993)

To extend the validation further from an optics experiment to acoustics experiment, an existing ultrasound acoustics experiment from Bayer and Niederdränk (1993) is also replicated. Here the scatterers were gravel stones submerged in water, having an average wave number scaled diameter of kd = 50.3. In this parametric range, the scattering is nearly omnidirectional away from the forward direction. The mean free path provided by Bayer and Niederdränk (1993) was kl = 69.2 and the aggregation geometry was semi-infinite with depth and width larger than the mean free path. An ultrasonic receiver was used to measure the intensity, though no receiver

distance or receiver resolution was reported. As in the optics experiment replication, multiple realizations were considered and then an ensemble average was taken.

To simulate this experiment, the aggregation geometry shown in Fig. 3-7 was used with N = 5400 and dimensions of kX = 20, kY = 100 and kZ = 20. Here to expedite convergence (only 256-330 realizations were needed), the average scatterer spacing was reduced to ks = 1.95 and the scatterer strength was set to $k\sigma_s^{1/2}$ = 0.70 to achieve a mean free path of kl = 69.6 (close to the experimental value). In addition, a linear taper was added to the shadowed side of the aggregation from $-40 \leq kx \leq -20$, adding 2000 more scatterers to the back of the aggregation. Plus, the wave number scaled exclusion distance was reduced to kh = 1.1 to facilitate scatterer placement. The removed thickness, kt, and the receiving array properties remained unchanged from those used in replicating the Wolf et al. (1988) experiment.

Since Bayer and Niederdränk (1993) state that the experimental aggregation is a semi-infinite medium, the extrapolation to $\phi_{\max}(kR) \to 90°$, achieved via $kR \to 0$, was again undertaken. Figure 3-12 shows the change in $B(\phi)/[B(\phi)]_{not\ peak}$ vs. the beam steering angle ϕ for decreasing values of kR = 18.2 (- - - -), 15.2 (– • – • –), 13.2 (- - - - -), 11.2 (– – – –), 8.2 (- • - • - • -) and 5 (••••••••••). For comparison, the Bayer and Niederdränk (1993) experimental results (Figure 5 in their paper) are centered (a shift of 1.5°) and plotted (————) as well. Here a fitted extrapolation is not necessary since the simulation results for kR = 8.2 and 5 are well matched to the shifted experimental results with all three providing a CBE peak of 1.5. Thus, if the experimental and simulation resolutions are comparable, Figure 3-12 shows that the simulations agree with the acoustic CBE experimental results when the mean free path is matched.

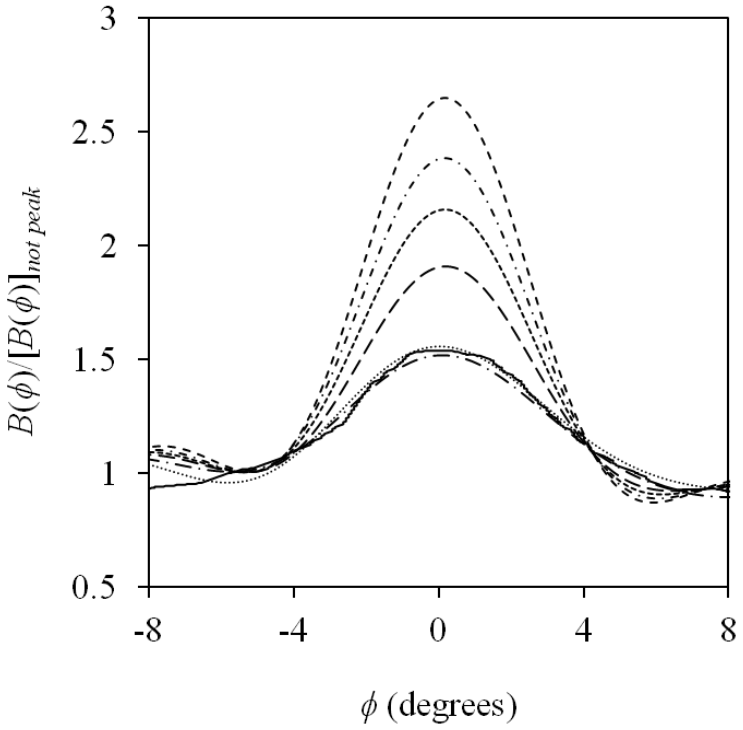

Figure 3-12: Normalized beamformed intensity vs. steering angle by replicating the Bayer and Niederdränk (1993) acoustics experiment for different receiving ranges: kR = 5 (••••••••••), 8.2 (- • - • - • -), 11.2 (– – – –), 13.2 (- - - - -), 15.2 (– • – • –), 18.2 (- - - -) and the Bayer and Niederdränk (1993) results (————), evaluated using kL = 64. Since no receiving resolutions are given in the Bayer and Niederdränk (1993) experiment, it is assumed that the receiving resolution in their experiment is comparable to that of the simulations. As the receiving array in the simulations are brought closer to the aggregation, the peak height decreases and approaches the results from the experiment with an enhancement of about 1.5.

3-3: Near field CBE Parametric Scaling

In the near field, for an infinite aggregation of point scatterers, ideally, the CBE peak height for any fixed receiving resolution should depend on average wave number scaled spacing between scatterers, *ks*, and the dimensionless scattering strength, $k\sqrt{\sigma_s}$. In order to determine if a single combination of the two parameters can control the CBE peak height, a parametric study showing how well simple algebraic combinations of *ks* and $k\sqrt{\sigma_s}$ could collapse peak height results to a single curve was undertaken for a set of 24 CBE simulations for the 3D rectangular

aggregation geometry shown in Fig. 3-7. The 3D rectangular geometry had dimensions kX = 64, kY = 100 and kZ = 20 and the scatterers were spaced in the range of $2.9 \le ks \le 6.4$ and had dimensionless scattering strengths in the range of $0.032 \le k\sqrt{\sigma_s} \le 3.544$. The receiving array considered was located a distance kR = 18.2 away and the length of the linear receiving array was kL = 64. This receiving range was selected since the simulation results converged with moderate computational effort (512 realizations) and the CBE peaks were distinct even for weak multiple scattering conditions.

Fundamentally, the coherent backscatter enhancement is a multiple scattering phenomenon. Mathematically, the importance of the scattered field in the Foldy (1945) equations increases when $k|g_1|$ is larger, which would occur for large $k\sqrt{\sigma_s}$, and when $k\left|\vec{r}_n - \vec{r}_j\right|$ is smaller, which would occur when ks is smaller. Therefore, the dependence of the CBE peak might follow a combined power law of the form of $(k\sqrt{\sigma_s})^m (ks)^{-n}$, where m and n are positive numbers. Assuming that this is an adequate combined dependence, the CBE peak ratios, scattering cross sections and average spacings for the 24 simulations were collected and plotted to find suitable values of the exponents m and n. The final result of this search is shown as Figure 3-13 where $B(0)/[B(\phi)]_{not\ peak}$ from each simulation is plotted versus $(k^2\sigma_s)^{1/4}(ks)^{-1}$. The mild scatter of the points may be caused by residual effects of the finite sized scattering aggregation and the fact that the peak height ratio may depend separately on ks and $k\sqrt{\sigma_s}$ and the parametric scaling $(k^2\sigma_s)^{1/4}(ks)^{-1}$ combines these parameters in a specific and slightly imperfect manner.

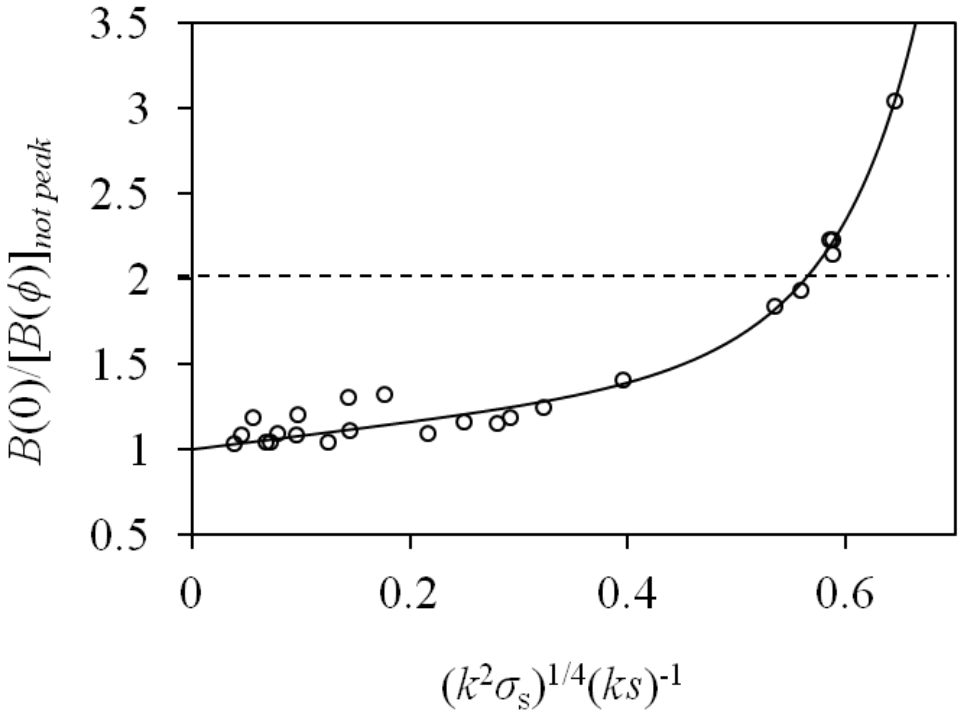

Figure 3-13: Simulated acoustic CBE peak heights $B(0)/[B(\phi)]_{not\ peak}$ versus $(k^2\sigma_s)^{1/4}(ks)^{-1}$ when $kX = 64$, $kY = 100$, and $kZ = 20$, $2.9 \le ks \le 6.4$ and $0.032 \le k\sigma_s^{1/2} \le 3.544$ for $kR = 18.2$. The simulated peak height increases approximately monotonically with $(k^2\sigma_s)^{1/4}(ks)^{-1}$. The mild scatter of the points is caused by the residual effects of the finite-sized scattering aggregation and the fact that the peak height ratio may depend separately on ks and $k^2\sigma_s$ while the ratio $(k^2\sigma_s)^{1/4}(ks)^{-1}$ combines these parameters

.

The results in Figure 3-13 are interesting for two reasons: (1) They suggest any parametric change that increases $(k^2\sigma_s)^{1/4}(ks)^{-1}$ will increase the prominence of the CBE peak height and (2) these results show that the CBE peak height can exceed the factor of two when the aggregation is of finite size. However, this parametric scaling is solely based on findings from simulation and there has yet to be any connections of the exponents with physical phenomena.

3-4: Summary and Conclusions

In this chapter, the fundamental equations for multiple scattering using the Foldy (1945) equations described in Chapter 2 have been solved numerically for structured and random

aggregations of scatterers. To ensure that the multiple scattering equations have been properly implemented, the simulations were verified via successful comparisons to scattering angles by Bragg scattering theory and wave number shifts calculated from Foldy's effective medium theory. To ensure that the simulations were predicting realizable acoustic fields, they were validated using acoustic energy conservation and through comparison with prior optical and acoustical experiments. Here the simulations were found to conserve acoustic energy better than one part in 10^4 even when there are thousands of strong scatterers and they produce results that are consistent with a coherence function that also matches the optical CBE experiments when geometrical and angular resolution differences are accounted for.

Five primary conclusions can be drawn from this chapter. (*i*) The field equations for multiple scattering provided in Foldy (1945) can be cast in dimensionless form and used for simulating the coherent backscatter enhancement. Although there has been previous work involving the Foldy equations and CBE using electromagnetic waves (Tsang et al., 1995), the present work is the first to show this to be true using omnidirectional point scatterers in acoustics (*ii*) The current simulations are properly implemented for point scatterers. The two verification tests and the two validation tests were all successful. In particular, it should be noted that the simulations conserve acoustic energy well for thousands of interacting scatterers even though Foldy's acoustic energy conservation requirement is only imposed on individual scatterers when isolated and subject to plane wave illumination. Plus, the second validation test with the optics experiment, although indirect, is the first attempt to quantitatively compare the results of optical CBE experiments and acoustic CBE simulations. To complete these comparisons, a coherent function for the scattered field was proposed and fitted, with some success, to the simulated and experimental results. (*iii*) The postulated coherence function may have value in describing

acoustic CBE in other circumstances when its parameters are appropriately adjusted. Here, the three constants in (3-5) must certainly depend on the dimensionless average scatterer spacing ks and scattering strength $k\sigma_s^{1/2}$, and the values provided in Section 3-3 likely only pertain to this study. However, the form of (3-5) may be general enough to apply in other circumstances. Additionally, the extent of the beamforming integration of the coherence function described in (3-4) determines when the receiving array sets the observed CBE peak width ($kL << k\sigma_y$) and when the backscattered field sets the observed CBE peak width ($kL >> k\sigma_y$). (*iv*) Acoustic CBE experiments can also be replicated using the Foldy (1945) equations. The current simulations produce CBE peak heights and widths for a semi-infinite medium which are nearly the same as experimental results, assuming that the receiving resolutions are comparable. (*v*) The height of the CBE peak appears to monotonically increase with $(k^2\sigma_s)^{1/4}(ks)^{-1}$. This parametric result is consistent with the notion that increased multiple scattering effects will occur when the scatterers are stronger and closer together. However, the exponents (1/4, –1) in this combined parameter can only be readily determined from broad parametric studies from simulation, like the ones reported here. The identification of such scaling exponents from experiments would be more difficult.

CHAPTER 4

Far Field Single Frequency Coherent Backscatter Enhancement

This chapter starts to address some of the concerns which may be of interest to the U.S. Navy and the remote sensing applications where CBE could be applicable by considering single frequency signals for multiple realizations of positions of the scatterers (In Chapter 5, broadband pulses in the form of frequency sweeps are simulated). It begins by first considering the near field simulation setup and geometry and gradually modifying the geometry by backing up the linear receiving array and replacing it with a receiving ring in the far field of the aggregation. The rectangular aggregation is then replaced by a spherical or spheroidal aggregation geometry. These aggregation geometries are typical for fish schools (Partridge, 1980). The Foldy (1945) equations are still utilized. The dependence of the CBE peak width on the aggregation geometry and size is considered by studying spherical aggregations of different radii and spheroidal aggregations in different orientations.

In order to understand the dependence of the strength of the CBE peak, a parametric study is done by considering a spherical aggregation and separately varying the wave number scaled aggregation size, the wave number scaled average spacing between scatterers, and the wave number scaled dimensionless scattering strength of a single scatterer. The backscattered returns from an aggregation of scatterers are compared with that of a single idealized (no fluid structure interaction) hard and soft sphere in the free space. This is done by matching the mean

square pressure in the backscatter direction for the aggregation of scatterers, $<|p_s(0)|^2>$, with the backscattered pressure magnitude-squared from a soft or hard sphere, $|p_s(0)|^2$, which was obtained using the van Bladel (1968) form of the Morse and Ingard (1968) equations. Comparisons are also done for prolate and oblate spheroids with soft and hard spheres. Modifications are made to the parametric scaling in Chapter 3 to consider the effect of aggregation geometry. Additionally, the magnitude of the average pressure in the backscatter direction from the aggregation of scatterers is compared with the formulae for the magnitude of the backscattered pressure from an ideal sphere have the effective medium properties of the aggregation (Hahn 2007) as a function of the small parameter, $\left|4\pi(kg_1)^2/(ks)^3\right|<<1$, briefly discussed in Chapter 2 in (2-10) and also in Frisch (1968). The backscatter results from these simulations are considered and discussed in the first part of Chapter 6. For simplicity, $p_s = \sum_j kg_1 \frac{p_j(k\vec{r}_j)}{A} \frac{G(k\vec{r},k\vec{r}_j)}{k}$, or the scattered pressure from evaluating the normalized form of the Foldy (1945) equations.

These types of single scattering objects were considered for several reasons: (*i*) Spheres are the simplest three dimensional objects. (*ii*) The hard and soft spheres have perfectly reflecting surfaces and are strong scatterers. (*iii*) Comparing to spheres eliminates the need to specify distances when comparing backscattering strength. (*iv*) The backscattered mean square pressure from a single isolated sphere is deterministic. (*v*) The scattering from ideal spheres can be easily used to compare with single isolated manmade objects. A portion of this chapter has been recently accepted by the Journal of the Acoustical Society of America.

4-1: From Near Field to Far Field

In Chapter 3, the near field CBE simulation geometry consists of a 3D rectangular aggregation with dimensions kX by kY by kZ and a linear receiving array a distance kR away from the aggregation with length kL (see Figure 3-8). In the scenario considered in Chapter 3, Rayleigh far field parameter ($kY^2/4R$) is significantly greater than 1. In this section, gradual modifications are made to the simulation geometry to account for the changes as the receiving geometry is brought to the far field of the aggregation ($kY^2/4R << 1$) and the aggregation geometry is modified to be more realistic to better model a school of fish. First, modifications are made to the receiving geometry by increasing the receiving range in factors of four until the Rayleigh far field parameter is much less than 1 and then the linear receiving array is replaced with a receiving ring like that considered in Chapter 3 for the Bragg scattering simulations. To follow, modifications are made to the aggregation of scatterers by changing the 3D rectangular aggregation into a spherical aggregation and increasing the scattering strength.

Here, the aggregation considered to replicate the optics experiment is considered. This aggregation has dimensions of $kX = 64$, $kY = 100$ and $kZ = 20$ and the linearly decreasing taper with dimensions of $kX = 20$ by $kY = 100$ by $kZ = 20$ is used. The dimensionless scattering strength of each individual scatterer composing the aggregation is $k\sigma_s^{1/2} = 0.21$ and the spacing between the scatterers is $ks = 3.2$. Figure 4-1 shows the normalized beamformed intensity, $B(\phi)/[B(\phi)]_{\text{not peak}}$ as a function of steering angle ϕ. The receiving range originally considered is $kR = 18.2$ and the normalized beamformed intensity is shown as the black solid line (—) in Figure 4-1. Receiving ranges are increased in factors of four until $kR \sim 74{,}000$ or the Rayleigh

far field parameter is 0.0338 (— • — • — in Figure 4-1). All of these simulations required 512 samples.

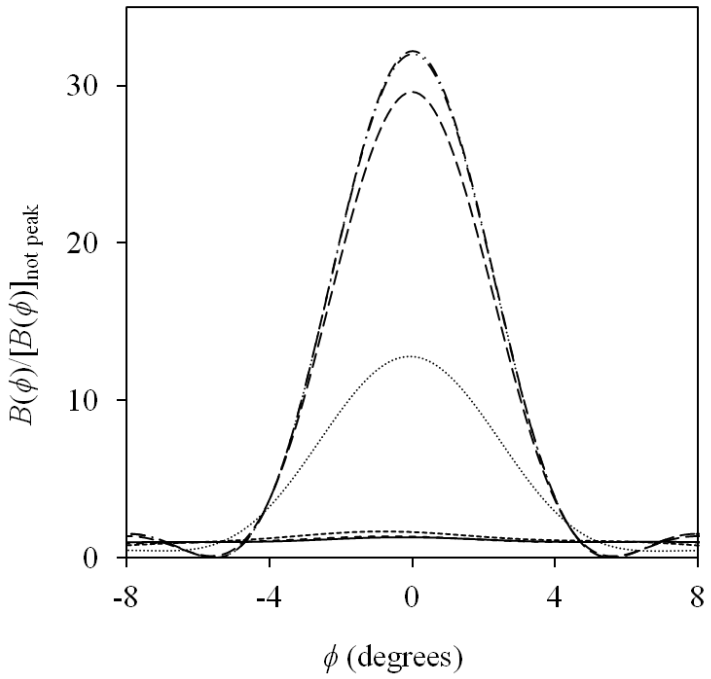

Figure 4-1: Effect on the CBE peak as the receiving range *kR* is increased. As the receiving range is increased, the peak height also increases. This is because the angular width of the finite-size aggregation decreases as the aggregation-array range increases until the aggregations appears as a single scatterer at the origin. In this case, there is no radiation coming from other directions, so $[B(\phi)]_{\text{not peak}}$ becomes the side-lobe level of the receiving array.

In Figure 4-1, the height of the peak at $\phi = 0$ increases as the receiving range increases from a factor of 1.25 to 30. Additionally, the sides of the peak at around 5 degrees touch at normalized beamformed intensity of 0, unlike beamformed intensity curves for smaller receiving ranges, where the plot levels off to 1 at the sides of the peak. Consequently, the linear array responds to the aggregation of scatterers at the origin as a single scattering object for large receiving ranges and thus, it becomes less sensitive to the properties of the aggregation. As a result, an alternate simulation geometry is needed which is sensitive to variations in

dimensionless scattering strength, wave number scaled scatterer spacing, and any other properties which may influence the multiple scattering effects in the far field.

In the far field, a receiving ring is considered instead of the linear receiving array. Additionally, rather than considering the beam steering angle, ϕ, which was utilized in Chapter 3, the azimuthal angle, φ, is used to evaluate the returns at the different angles (shown in Figure 4-2). The Foldy (1945) equations are evaluated on the receiving ring for each angle φ and a pressure magnitude squared is obtained. For the CBE plots, the ensemble average of the pressure magnitude squared is taken to yield a mean square pressure and the mean square pressure is normalized by the mean square pressure in the backscatter direction, unlike in Chapter 3 where the beamformed intensity was normalized by the beamformed intensity excluding the peak. The convention of the normalization was changed in the far field, because it was observed that the far field CBE peak results depend on the geometry which is in agreement with the expectation. Additionally, because of this influence of geometry on the CBE peak, the angular range considered is $-90 \leq \varphi \leq 90$ degrees (as opposed to $-8 \leq \phi \leq +8$ degrees in the near field studies). This will be discussed in greater detail in sections 4-2 and 4-3 of this chapter. The scattering aggregation is the same as discussed.

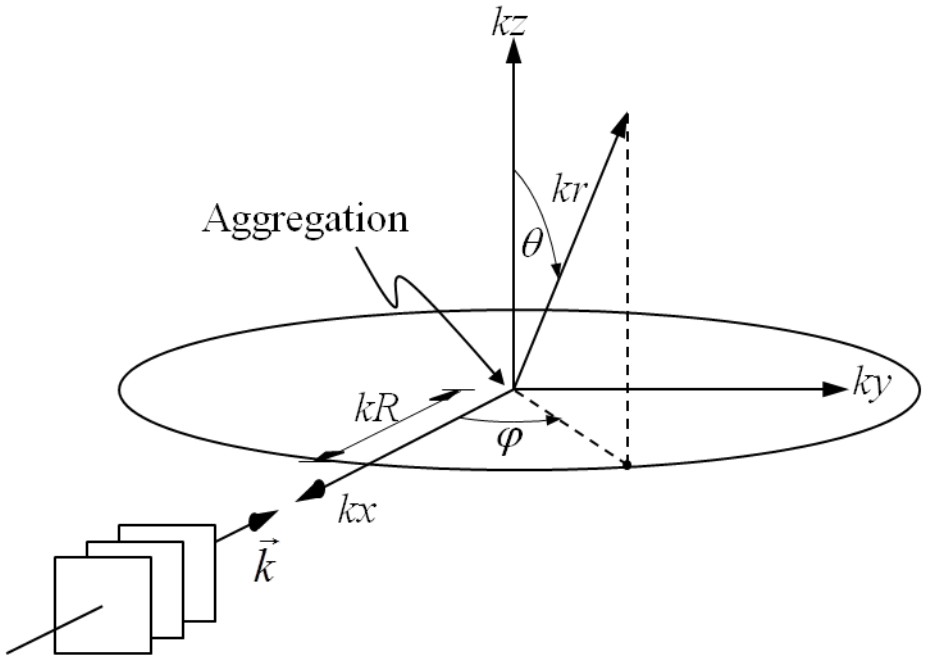

Figure 4-2: Simulation geometry. The aggregation (not shown) is centered at the origin and a plane wave with wave number vector $\vec{k}$ illuminates the aggregation of scatterers. The scattered sound field is received in the far-field of the aggregation on a ring of radius *R* lying in the *x-y* plane The scattering angle φ is measured in the *x-y* plane from the backscatter direction defined by $\varphi = 0°$ and $\theta = 90°$.

In Figure 4-3, the normalized mean-square pressure is plotted as a function of angle, φ for the 3D rectangular aggregation obtained via the far field receiving ring with 512 realizations. A peak appears even with this new receiving geometry. Additionally, unlike the results obtained via plane wave beamforming, while a peak at 0 degrees does occur after 512 realizations, in order to have the simulation results be nominally symmetric and smooth, it appears that 512 realizations may not be enough for full convergence and possibly thousands of realizations may be required. This is due to the fact that beamforming is less sensitive to random scattering fluctuations (Aubry et al. 2007) and therefore, fewer realizations are needed to obtain a nominally symmetric and smooth curve.

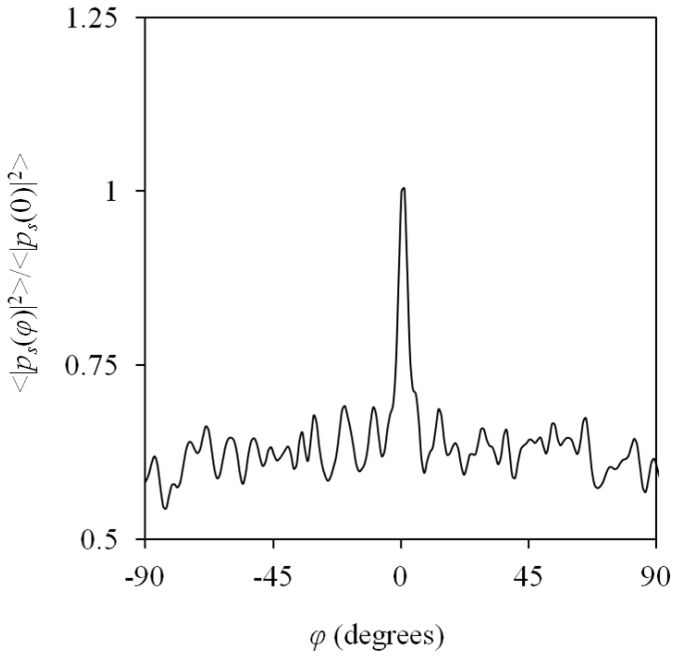

Figure 4-3: Normalized mean square pressure for the 3D rectangular aggregation in Chapter 3. For the 3D rectangular aggregation considered in the near field, a very narrow and prominent peak occurs in the far field as well.

Since an objective of this thesis is to model schools of fish, the aggregation is modified to appear more typical to that of a school of fish, so the 3D rectangular aggregation is replaced with a spherical aggregation. The aggregation has radius of ka = 32, the same scatterer properties as the 3D rectangular aggregation (ks = 3.2 and $k\sigma_s^{1/2}$ = 0.21), resulting in 4200 scatterers, and the same receiving ring radius. Figure 4-4 shows the normalized mean square pressure as a function of the azimuthal angle, φ, in degrees for the spherical aggregation. As expected, thousands of realizations were required for nominal convergence. Interestingly, the shape of Figure 4-4 also changed with the modification of the aggregation geometry. Firstly, the CBE peak at φ = 0 is no longer present unlike in the case of Figure 4-3. Additionally, while the side ripples in the normalized mean square pressure plot for the rectangular aggregation at $\varphi \neq 0$ levels off at $<|p_s(\varphi \neq 0)|^2>/<|p(0)|^2>$ = 0.6, the mean square pressure plot in Figure 4-4 does not do that and instead

curves downward. This suggests that the aggregation geometry also plays a role in the angular dependence of the normalized mean square pressure in the far field.

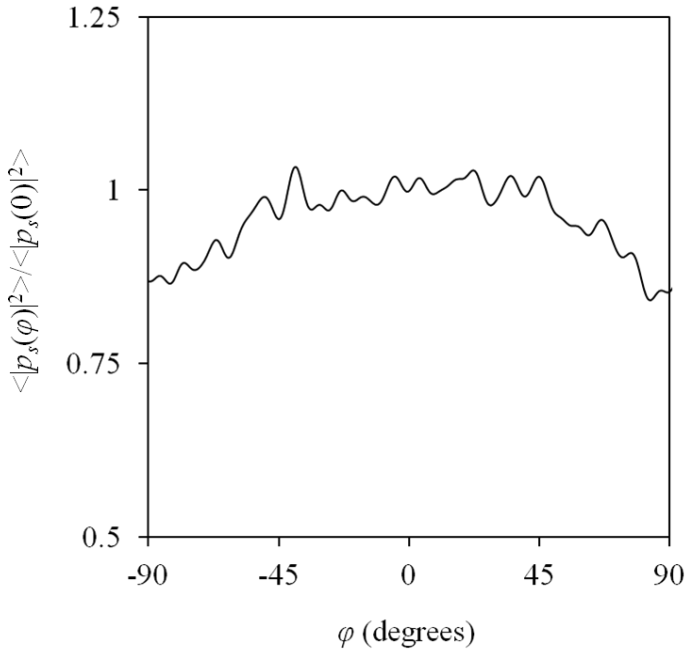

Figure 4-4: Normalized mean square pressure for a spherical aggregation with ks = 3.2 and $k\sigma_s^{1/2}$ = 0.21. When the 3D rectangular aggregation is replaced with a spherical aggregation, an aggregation geometry common to fish schools (Partridge 1980), the CBE peak disappears. This suggests that the aggregation geometry may also describe the prominence in the CBE peak in the far field.

Since the current aggregation conditions do not produce a CBE peak, the dimensionless scattering strength was increased to $k\sigma_s^{1/2}$ = 1.5 while the keeping all other parameters fixed. This yields a distinct CBE peak shown in Figure 4-5 with a similar shape in the plot as in Figure 4-4 at the angles not at the peak. This suggests that the geometry of the aggregation plays an important role in the CBE peak width. While the work in this thesis primarily focuses on understanding the peak effects from aggregation geometries which are typical to fish schools,

additional analysis could also be performed to understand the peak effects for aggregation shapes which are more atypical to fish schools.

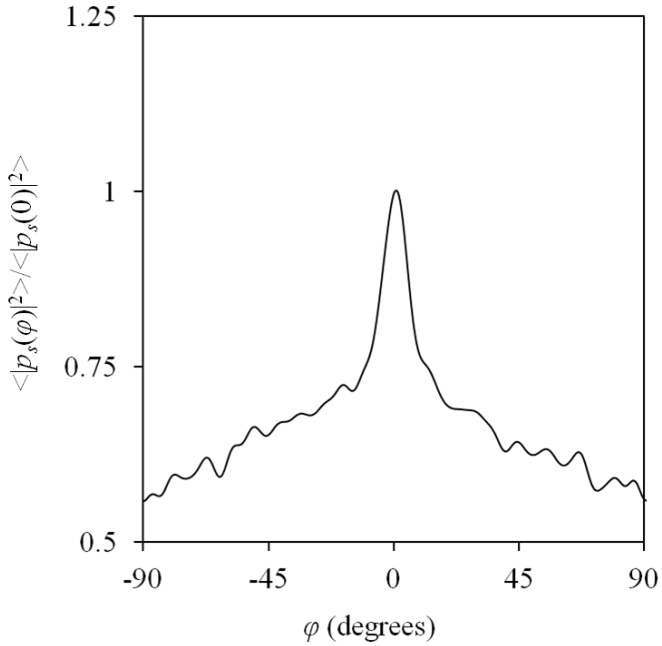

Figure 4-5: Normalized mean square pressure for a spherical aggregation with ks = 3.2 and $k\sigma_s^{1/2}$ = 1.5. Increasing the dimensionless scattering strength up to 1.5 returns a very prominent CBE peak.

4-2: Simulation Setup

In this chapter, the Foldy (1945) equations are evaluated for three different aggregation geometries: (1) spheres, (2) oblate spheroids (enlarged in the equatorial plane perpendicular to the axis of rotational symmetry) and (3) prolate spheroid (elongated along the axis of rotational symmetry). The aggregations were generated by first randomly placing point scatterers in an enclosing cube or rectangular prism centered at the origin with a distance h between scatterers of at least kh = 1.6. Then, scatterers which were outside of the desired spherical or spheroidal geometry were removed. The size of the aggregations is set by the dimensionless parameter ka,

where a is the radius of the spherical aggregations, and the spherical-volume-equivalent radius of the spheroidal aggregations.

Spherical aggregations were considered to determine how the CBE peak width and height depend on ka, ks, $k\sigma_s^{1/2}$ and also for comparisons with scattering from single non-compact spheres having ideal hard and pressure-release (or soft) spherical-surface boundary conditions (discussed in Chapter 2) without fluid-structure interactions. Three parameter studies involving different dimensionless aggregation radii (ka = 12, 16, 25 and 32), dimensionless scatterer spacings (ks = 6.4, 4.8, 3.2 and 2.9), and dimensionless scatterer strengths ($k\sigma_s^{1/2}$ = 0.38, 0.75, 1.5, and 3.0) were undertaken. The parameters for the baseline aggregation were ka = 16, ks = 3.2 and $k\sigma_s^{1/2}$ = 1.5, and this aggregation involved 524 scatterers.

For the simulations involving the spheroidal aggregations, the orientation of the axis of symmetry was separately set parallel to the kx, ky and kz coordinate axes to identify the effect of elementary orientation changes on the CBE peak. For the oblate spheroids, the dimensionless equatorial and polar radii were ka_e = 32 and ka_p = 16, respectively. For the prolate spheroids, the dimensionless equatorial and polar radii were ka_e = 16 and ka_p = 32, respectively. Fixed values of ks = 3.2 and $k\sigma_s^{1/2}$ = 1.5 were used for all simulations involving spheroidal aggregations.

4-3: Far-Field CBE Peak Width

This section provides CBE peak width results and comparisons for spherical and spheroidal aggregations in terms of the normalized average mean square scattered field

amplitude $\left\langle \left| p_s(\varphi) \right|^2 \right\rangle \Big/ \left\langle \left| p_s(0) \right|^2 \right\rangle$. This normalization suppresses variations in CBE peak strength so that CBE peak width changes are more readily apparent.

Far-field backscattering results for spherical aggregations with dimensionless radii *ka* = 12, 16, 25 and 32, are shown in Figure 4-6 for *ks* = 3.2 and $k\sigma_s^{1/2}$ = 1.5. The number of scatterers and realizations comprising these results are as follows: 220 and 100,000 for *ka* = 12, 524 and 7449 for *ka* = 16, 2000 and 6144 for *ka* = 25 and 4200 and 4524 for *ka* = 32, respectively. The results in Figure 4-6a) show that a CBE peak appears in all four cases and that this peak is nominally symmetrical about φ = 0; additional realizations merely improve this symmetry. Furthermore, the CBE peaks monotonically narrow as *ka* increases, and this narrowing is directly related to the size of the aggregation as shown in Figure 4-6b) where the CBE peaks collapse nicely to a single curve for $|ka\varphi| \leq 5$ when φ is measured in radians. Therefore, in the far field of a spherical aggregation, the CBE peak width $\Delta\varphi$ is proportional 1/*ka*, a result that is consistent with diffraction-limited radiation from a non-compact spherical source distribution. Furthermore, with *ka* fixed, variations in *ks* and $k\sigma_s^{1/2}$ produced no discernible variations in CBE peak width; such variations only altered the strength of the CBE peak.

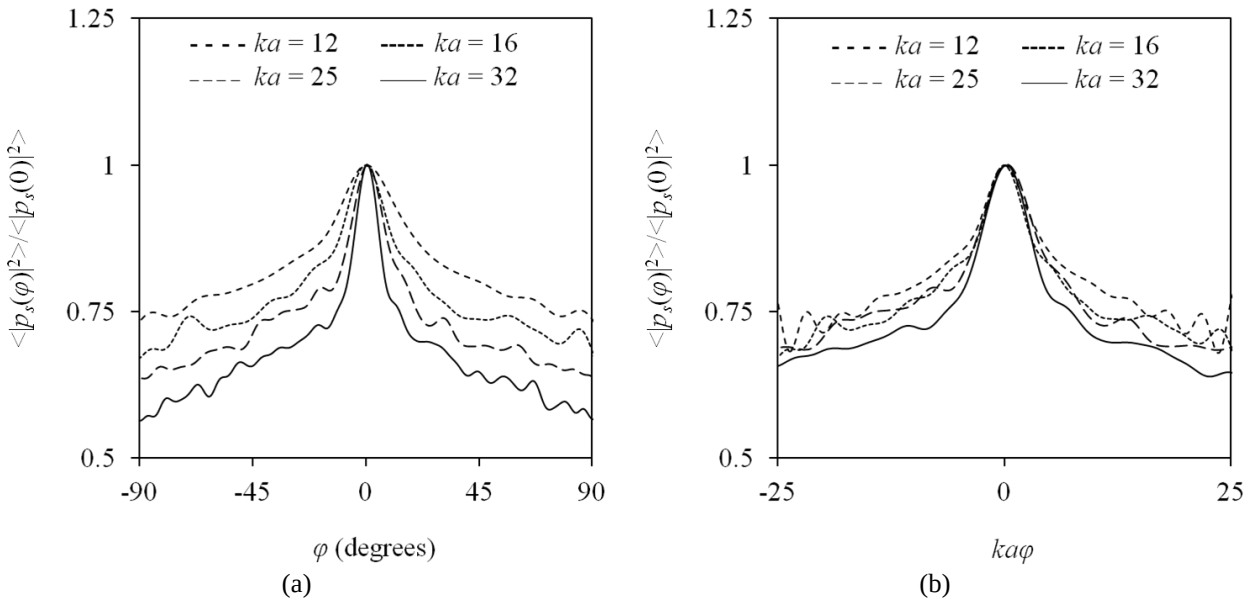

Figure 4-6: Normalized mean square pressure $\left\langle \left| p_s(\varphi) \right|^2 \right\rangle / \left\langle \left| p_s(0) \right|^2 \right\rangle$ versus scattering angle φ in degrees (a), and versus the product of the dimensionless aggregation radius *ka*, and the scattering angle φ, when φ is measured in radians (b). The results are for spherical aggregations with *ka* = 12, 16, 25, and 32 composed of scatterers spaced an average distance *ks* = 3.2 apart and having scattering strength $k\sigma_s^{1/2}$ = 1.5. As *ka* increases, the CBE peak narrows, but, as shown in (b), all four CBE peaks collapse when plotted vs. $ka\varphi$. This suggests that the aggregation's acoustic size, represented here by *ka*, sets the width of the CBE peak.

Results for the 2-to-1 oblate and prolate spheroidal aggregations in different orientations are shown in Figures 4-7 and 4-8, respectively. Here, the number of scatterers and realizations for these results are 2100 and 4096-4227 for oblate spheroids and 1050 and 4401-9050 for prolate spheroids, respectively. There are three curves on each plot corresponding to the orientation of the spheroidal axis of symmetry lying along the *kx* (——), *ky* (— — — —) and *kz* (- - - -) coordinate directions. The oblate spheroid results in Figure 4-7 show that the CBE peak is narrower when the shorter polar axis is parallel to the *kx* and *kz* directions, while it is wider when the shorter polar axis is parallel to the *ky* direction. The prolate spheroid results in Figure 4-8 show that the CBE peak is narrower when the longer polar axis is parallel to the *ky* direction, while it is wider when the longer polar axis is parallel to the *kx* and *kz* directions. For both types of spheroids, the CBE peak is narrower (wider) when the aggregation has a larger (smaller)

geometric extent along the *ky* axis, a finding that is expected for diffraction-limited far-field radiation.

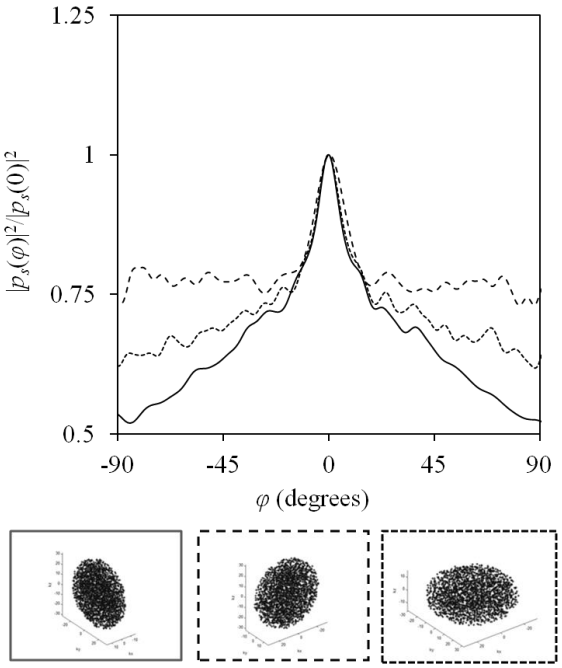

Figure 4-7: Same as Fig. 4-6 but for oblate spheroidal aggregations with equatorial radius ka_e = 32 and polar radius ka_p = 16 in three different orientations where the shorter polar axis was parallel to the *kx* (———), *ky* (– – – –), and *kz* (- - - - -) coordinate directions. These aggregation orientations are depicted below the plot. Depending on the orientation of the aggregation, the width of the CBE peak changes, further confirming that the aggregation geometry sets the width of the CBE peak.

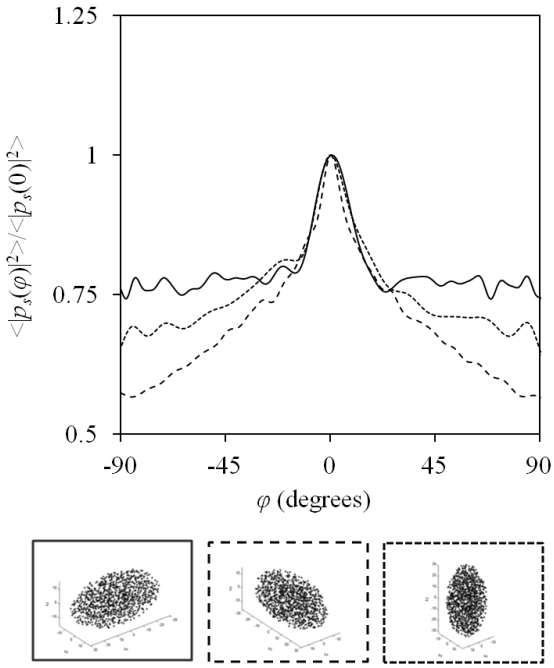

Figure 4-8: Same as Fig. 4-6 but for prolate spheroidal aggregations with equatorial radius ka_e = 16 and polar radius ka_p = 32 in three different orientations where the longer polar axis was parallel to the *kx* (———), *ky* (– – – –), and *kz* (- - - - -) coordinate directions. These aggregation orientations are depicted below the plot. Depending on the orientation of the aggregation, the width of the CBE peak changes, further confirming that the aggregation geometry sets the width of the CBE peak.

For both spherical and spheroidal aggregations, the back-propagating CBE radiation peak width approaches the narrowest possible radiation beam width that could be made by the aggregation if each scatterer were replaced by an omni-directional point source that radiates with the phase necessary to produce a back-propagating plane wave. In order to test this peak width claim, separate simulations were completed with this scatterer-to-back-propagation-phased-source replacement. The resulting curves of $\langle|p_s(\varphi)|^2\rangle/\langle|p_s(0)|^2\rangle$ are shown in Fig. 4-9 where the solid line is for the scatterers and the dashed line is for the back-propagation-phased sources. The vertical dashed lines are at ±11.25° and show that the peak widths agree. This indicates that the far-field CBE peak width depends on the aggregation's size and shape in the same way that sound radiated from an equivalent retro-directive distribution of acoustic sources depends on the distribution's size and shape.

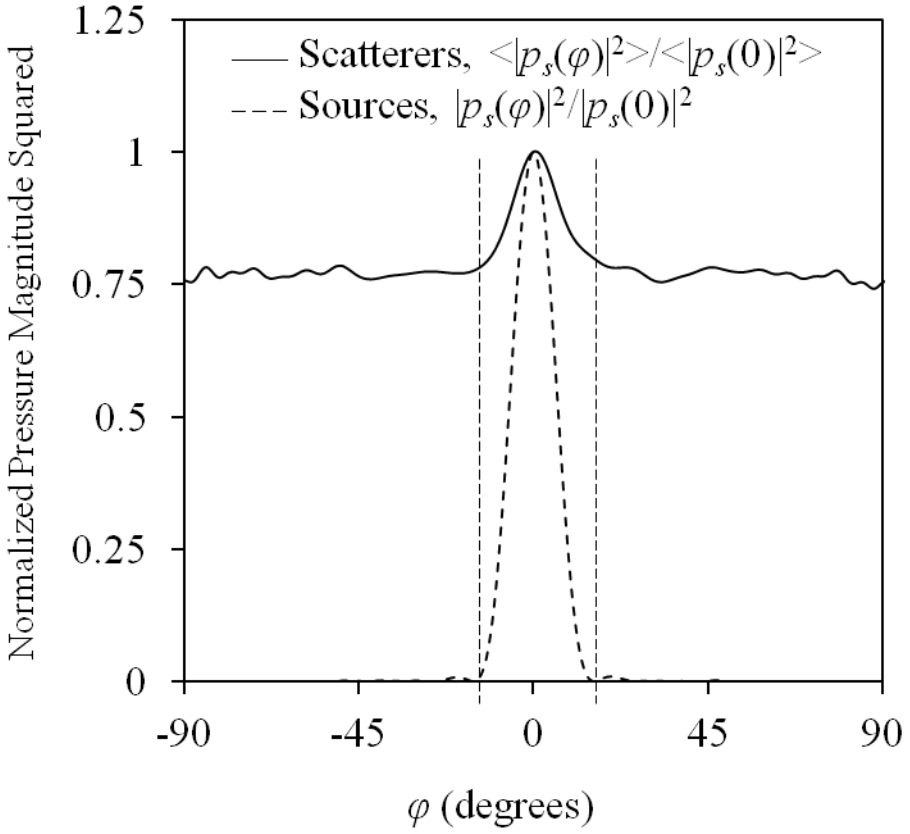

Figure 4-9: Sample comparison in the peak width of an aggregation of omnidirectional point scatterers from an oblate spheroid having ks = 3.2 and $k\sigma_s^{1/2}$ = 1.5 with an aggregation of omnidirectional point sources with their phasing set so that their radiation is retrodirective vs. the scattering angle, φ. Vertical dashed lines at ±11.25° ($2\pi/ka$ in degrees) show that the widths of the peaks from an aggregation of scatterers and from an aggregation of omnidirectional retrodirectively-phased sources are comparable.

4-5: Far Field CBE Peak Strength

In Chapter 3, the strength of the CBE peak was reported as a ratio of the mean square pressure backscattered by the aggregation, $\left\langle |p_s(0)|^2 \right\rangle$, and the spatially averaged mean square pressure the aggregation scatters into small nonzero angles near the backscatter direction, $\left\langle |p_s(\varphi)|^2 \right\rangle_{not\ peak}$. However, as shown in Figures 4-6-4-8 for 20° ≤ |φ| ≤ 90°, $\left\langle |p_s(\varphi)|^2 \right\rangle_{not\ peak}$

depends on φ and is not a consistent well-defined level in the far-field of the spherical and spheroidal aggregations. Thus, peak CBE backscattered radiation was compared to backscattered radiation from ideal hard and soft spheres as calculated from (2-16) for $\beta_m \rightarrow 0$ and $\beta_m \rightarrow \infty$, respectively. These comparisons were made in three ways. First, the backscattered pressure magnitude squared from ideal hard ($|p_s(0)|^2_{hard}$) and soft ($|p_s(0)|^2_{soft}$) spheres were matched to $\left\langle |p_s(0)|^2 \right\rangle$ from the aggregation by adjusting the radii of the ideal spheres. In this case, the relative sizes of the aggregation and the spheres indicate the aggregation's backscattering strength. And second, the ratio of $\left\langle |p_s(0)|^2 \right\rangle$ from the aggregation to the average of the backscattered pressure magnitude square from equal sized ideal hard and soft spheres was calculated to determine when backscattering from the aggregation is likely to be stronger than that from a single equivalent-size object. The final method involved use of the Hahn (2007) formulation using the effective medium theory discussed in Chapter 2 and used as a verification technique in Chapter 3.

The first set of CBE peak strength comparisons involving matched backscattered sound from ideal spheres are shown in Figures 4-10, 4-11 and 4-12, where the $\left\langle |p_s(\varphi)|^2 \right\rangle$, $|p_s(\varphi)|^2_{hard}$, and $|p_s(\varphi)|^2_{soft}$ are plotted versus φ for $-90° \leq \varphi \leq +90°$ when $|p_s(0)|^2_{hard}$ and $|p_s(0)|^2_{soft}$ are separately matched to $\left\langle |p_s(0)|^2 \right\rangle$. In these three figures, variations are individually made in *ka*, *ks* and $k\sigma_s^{1/2}$ to illustrate what happens as the prevalence of multiple scattering increases. In all these figures, the results for the aggregations are given by solid curves while those for the hard and soft spheres are given by longer and shorter dashed curves respectively. And, as a further

distinguishing feature, $|p_s(\varphi)|^2_{hard}$ shows more variation in the plotted angular range than $|p_s(\varphi)|^2_{soft}$ because of the Bessel function derivatives discussed in Chapter 2.

The results provided by the three figures are as follows. Figure 4-10 shows the normalized CBE peak results when the spherical aggregation's radius is *ka* = 12 and 32, for *ks* = 3.2 and and $k\sigma_s^{1/2}$ = 1.5. In Figure 4-10a), the radii of the backscatter equivalent hard and soft spheres (*ka* = 10.5 and 10.3), are smaller than that of the aggregation (*ka* = 12). However, in Figure 4-10b), the radii of the backscatter equivalent hard and soft spheres (*ka* = 39.7 and 39.7), are larger than that of the aggregation (*ka* = 32).

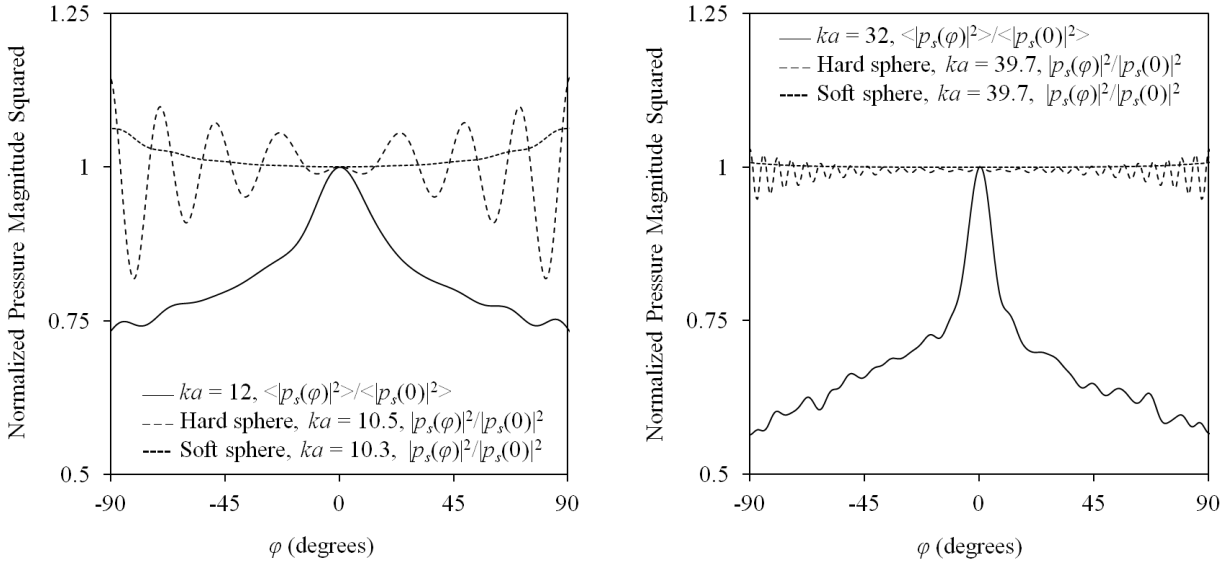

Figure 4-10: Comparisons between mean-square scattered pressure $\left\langle |p_s(\varphi)|^2 \right\rangle$ from spherical aggregations of scatterers having *ks* = 3.2 and $k\sigma_s^{1/2}$ = 1.5, and that from backscatter-equivalent ideal hard and soft spheres, calculated from (2-14) when $\beta_n \to 0$ and $\beta_n \to \infty$, respectively, all divided by $\left\langle |p_s(0)|^2 \right\rangle$ vs. the scattering angle φ. This normalization requires all curves to pass through (0,1). In (a), the aggregation's radius is *ka* = 12, and the radii of the backscatter-equivalent hard and soft spheres are *ka* = 10.5 and 10.3, respectively. In (b), the aggregation's radius is larger, *ka* = 32, and the radii of the backscatter-equivalent hard and soft spheres are both *ka* = 39.7. These results suggest that an increase in the aggregation size for fixed dimensionless scattering strength and scatterer spacing yields an increase in the multiple scattering effects (a more prominent CBE peak). Consequently, the aggregation is larger than the backscatter-equivalent hard and soft spheres in (a), but this size relationship switches in (b).

Figure 4-11 shows normalized CBE peak results when the aggregation's average spacing between scatterers is ks = 6.4 and 2.9, for ka = 16 and $k\sigma_s^{1/2}$ = 1.5. In Figure 4-11a), the CBE peak is weak, and the radii of the backscatter-equivalent hard and soft spheres (ka = 6.9 and 6.7) are smaller than that of the aggregation (ka = 16). However, in Figure 4-11b) the CBE peak is more apparent and the radii of the backscatter equivalent hard and soft spheres (ka = 16.6 and 16.9) are slightly larger than that of the aggregation (ka = 16).

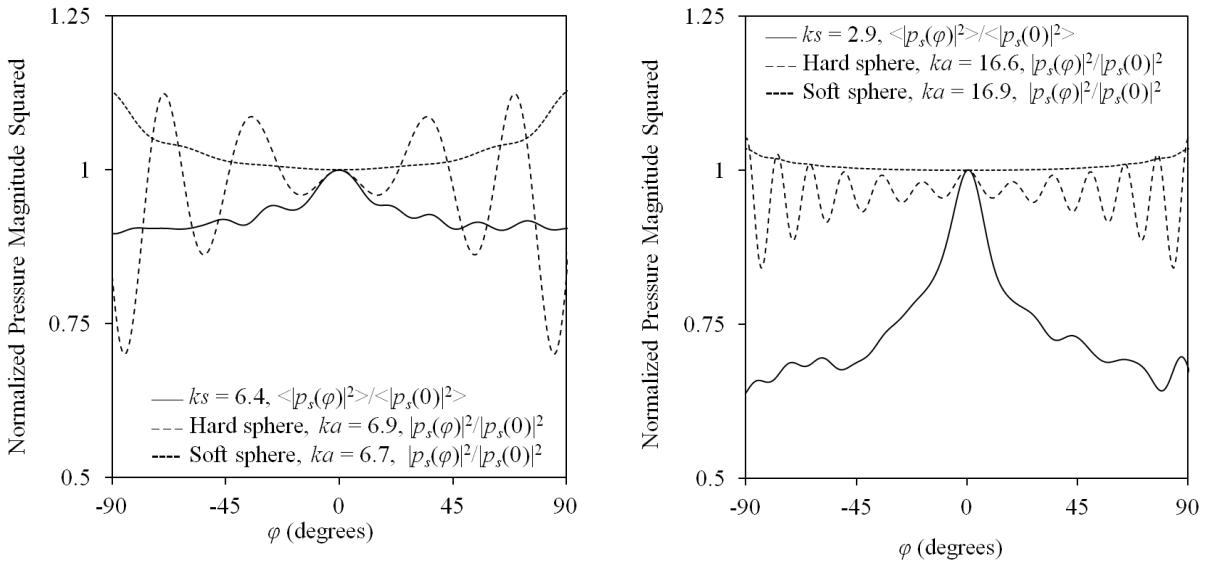

(a) (b)

Figure 4-11: Same as Fig. 4-10, except ka = 16, $k\sigma_s^{1/2}$ = 1.5 and the average spacing between scatterers ks is varied between (a) and (b). In (a), ks is 6.4, and the radii of the backscatter-equivalent hard and soft spheres are ka = 6.9 and 6.7, respectively. In (b), ks is 2.9, and the radii of the backscatter-equivalent hard and soft spheres are ka = 16.6 and 16.9, respectively. A decrease in ks leads to an increase in the multiple scattering (a more prominent CBE peak). Consequently, as in Fig. 6, the aggregation is larger than the backscatter-equivalent hard and soft spheres in (a), but this size relationship switches in (b).

Figure 4-12 shows normalized CBE peak results when the dimensionless strength of the aggregation's scatterers is $k\sigma_s^{1/2}$ = 0.38 and 3.0 for ka = 16 and ks = 3.2. In Figure 4-12a), the CBE peak is absent due to the weak multiple scattering effects stemming from a weaker dimensionless scattering strength of an individual scatterer and the radii of the backscatter equivalent hard and soft spheres (ka = 4.6 and 4.3) are smaller than that of the aggregation (ka =

16). However, in Figure 4-12b), the CBE peak is clearly present and the radii of the backscatter equivalent hard and soft spheres (*ka* = 25 and 24.8) are again larger than that of the aggregation (*ka* = 16).

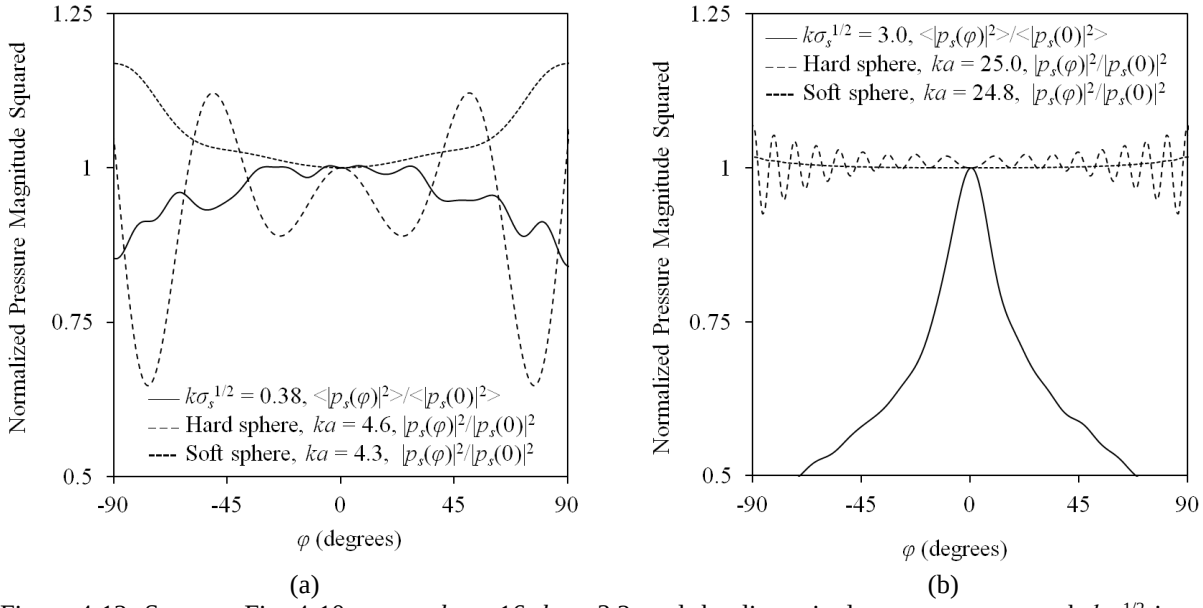

Figure 4-12: Same as Fig. 4-10, except *ka* = 16, *ks* = 3.2, and the dimensionless scatterer strength $k\sigma_s^{1/2}$ is varied between (a) and (b). In (a), $k\sigma_s^{1/2}$ is 0.38, and the radii of the backscatter-equivalent hard and soft spheres are *ka* = 4.6 and 4.3, respectively. In (b), $k\sigma_s^{1/2}$ is 3.0, and the radii of the backscatter-equivalent hard and soft spheres are *ka* = 25.0 and 24.8, respectively. An increase in the dimensionless scatterer strength yields an increase in the multiple scattering effects (a more prominent CBE peak). Here again, the aggregation is larger than the backscatter-equivalent hard and soft spheres in (a), but this size relationship switches in (b).

Calculations were also done for the baseline case and a few intermediate parametric values that fall in between the scenarios considered in Figures 4-10, 4-11 and 4-12 and show the transition of where the backscatter equivalent hard and soft spheres start to exceed that of the aggregation. For the baseline case of *ka* = 16, *ks* = 3.2 and $k\sigma_s^{1/2}$ = 1.5, the radii of the backscatter equivalent hard and soft spheres (*ka* = 15.5 and 15.5, respectively) are slightly smaller than that of the aggregation of scatterers. Increasing the aggregation size to *ka* = 25 with *ks* and $k\sigma_s^{1/2}$ held fixed at 3.2 and 1.5 respectively yielded a backscatter equivalent hard and soft sphere (*ka* = 28.6

and 28.2) larger than that of the aggregation. Holding ka = 16 and ks = 3.2 fixed and decreasing the $k\sigma_s^{1/2}$ to 0.75, the backscatter equivalent hard and soft spheres are smaller than that of the aggregation at ka = 9.1 and 8.4, respectively. Lastly, increasing the spacing to ks = 4.8, while holding ka and $k\sigma_s^{1/2}$ fixed at 16 and 1.5, respectively, resulted in a backscatter equivalent hard and soft sphere (ka = 9.9 and 9.9 respectively) to be small than that of the aggregation. Table 4-1 summarizes the findings from the matching.

Table 4- 1: Summary of the findings from the parametric study and the backscatter equivalent corresponding hard and soft sphere sizes. When multiple scattering effects are strong, the corresponding hard and soft spheres' radii exceed that of the aggregations' radii. Weaker multiple scattering effects yield backscatter equivalent spheres which are smaller in size compared to the aggregation.

ka	ks	$k\sigma_s^{1/2}$	Shape	CBE peak?	$(ka)_{hard}$	$(ka)_{soft}$
12	3.2	1.5	Sphere	Yes	10.5	10.3
16	3.2	1.5	Sphere	Yes	15.5	15.5
25	3.2	1.5	Sphere	Yes	28.6	28.2
32	3.2	1.5	Sphere	Yes	39.7	39.7
16	6.4	1.5	Sphere	Yes	6.9	6.7
16	4.8	1.5	Sphere	Yes	9.9	9.9
16	2.9	1.5	Sphere	Yes	16.6	16.9
16	3.2	0.38	Sphere	No	4.6	4.3
16	3.2	0.75	Sphere	Yes	9.1	8.4
16	3.2	3.0	Sphere	Yes	25.0	24.8
32	3.2	0.21	Sphere	No	7.0	6.8
32	3.2	0.74	Sphere	Yes	22.7	22.8
32	3.2	2.56	Sphere	Yes	52.7	52.5
32	3.2	3.2	Sphere	Yes	57.7	57.5
20.2	3.2	1.5	Prolate	Yes	20.0	19.5
20.2	3.2	1.5	Prolate	Yes	22.6	22.4
20.2	3.2	1.5	Prolate	Yes	22.6	22.3
25.4	3.2	1.5	Oblate	Yes	32.5	32.8
25.4	3.2	1.5	Oblate	Yes	27.5	27.3
25.4	3.2	1.5	Oblate	Yes	27.4	27.3

When taken together, the results shown in Figures 4-10, 4-11 and 4-12 along with the intermediate calculations indicate that as the prevalence of multiple scattering (and of CBE) increases, the CBE peak becomes more prominent; the equivalent hard and soft sphere radii increase and the relative level of scattering from the aggregation at angles φ away from the CBE

peak declines. Thus, bistatic measurements of $\left\langle |p_s(\varphi)|^2 \right\rangle$ over a sufficiently wide range of φ might be a possible remote means for discriminating between an aggregation of many small scatterers and a single large object. However, such measurements might be difficult in practice at ranges of several kilometers since the necessary angular range of φ might be several 10's of degrees. An alternative approach to aggregation vs. large object discrimination that may be applicable at short ranges is described in Chapter 6.

The second set of CBE peak strength comparisons were intended to determine the parametric dependence of $\left\langle |p_s(0)|^2 \right\rangle$ compared to that of the average backscattered pressure magnitude squared, $|p_s(0)|^2_{ideal} = \frac{1}{2}\left(|p_s(0)|^2_{hard} + |p_s(0)|^2_{soft} \right)$, from equivalent size ideal spheres with hard and soft surface boundary conditions. For this effort, the ratio, $\left\langle |p_s(0)|^2 \right\rangle \Big/ |p_s(0)|^2_{ideal}$ was plotted vs. $(ka)^{\alpha}(ks)^{\beta}(k\sigma_s^{1/2})^{\gamma}$ and the values of the scaling exponents (α, β, γ) were adjusted so that the various simulation outcomes all fell near or on a single line. The values of the scaling exponents were solely based on the simulation results and the fact that the multiple scattering effects would increase for higher $k\sigma_s^{1/2}$, lower ks and higher ka, due to the increase in the strength and number of the scatterers. Specific physical relevance of the values of (α, β, γ) have yet to be found. This comparison and fitting effort included 14 spherical aggregation parameter sets spanning the parametric ranges $12 \le ka \le 32$, $6.4 \ge ks \ge 2.9$, and $0.21 \le k\sigma_s^{1/2} \le 3.2$; and the six spheroidal aggregation parameter sets described for Figures 4-7 and 4-8 where the volume equivalent radius was used for a.

The results of this comparison and fitting effort are shown on Figure 4-13 where $\left\langle |p_s(0)|^2 \right\rangle \Big/ |p_s(0)|^2_{ideal}$ is plotted vs. $(ka)^{1/3}(ks)^{-1}(k\sigma_s^{1/2})^{1/2}$, and circles and squares represent

spherical and spheroidal parameter sets, respectively. This figure provides three important results. First, as expected, the fitted exponent values suggest that the relative height of a CBE peak increases when the aggregation is larger, when the scatterers are closer together and when the strength of each scatterer is larger. Second, when $\left\langle |p_s(0)|^2 \right\rangle \Big/ |p_s(0)|^2_{ideal}$ is above unity or equivalently when $(ka)^{1/3}(ks)^{-1}(k\sigma_s^{1/2})^{1/2} \geq 0.94$, the aggregation backscatters more sound than a single ideal spherical scatterer that is the same size as the aggregation. Thus, under the right conditions, a school of fish may appear as a single man-made object of the same or larger size when interrogated via a backscatter based sonar system. And third, the filled symbols in Figure 4-13 indicate parameter sets where no discernible CBE peak was found. These parameter sets appear in the lower left of Figure 4-13 and occur when $(ka)^{1/3}(ks)^{-1}(k\sigma_s^{1/2})^{1/2}$ is less than 0.48.

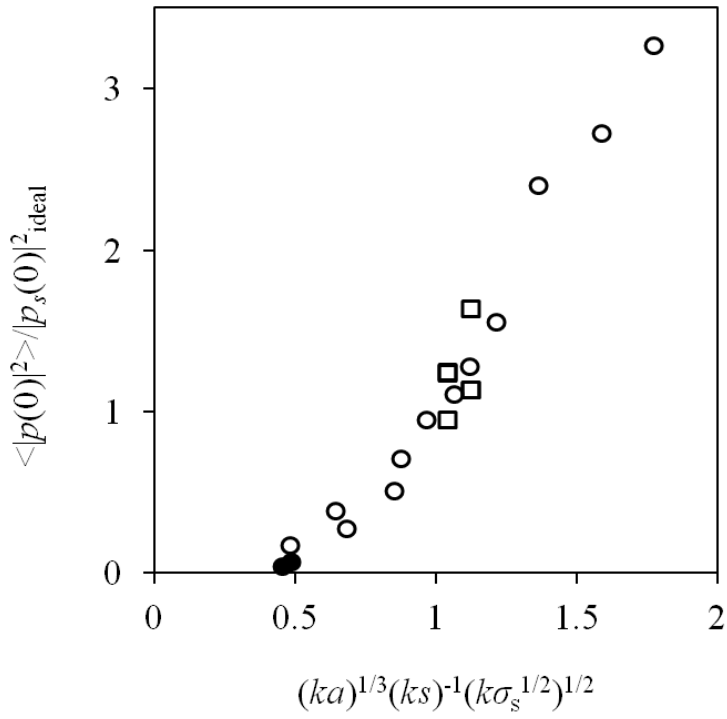

Figure 4-13: Backscattering ratio $\left\langle |p_s(0)|^2 \right\rangle / |p_s(0)|^2_{ideal}$ vs. $(ka)^{1/3}(ks)^{-1}(k\sigma_s^{1/2})^{1/2}$ for 20 different parameter sets involving spherical aggregations (circles) and spheroidal aggregations (squares). The filled symbols indicate parameter sets where no discernible CBE peak was found. The scattered field from an aggregation of point scatterers is greater than that of equivalent sized ideal spheres when $(ka)^{1/3}(ks)^{-1}(k\sigma_s^{1/2})^{1/2} \geq 0.94$.

An alternate summary of the results shown in Figure 4-13 is provided in Figure 4-14 where the difference between the average size of the ideal spheres, $(ka)_{ref} = [(ka)_{hard} + (ka)_{soft}]/2$, and the size of the aggregation (ka) is plotted vs. a product of powers of independent dimensionless parameters, $(ka)^{1/2}(ks)^{-4/5}(k\sigma_s^{1/2})^{3/4}$. For this summary, the backscattered mean square pressure from the aggregation of scatterers is matched with the pressure magnitude squared from the ideal hard and soft sphere. The corresponding backscatter equivalent hard and soft spheres' radii are then averaged and the difference of the average sphere from the aggregation is obtained. Here, again, the empirical scaling exponents (1/2, –4/5, 3/4) were chosen so that the various simulation outcomes all fell on or near a single line. As in Figure 4-13, the circles and squares in Fig. 4-14 represent spherical and spheroidal parameters, respectively,

and the two filled symbols are for parameter sets that did not produce discernible CBE peaks. Additionally, in Figure 4-14, the positive values of $(ka)_{ref} - (ka)$ indicate where the backscatter equivalent ideal sphere is larger than the aggregation, and the negative values show where the backscatter equivalent ideal sphere is smaller than the aggregation .

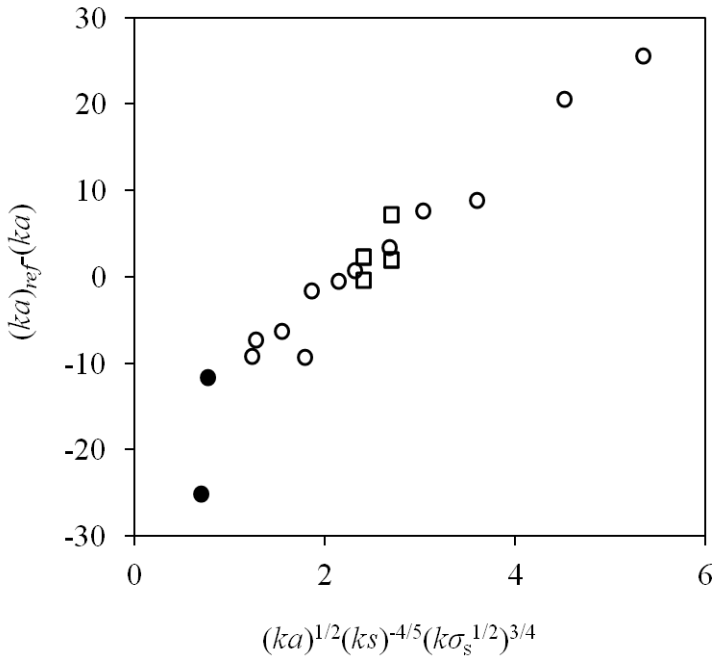

Figure 4-14: Difference between the reference radius, the average in the radii of the hard and soft spheres, and the aggregation radius, $(ka)_{ref} - (ka)$ vs. an empirical product of powers of the dimensionless parameters, $(ka)^{1/2}(ks)^{-4/5}(k\sigma_s^{1/2})^{3/4}$, for 20 parameter sets involving spherical aggregations (circles) and spheroidal aggregations (squares). The two filled symbols indicate parameter sets where no discernible CBE peak was found, $(ka)^{1/2}(ks)^{-4/5}(k\sigma_s^{1/2})^{3/4} < 0.8$. The aggregation radius is smaller than that of the reference sphere when $(ka)^{1/2}(ks)^{-4/5}(k\sigma_s^{1/2})^{3/4} \geq 2.3$. Thus, when strong enough, multiple scattering may cause an aggregation to appear to be a single larger object.

Figure 4-14 provides three important results. First, as in Figure 4-13, the exponent values indicate that the CBE peak strength increases when the aggregation, or its projected area normal to the incident wave vector, is larger, when the scatterers are closer together, and when the strength of each scatterer is larger. Second, when $(ka)_{ref} - (ka)$ is greater than 0, or equivalently when $(ka)^{1/2}(ks)^{-4/5}(k\sigma_s^{1/2})^{3/4} \geq 2.3$, the aggregation backscatters as much sound as a perfectly reflecting sphere of equal or larger size. Thus, under the right conditions, a school of fish may

appear to be single man-made object of the same or larger size when remotely interrogated via a backscatter-based sonar system. And third, the location of the filled symbols suggests that CBE is not apparent in the far-field of the aggregation when $(ka)^{1/2}(ks)^{-4/5}(k\sigma_s^{1/2})^{3/4} \leq 0.8$.

The second backscattering strength comparison involves determining the extent to which the effective medium approximation can be used to determine the amplitude of the average backscattered pressure, $|<p_s(0)>|$, from aggregations of scatterers. These results are shown in Fig. 4-15 where $20\log_{10}(|<p_s(0)>|/|p_s(0)|_{Hahn})$ is plotted vs. $|4\pi(kg_1)^2/(ks)^3|$, the wave number scaled form of the small parameter described in Hahn (2007) from (2-19), where $|p_s(0)|_{Hahn}$ is the amplitude of the pressure backscattered from a single sphere with the same radius as the aggregation that has the effective medium characteristics of the aggregation. Backscattered pressure amplitudes from the aggregations vary significantly, and this variation is quantified by the error-bars shown in the Fig. 4-15 which corresponds to plus and minus one standard deviation of the mean.

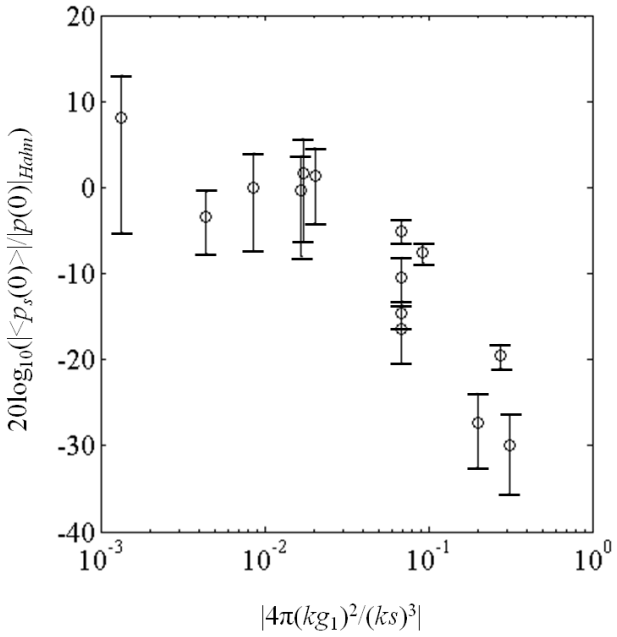

Figure 4-15: Average backscattered field ratio in dB, $20\log_{10}\left(\left|\langle p_s(0)\rangle\right|/\left|p(0)\right|_{Hahn}\right)$ vs. $\left|4\pi(kg_1)^2/(ks)^3\right|$, for 14 parameter sets representing spherical aggregations. Here $|p(0)|_{Hahn}$ is the backscattered amplitude from an equal size sphere having properties predicted by Foldy's effective medium theory for the aggregation (Foldy 1945, Hahn 2007). The error bars represent plus and minus one standard-deviation of the mean. The variations in error bar size are due to the differences in the number of realizations considered for each parameter set. For $\left|4\pi(kg_1)^2/(ks)^3\right| \leq$ 0.03, the average backscattered pressure from the aggregation matches the Hahn sphere predictions within the known statistical uncertainty. However, as $\left|4\pi(kg_1)^2/(ks)^3\right|$ increases above 0.06, backscatter from the Hahn (2007) sphere overestimates the average-field amplitude from the aggregation because the effective medium theory is only valid when $\left|4\pi(kg_1)^2/(ks)^3\right| << 1$ (Frisch 1968, see also Hahn 2007).

Figure 4-15 provides two noteworthy results. First, the current average field backscatter results for spherical aggregations match those from the effective medium approximation, to within the known statistical uncertainty, when $|4\pi(kg_1)^2/(ks)^3|$ is small, as expected from the dimensional and scattering-diagram analysis of Frisch (1968) who concluded that $|4\pi(kg_1)^2/(ks)^3|$ must be small for the effective medium approximation to be valid. And second, the effective medium approximation is likely to overestimate the average backscattered field amplitude when $|4\pi(kg_1)^2/(ks)^3|$ is not small. This overestimate occurs because the Foldy (1945) effective medium approximation excludes some multiple-scattering chains (Frisch 1968), which leads to an

underestimate (overestimate) of random (ensemble-average) scattering within and from the aggregation. Consequently, $|<p_s(0)>|/|p_s(0)|_{Hahn}$ falls below unity as $|4\pi(kg_1)^2/(ks)^3|$ increases.

4-6: Summary and Conclusions

In this chapter, the Foldy (1945) multiple scattering equations were considered to simulate acoustic CBE in the far field of a finite size aggregation of scatterers illuminated by a plane wave with wave number k in an unbounded uniform environment. The simulations involved thousands of realizations for each aggregation parameter set and included variations in the dimensionless aggregation size: $12 \leq ka \leq 32$, in the dimensionless average scatterer spacing: $6.4 \geq ks \geq 2.9$, in the dimensionless strength of a scatterer: $0.38 \leq k\sigma_s^{1/2} \leq 3.0$, and in the shape of the aggregation (spherical, oblate spheroidal, prolate spheroidal). From these simulations, the dependence of the width and height of the CBE peak on ka, ks, $k\sigma_s^{1/2}$, and the aggregation's shape was determined. Simulated backscattered mean square pressures from the spherical aggregations were also compared to that from single ideal spherical scatterers.

The results from this chapter support the following three conclusions. First, the aggregation geometry sets the width of the CBE peak in the far field, when a CBE peak exists. Larger aggregations produce narrower peaks, whereas smaller aggregations produce wider peaks. Overall, CBE peak widths were found to be proportional to $1/ka$ for spherical aggregations, and, for all aggregations, CBE peak widths were consistent with diffraction limited radiation from the aggregation when each scatterer is replaced by a monopole source and all the source phases are set to produce a retro-directed plane wave. Second, the mean square pressure backscattered from a spherical aggregation may exceed that from a single equivalent size sphere having an ideal hard or pressure release surface boundary condition. The likelihood of this occurring increases

when the aggregation is larger, the scatterers are closer together, and the strength of an individual scatterer is larger. When considered all together, the composite requirement for an aggregation to produce equivalent or stronger backscattering than an equivalent-volume ideal sphere is $(ka)^{1/2}(ks)^{-4/5}(k\sigma_s^{1/2})^{3/4} \geq 2.3$. Third, Foldy's effective medium theory matches the simulation results to within the known statistical uncertainty when applied to the amplitude of the average field backscattered from an aggregation and equivalent size spheres with matched properties when $|4\pi(kg_1)^2/(ks)^3| < 0.03$.

The findings in this chapter show CBE in a context more applicable to the interests of the U.S. Navy and fisheries acoustics groups. While CBE is observed in the far field and there are noticeable differences in the average backscattering from an aggregation of scatterers compared to that of a single ideal sphere, there are disadvantages which likely render the use of CBE for remote aggregation-vs.-single-object discrimination impractical. Here, it is assumed that the school of fish can be interrogated by many pings, the swimbladder of the fish can be approximated as an omnidirectional point scatterer ($ka_s << 1$) and the geometry would, for the most part, stay the same over the realizations. Additionally, in order to see a noticeable difference in the backscatter direction from other angles, returns would need to be measured over a wide range of angles, on the order of 10's of degrees. Lastly, the fish composing the school need to be strong scatterers, spaced close together and the aggregation needs to be large enough to observe CBE. Thus, for sonar operations based on identifying the existence of CBE, a fish school consisting of weak scatterers may yield a false classification. In practice, however, the results shown in this chapter provide insight into the differences in the returns between a school of fish from that of a single scattering object, such as a bubble or manmade scattering object, under idealized circumstances (without fluid-structure interactions) in the free space. Chapter 5

will consider broadband CBE to see if there are any changes in returns when the incident signal is a broadband pulse. Additionally, it will present results that explore whether or not a time domain signal would produce equivalent results with fewer realizations or if other features in the returned signal can be considered for aggregation-vs.-single-object discrimination.

CHAPTER 5

Far Field Broadband Coherent Backscatter Enhancement

While the work considered in Chapter 4 started to address some of the concerns of interest to the U.S. Navy by considering narrowband, far field simulations in the frequency domain, this chapter presents work considering broadband pulses using frequency sweeps with ranges of interest to the Navy in the time domain (Nero 1996). The first half of this chapter focuses on aggregations of omnidirectional point scatterers with fixed scattering strength and is a parametric study considering the impact on the CBE peak for an increase in the number of scatterers and fixed scattering cross section in the time domain. The second half of this chapter involves: (i) simulating aggregations of scatterers with herring fish properties, particularly the effective swimbladder radius and fish flesh viscosity, at varying depths in the ocean and (ii) the impact that varying aggregation depth has on the CBE peak. Comparisons of the simulated results from the aggregations are made with the ideal hard and soft spheres as in Chapter 4 to show the differences in the returns from a school of herring, a fish species common in the pelagic zone of the ocean (Costello et al., 2010), with single isolated idealized scattering objects that also may be present in the ocean. Changes to the incident pulse after interacting with the aggregation of scatterers are also considered. Due to the complexity of the broadband simulations, most of the simulations considered here are not fully converged, but are sufficiently so to observe the CBE peak.

5-1: Simulation Setup

In this chapter, the simulation geometry is the same as in Figure 4-2 with a spherical aggregation centered at the origin and the receiving ring radius of R = 5000m. Thus, in water (c = 1500m/s), the time delay of the scattered field should be at 3.33s. For these simulations, the aggregation has a radius, a, of 2.5m and the scatterers have fixed scattering cross section (σ_s = 0.03 m^2). The simulated school of herring has a radius of, a, of 2.85m. The fixed scattering cross section aggregations consisted of 1000 and 2000 scatterers, and the simulated herring school consisted of 1000 fish. For the herring fish school, the average spacing s was a typical fish length (s = 0.46m herring). The swim bladder volume was 1.45 ml (Fässler et al. 2008) with a swimbladder radius of a_s = 7.02mm and a viscosity coefficient approximating fish flesh is ξ = 20 Pas (Love 1978). A 0.1s frequency sweep pulse is considered from f_0 to f_1, though simulations are performed for frequencies from f_0 - 100 to f_1 + 100 to cover the effects of spectral leakage in the Fourier transform of the signal as well, and a sampling frequency of 10kHz is considered.

For the fixed scattering strength simulations, the frequencies considered range from f_0= 3kHz to f_1 = 4kHz. For the simulated herring schools, the swim bladder radius and viscosity coefficient values have been used in the Love (1978) model discussed in Chapter 2 and the frequencies of interest have surrounded the resonance peak of the swim bladder radius for the three depths (shown in Figure 5-1 as $k\sigma_s^{1/2}$ vs. frequency in kHz). Thus, for a depth of z = 60m, f_0 = 1kHz and f_1 = 2kHz (ka_s = 0.03-0.06); z = 236m, f_0 = 1.5kHz and f_1 = 3kHz (ka_s = 0.04-0.09); and for a depth of z = 430m, f_0 = 2.5kHz and f_1 = 4kHz (ka_s = 0.07-0.12). For the frequency ranges considered, the effective wave number scaled swimbladder radius is significantly less than 1. Thus, the Foldy (1945) equations are directly applicable herring schools at these depths

and frequencies. At the three depths, the maximum dimensionless scattering strengths are $k\sigma_s^{1/2}$ = 0.9 at a frequency of 1.25kHz at z = 60m, $k\sigma_s^{1/2}$ = 1.9 at a frequency of 2.33kHz at z = 236m, and $k\sigma_s^{1/2}$ = 2.4 at a frequency of 3.1kHz at z = 430m. These depths are all in the pelagic zone in the ocean (Costello et al, 2010).

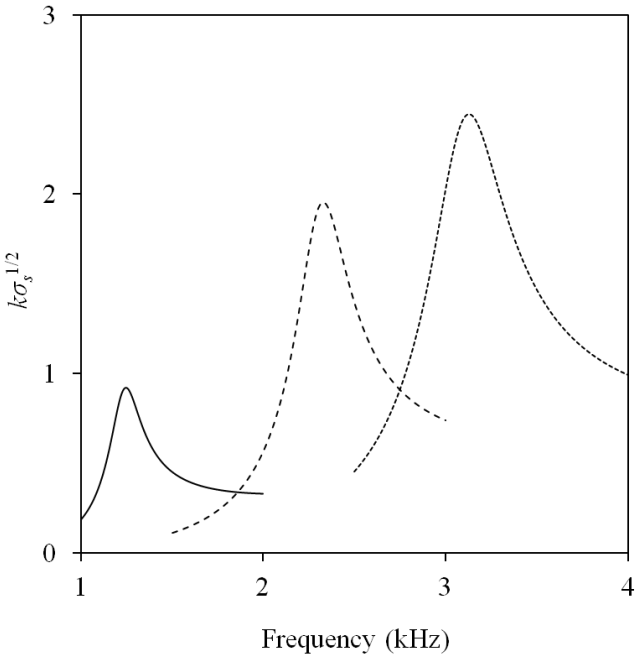

Figure 5-1: Effect of the dimensionless scattering strength of each scatterer $k\sigma_s^{1/2}$ as a function of frequency (kHz) for varying depths z = 60m (——), 236m (– – – –) and 430m (----) via the Love (1978) model. Each curve covers the bandwidth of the simulations at that depth.

The ideal hard and soft spheres are evaluated using van Bladel's (1968) scattering formulae at the same frequencies as the simulations. Unlike in Chapter 4, where the simulations are matched to the corresponding sphere using the backscatter direction to set the sphere's radius, in this chapter, due to the complexity of the simulations, the corresponding van Bladel (1968) hard and soft spheres are obtained by matching the radii of the aggregation: $a = a_{hard} = a_{soft}$.

5-2: Simulation Results with Fixed Scattering Cross Section and Comparisons with the Incident Signal

In Chapters 3 and 4, single frequencies with fixed average scatterer spacing *ks* and dimensionless scattering strength, $k\sigma_s^{1/2}$, were considered. Here, the dimensionless scattering strength could be any value as long as $k\sigma_s^{1/2}$ was less than or equal to 3.5449. Therefore, for the broadband simulations, since the wave number would be constantly changing as the frequencies change, the scattering cross section is held fixed at $\sigma_s = 0.03\text{m}^2$, which for a 3-4kHz frequency sweep, yields a dimensionless scattering strength ($k\sigma_s^{1/2}$ = 2.2-2.9) well under the point scatterer constraint but still representing strong scatterers.

Figures 5-2 and 5-3 show the change in prominence of the CBE peak for 1000 and 2000 scatterer aggregations after 64 realizations. For these figures, the ordinate is the azimuthal angle, φ, from Fig. 4-2, in degrees and the time delay on the abscissa is in seconds. As in Chapter 4, the angular range of interest spans from φ = (–90°, +90°). The colors represent the scattered mean square pressure in the time domain. A comparison of these two figures, which have different color scales, indicates that, similarly to the far field single frequency simulations, the back-scattered mean square pressure in the time domain increases as the multiple scattering effects increase (an increase in the number of scatterers causes a decrease in the average spacing between scatterers, and this increases the amount of multiple scattering). Additionally, since it was seen in Chapter 4 that the CBE peak width is dictated by aggregation geometry and the same frequency ranges are considered for these simulations, the peak width in Figures 5-2 and 5-3 are expected to be the same. Though the results at some times are off center due to incomplete convergence, generally, the peak widths do seem to follow this expected trend.

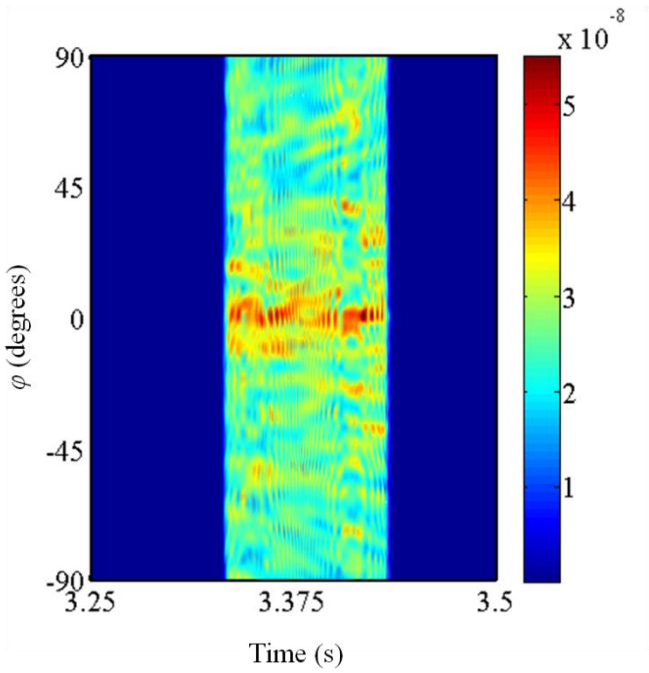

Figure 5-2: Scattered mean square pressure in the time domain for 1000 scatterers (ks = 5.1-6.7) in a spherical aggregation with radius = 2.5m, a dimensionless scattering strength each scatterer of $k\sigma_s^{1/2}$ = 2.2-2.9, and a 3-4kHz frequency pulse. Since the range of the dimensionless scattering strength is high for this simulation, a peak still occurs at $\varphi = 0$.

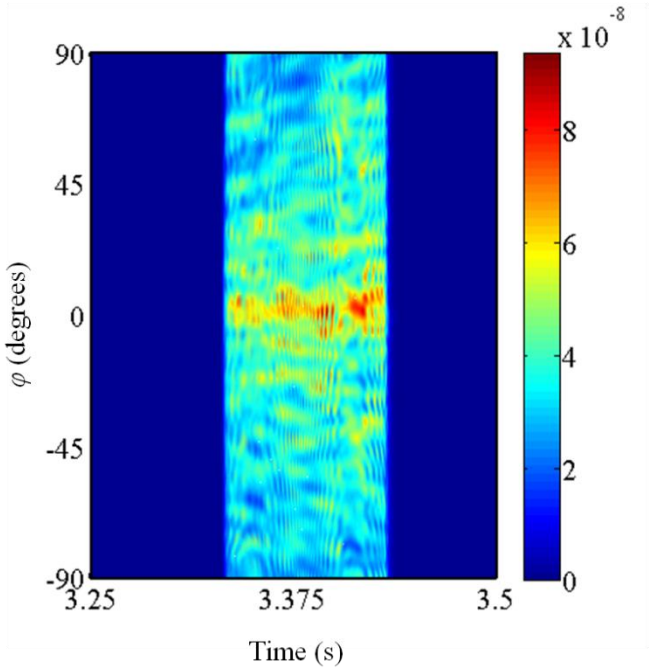

Figure 5-3: Same as Fig. 5-2 except here there are 2000 scatterers (ks = 4.0-5.3).

Figures 5-4 has three plots. The incident original signal is the uppermost plot. The original signal squared is the middle plot. The resulting signal after it interacts with the scattering aggregation is the third plot. Figure 5-4 (the two plots in the top) shows the original 0.1s-duration 3-4kHz frequency sweep and (the third plot) is the scattered mean square pressure in the time domain in the backscatter direction for 1000 scatterers (shown in blue) and 2000 scatterers (shown in black). If these simulations were fully converged, it would be that the mean square pressure in the backscatter direction would be smooth without the oscillations (see Section 5-3 for more converged results). The resulting backscattered mean square pressure signal after it interacts with the aggregation of scatterers is higher for the 2000 scatterer simulations than it is for the 1000 scatterer simulations, as expected.

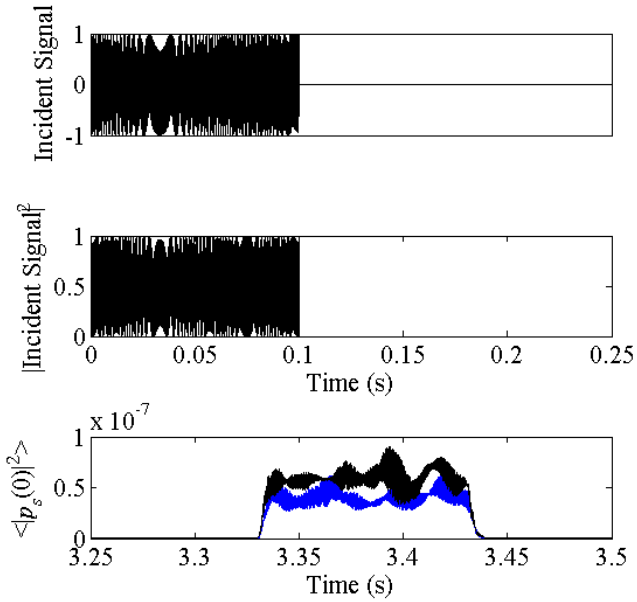

Figure 5-4: Backscattered mean square pressure for 1000 (blue) and 2000 (black) scatterers (bottom) corresponding to the original signal (top two plots)

The correlation of the original signal with the backscattered pressure signal even further, the correlation coefficient of the two signals is considered for a single realization. Here, the real part of the backscattered pressure is considered. In both Figures 5-5 and 5-6, the correlation coefficient of the real part of the backscattered pressure with the original signal is plotted as a function of the time lag in seconds. The real part of the backscattered mean pressure is very poorly correlated with the original signal for both 1000 and 2000 scatterers.

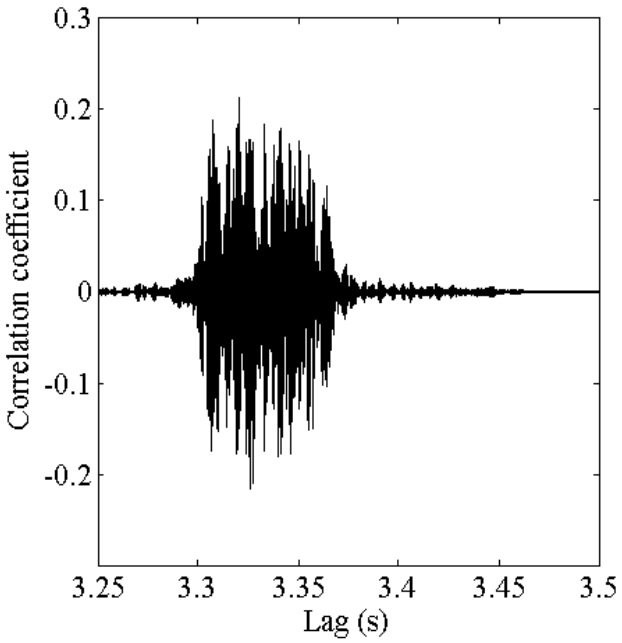

Figure 5-5: The correlation coefficient of the real part of the pressure of a single realization of 1000 scatterers is very poorly correlated with the original signal.

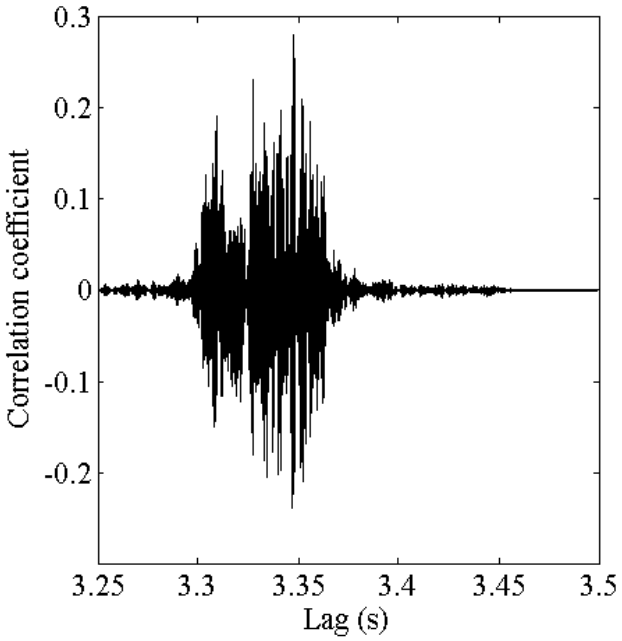

Figure 5-6: The correlation coefficient of the real part of the pressure of a single realization of 2000 scatterers is very poorly correlated.

Based on Figures 5-2 to 5-6, the following three important observations are made. They are: (*i*) in as few as 64 realizations, a CBE peak does start to emerge, though there are still some higher mean square pressure values at other angles. This is shown in Figures 5-2 and 5-3. (*ii*) Secondly, it also shows that as in the frequency domain considered in Chapter 4, an increase in the multiple scattering effects does yield an increase in the mean square pressure in the time domain. (*iii*) When the real part of the backscattered pressure is considered, the cross correlation of the two signals yields results which are very poorly correlated, because of the random placement of the scatterers.

5-3: Resonant Scattering CBE and Comparisons with van Bladel (1968) Spheres

Thus far, the effects of an aggregation of idealized scatterers on the original signal have been studied using as many as 64 realizations and as few as a single realization. The work in this

section considers resonant point scatterers with herring fish properties. Furthermore, it addresses relevant questions to practical sonar applications by considering the van Bladel (1968) spheres from Chapters 2 and 4. Given that the ocean environment can only be considered a free space environment over short ranges, these simulations may be relevant for downward looking echosounder recordings where direct path propagation is solely considered (no surface or bottom reflections).

For the simulations in this section, 4096-4900 realizations were conducted for the three depths. Thus, the results appear smoother and cleaner compared to that shown in Section 5-2. It should be noted, however, these simulations took close to 8-10 months on the supercomputing cluster, Flux, provided by the University of Michigan's Advanced Research Computing facility, unlike the 4-6 week runtime on the same computer(s) for the single frequency signals. As in the previous section and Chapter 4, this study was performed as a parametric study, analyzing the effect of the depth on the CBE peak. From Figure 5-1, the increase in the depth causes the dimensionless scattering strength to increase so it would be expected that the peak should be more prominent. Additionally, a brighter band, representing stronger scattering, would be expected, corresponding to the time when the resonant frequency occurs (3.36s for the herring school at 60m depth, 3.39s for the herring school at 236m depth and 3.37s for the herring school at 430m depth).

Figure 5-7 shows the resulting scattered mean square pressure in the time domain for a school depth of 60m. A CBE peak does appear for this aggregation at the depth considered, though it is weak, as will be demonstrated for higher depths such 236m and 430m. Additionally, since a lower band of frequencies are considered (1-2kHz), the wave number scaled size of the aggregation is small (ka = 14.9 at the resonance frequency). Therefore, the CBE peak has a width

of $\Delta\varphi = 2\pi/ka = 24.2°$, which is consistent with that expected from the single frequency signal results shown in Chapter 4. Additionally, as expected, the highest mean square pressure occurs at the time corresponding to the resonant frequency, as is seen in Figure 5-7 (dark red). The regions surrounding that time corresponding to the resonant frequency (orange-yellow) are still bright, but gradually dim with increasing or decreasing time. Figure 5-8 shows the backscattered mean square pressure as a function of time for the herring fish school at 60m corresponding to the original signal (top two plots). The backscattered mean square pressure tends to follow a similar trend as the dimensionless scattering strength as a function of frequency in Figure 5-1 since the frequency-sweep broadcast signal allows an approximate correspondence to be drawn between frequency and time.

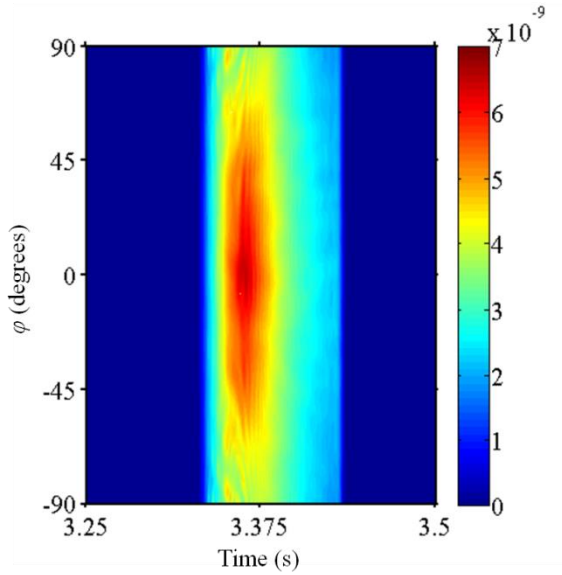

Figure 5-7: Mean square pressure as a function of φ (degrees) and time (s) for the herring fish school at a depth of 60m. A CBE peak does result at the time corresponding to the resonant frequency and the peak is very broad.

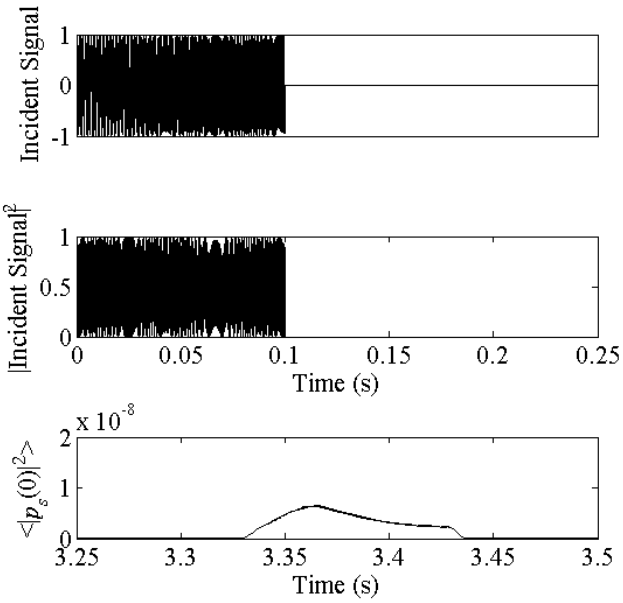

Figure 5-8: Backscattered mean square pressure as a function of time for the herring fish school at 60m corresponding to the original signal (top two plots)

The comparisons with the van Bladel (1968) spheres of equivalent size show that the angular dependence of the pressure magnitude squared for the hard and soft spheres are similar, though there are small differences in magnitude between the hard and soft spheres (Figures 5-9 and 5-10). Figures 5-9 through 5-11 show that the scattering from the equivalent size hard and soft sphere is much greater than that from the aggregation. This is contrary to what has been observed for the case of single frequency scaling developed in Chapter 4. Additionally, Figure 5-11 shows the comparison of the pressure magnitude squared from the soft and hard spheres with the mean square pressure of the herring school at 60m depth. The top two figures in Figure 5-11 show the backscattered pressure magnitude squared of the soft and hard spheres, respectively, and the bottom plot is the backscattered mean square pressure over the 4096 realizations for the herring fish school at 60m depth. The returns for the aggregation are significantly different from that of the hard and soft sphere. The pressure is much lower and the

returned signal ramps up gradually from 3.33 to 3.37s compared to the soft and hard sphere. The later part of the signal also ramps down later (3.43s) compared to that of the hard and soft sphere. This is due to the resonance curve shown in Figure 5-1 for 60m depth.

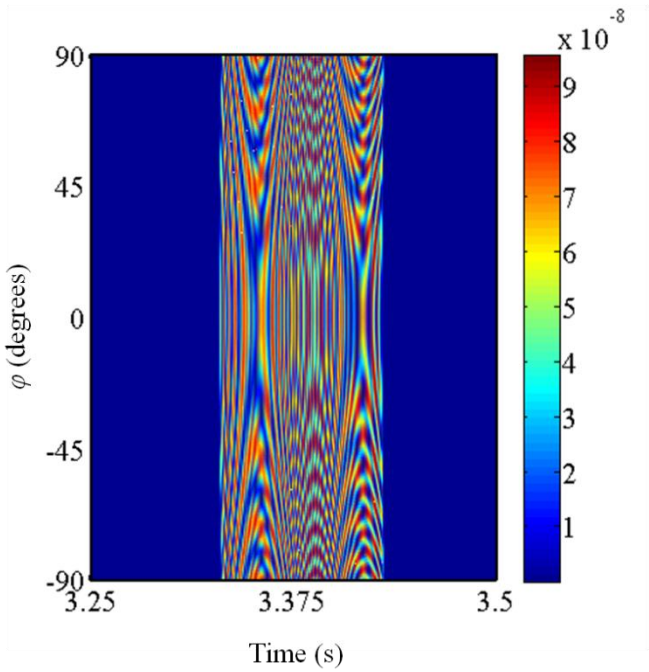

Figure 5-9: Pressure magnitude square as a function of angle (φ) in degrees and time in seconds for a soft sphere with frequencies 1-2kHz, corresponding to the frequency range considered for the herring fish school at 60m depth

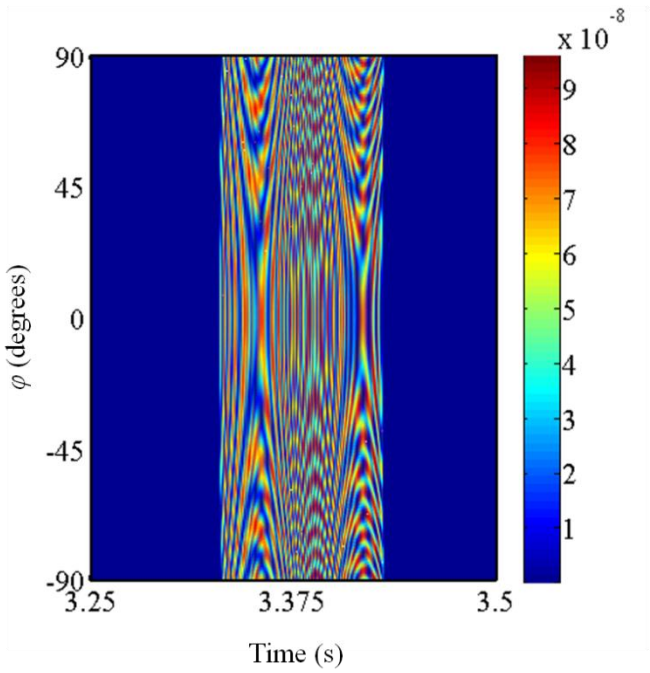

Figure 5-10: Pressure magnitude square as a function of angle (φ) in degrees and time in seconds for a hard sphere with frequencies 1-2kHz, corresponding to the frequency range considered for the herring fish school at 60m depth

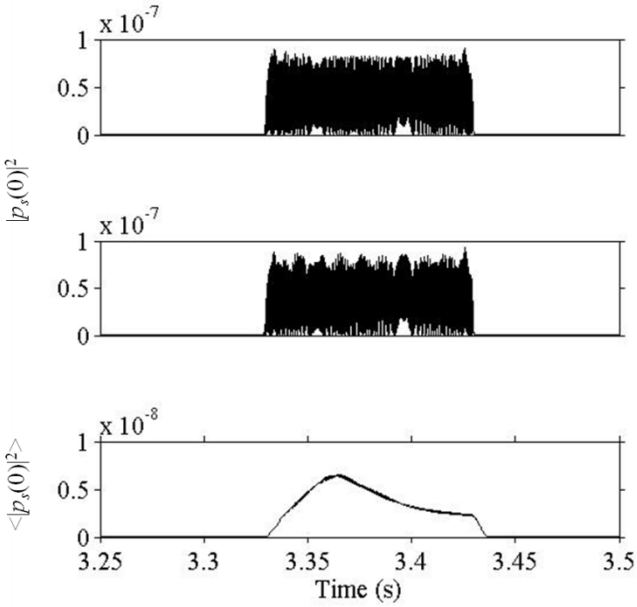

Figure 5-11: Pressure magnitude squared for the soft (top) and hard (middle) spheres and the spherical aggregation of herring fish at 60m depth (bottom)

Figure 5-12 shows the resulting plot of the mean square pressure as a function of the angle, φ, and time in seconds for the herring school at 236m for 1.5-3kHz. Here, again a CBE peak does occur, which is more prominent and the scattered mean square pressure for the aggregation at this depth is larger, due to the fact that the dimensionless scattering strength at this depth is also larger with a dimensionless scattering strength of 1.93 at the resonant frequency. The highest mean-square pressure in this figure occurs at 3.39s. The angular width of this peak is narrower compared to Figure 5-7 since the aggregation radius at resonance is ka = 27.8, yielding a peak width of $2\pi/ka$ = 12.9 degrees. Figure 5-13 is the backscattered mean square pressure as a function of time for the herring fish school at 236m corresponding to the original signal (top two plots). As in Figure 5-8, this figure also shows that the shape of the time dependent signal follows that of Figure 5-1 with the peak at 3.39 s, corresponding to the resonant frequency because of the time-frequency correspondence inherent in a frequency-sweep signal.

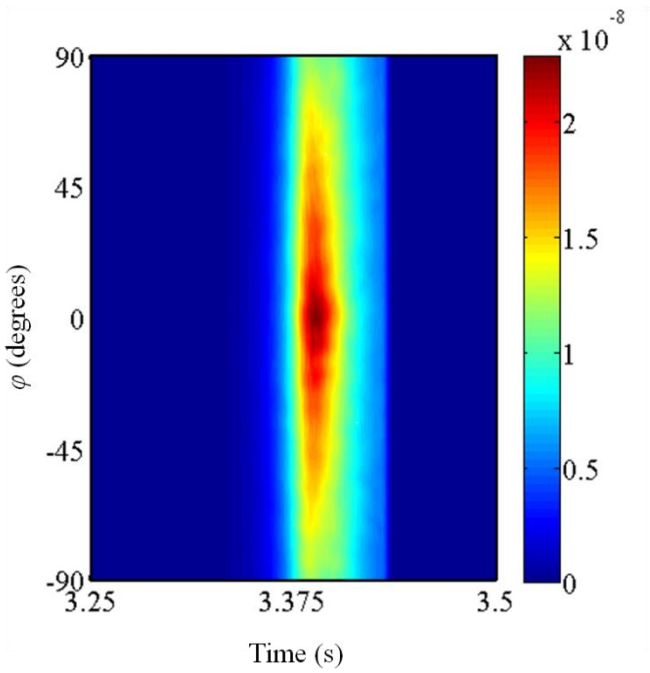

Figure 5-12: Mean square pressure as a function of φ (degrees) and time (s) for the herring fish school at a depth of 236m. A CBE peak does result at the time corresponding to the resonant frequency.

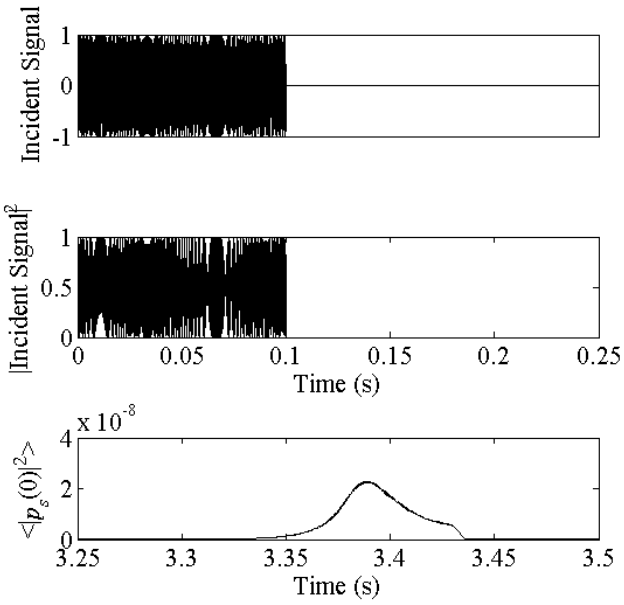

Figure 5-13: Backscattered mean square pressure as a function of time for the herring fish school at 236m corresponding to the original signal (top two plots)

Comparing these findings with the van Bladel (1968) spheres, the corresponding soft and hard spheres of the same size for this frequency band and the angular dependence, yields results (Figures 5-14 and 5-15) which look similar but different in magnitude, just as in Figures 5-9 and 5-10. Comparing the time dependence of the pressure magnitude square of the soft and hard spheres (top and middle) with the aggregation (bottom), the mean square pressure of the aggregation ramps up gradually from 3.33-3.38s (Figure 5-16). It is also longer (3.43s) than the pressure magnitude squared of the soft and hard sphere.

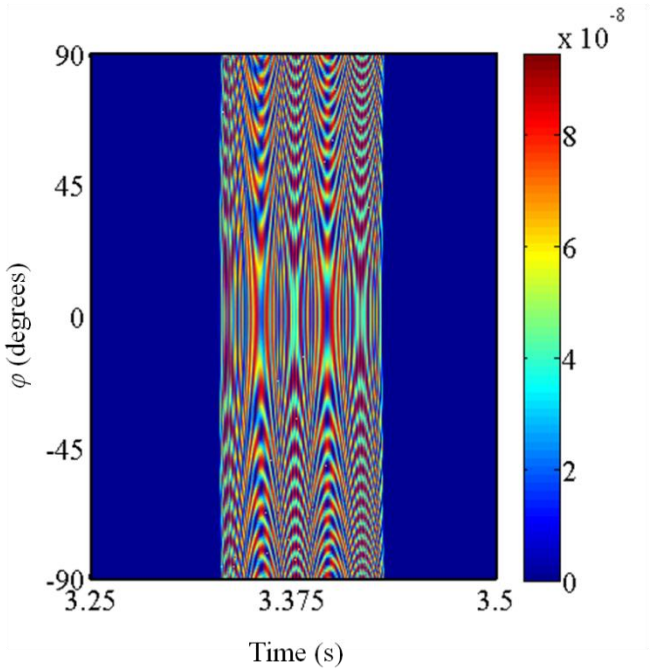

Figure 5-14: Pressure magnitude square as a function of angle (φ) in degrees and time in seconds for a soft sphere with frequencies 1.5-3kHz, corresponding to the frequency range considered for the herring fish school at 236m depth

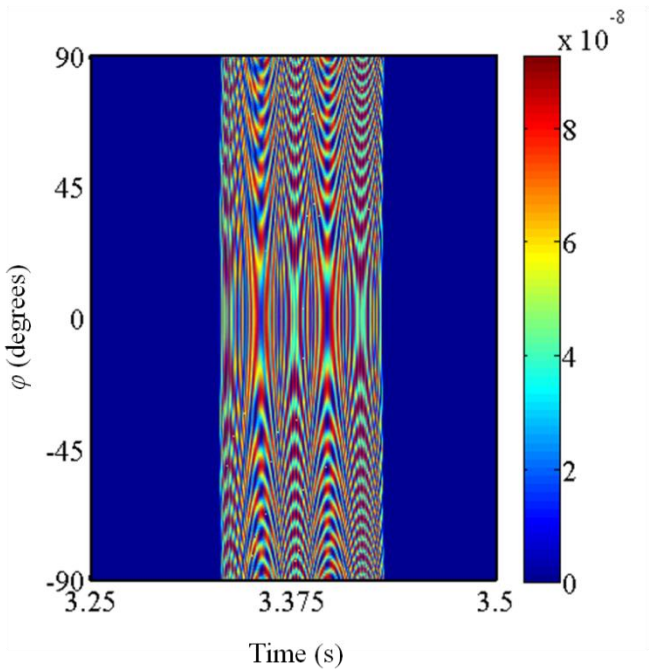

Figure 5-15: Pressure magnitude square as a function of angle (φ) in degrees and time in seconds for a hard sphere with frequencies 1.5-3kHz, corresponding to the frequency range considered for the herring fish school at 236m depth

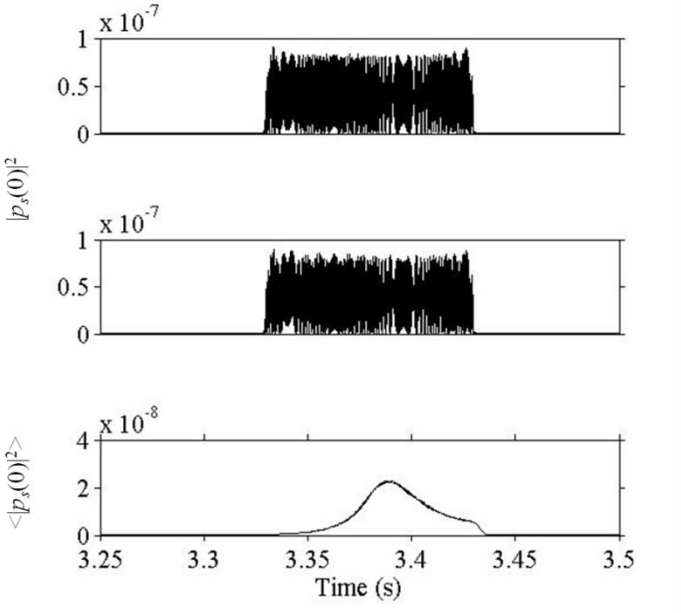

Figure 5-16: Pressure magnitude squared for the soft (top) and hard (middle) spheres and the spherical aggregation of herring fish at 236m depth (bottom)

The deepest fish school considered was at a depth of 430m. Here, the herring's swim bladder resonant frequency was 3.1kHz and the dimensionless scattering strength at that frequency was 2.4. Figure 5-17 shows the mean square pressure as a function of angle in degrees and time (s). A more prominent CBE peak occurs at this depth and the peak width appears to have narrowed significantly since the aggregation radius at the resonant frequency is ka = 37, yielding a peak width of $2\pi/ka$ = 9.7 degrees. Figure 5-18 shows the resulting time dependent mean square pressure for this depth for frequencies of 3-4kHz. Here, the shape is similar to that of the resonant frequency and the peak is more distinct, compared to the other plots.

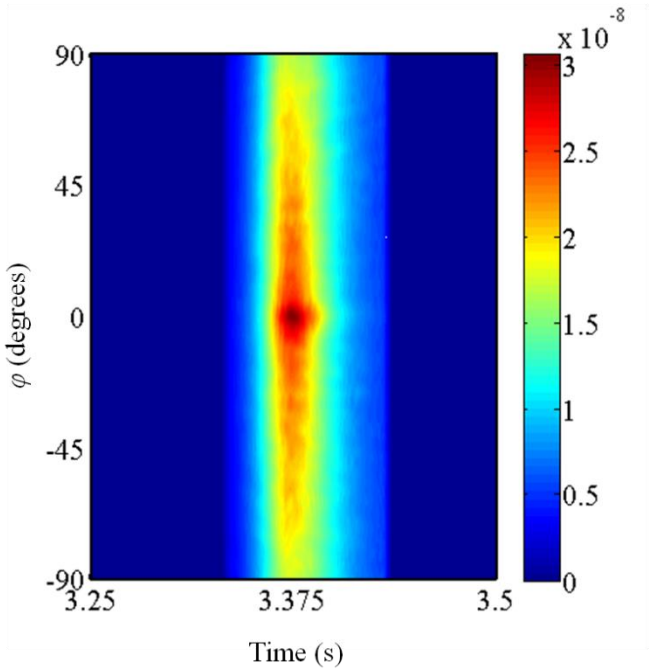

Figure 5-17: Mean square pressure as a function of φ (degrees) and time (s) for the herring fish school at a depth of 430m. A CBE peak does result at the time corresponding to the resonant frequency.

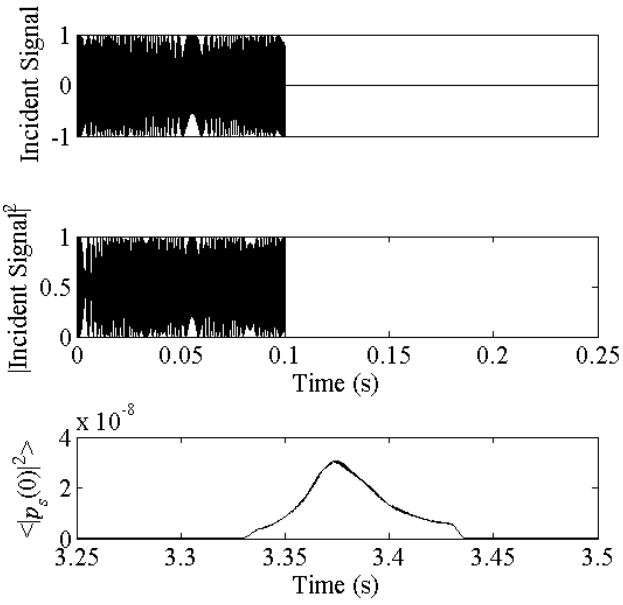

Figure 5-18: Backscattered mean square pressure as a function of time for the herring fish school at 430m corresponding to the original signal (top two plots)

Considering the van Bladel (1968) spheres for the frequencies of 3-4kHz, Figures 5-19 and 5-20 show the pressure magnitude squared as a function of angle and time in seconds for the soft and hard spheres, respectively. As in the previous depths, the pressure magnitude squared of the soft and hard spheres look similar, with slight differences in magnitude. Figure 5-21 shows the time dependence of the backscattered pressure magnitude squared for the soft and hard spheres (top and middle, respectively) and the backscattered mean square pressure of the herring fish school at 430m depth. Once again, there are significant differences in the pressure magnitude squared of the soft and hard spheres from the mean square pressure of the herring fish school at 430m depth of the same size. The signal is smoother and more gradual, both early on (3.33s) and later on (3.43s), yielding in the pressure signal once again ramping down later than that of a soft or hard sphere of the same size.

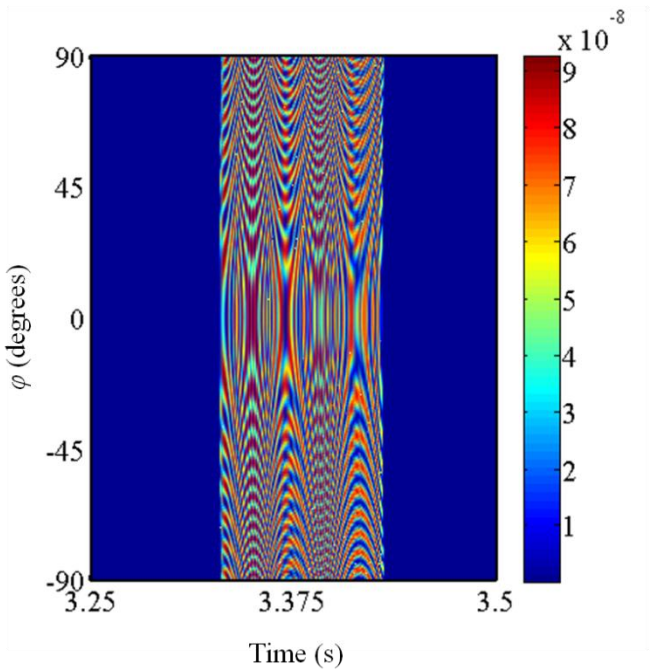

Figure 5-19: Pressure magnitude square as a function of angle (φ) in degrees and time in seconds for a soft sphere with frequencies 3-4kHz, corresponding to the frequency range considered for the herring fish school at 430m depth

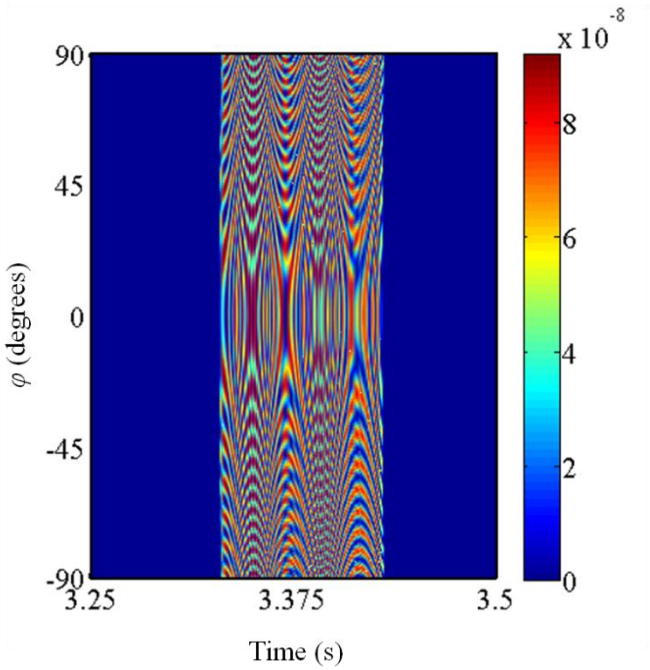

Figure 5-20: Pressure magnitude square as a function of angle (φ) in degrees and time in seconds for a hard sphere with frequencies 3-4kHz, corresponding to the frequency range considered for the herring fish school at 430m depth

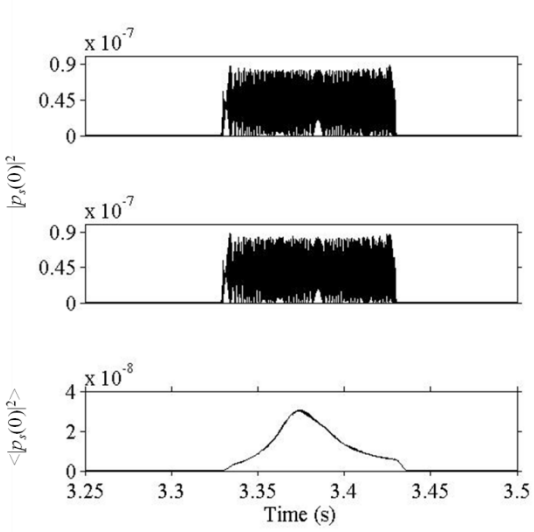

Figure 5-21: Pressure magnitude squared for the soft (top) and hard (middle) spheres and the spherical aggregation of herring fish at 430m depth (bottom)

The simulations discussed in this section are the most realistic set of simulations presented in this thesis, without considering multipath propagation, in that they consider scattering from omnidirectional point scatterers with herring fish properties such as fish flesh viscosity and swimbladder radius, obtained from a volume equivalent sphere of the swim bladder. Though clean results from the CBE simulations require thousands of realizations, which can be time consuming, these results show that there are significant differences in the scattered mean square pressure from the fish school from the original signal. Additionally, it shows that there are significant differences in the returns from the herring fish school from that of an equivalently sized hard or soft sphere in the shape of the backscattered time dependent signal and the start and end times of the signal for an aggregation of resonant scatterers.

5-4: Summary and Conclusions

In this chapter, broadband, frequency sweep signals were considered as the incident wave on spherical aggregations of scatterers. The first part of the chapter considered aggregations of ideal scatterers, with fixed scattering cross section, and the second half considered aggregations of scatterers with herring fish properties such as swimbladder volume and viscosity for varying depths. Results were compared by considering single, 64 and up to 4096 realizations with the original signal as well as the van Bladel (1968) spheres discussed in Chapter 4. The time delays in the signal were compared and the cross correlation was evaluated to draw more effective comparisons in the real part of the backscattered mean square pressure.

The findings from this chapter yield several conclusions: (*i*) The constraints considered in Chapters 3 and 4 to determine if a CBE peak results in the frequency domain are considered important in ensuring a CBE peak in the time domain as well. The CBE peak is still dependent on spacing, aggregation size and dimensionless scattering strength. In actual fish schools, however, an increase in the depth of the fish school in the ocean also increases the multiple scattering effects in the free space. (*ii*) The Foldy (1945) equations can be used to simulate an aggregation of omnidirectional point scatterers with herring fish school properties and CBE occurs for the aggregations considered. (*iii*) In the time domain, a backscattered pressure magnitude squared of a single realization of an aggregation of scatterers is very poorly correlated with the original signal, though the cross correlation fluctuations do increase with the number of scatterers. (*iv*) And, lastly, there are significant differences in the backscattered mean square pressure resulting from an aggregation of scatterers from that of an equivalently sized hard or soft sphere of the same size, both in the presence of a CBE peak as well as time delays in the signal.

As in Chapter 4, while CBE still may be too weak a phenomenon for use in discriminating schools of fish from other objects in practice; only if a wide range of angles could be measured over thousands of realizations, then it might provide an effective means of discrimination. Additionally, the work reported in this chapter also suggests that CBE isn't necessarily the only tool which can be used to gather information for discriminating fish schools from other scattering objects of comparable backscattering strength. In practice, the results shown in this chapter provide additional insight into how the returns from a fish school differ from that of a single scattering object which may be present in the ocean for all angles under idealized circumstances. Typically, in a downward looking echosounder system, where the simulation setup would be most applicable, information on the returns at other angles would not be able to be readily determined. However, the work reported in this chapter does not consider multiple scattering from scattering objects which are not omnidirectional and may also be present in the ocean or compression and expansion effects of the sphere which could also play a role. Discussion in Chapter 6 considers this even further by comparing the findings presented thus far with using the probability distribution function of the pressure amplitude and standard deviations of the collected samples which can be obtained in the backscatter direction.

CHAPTER 6

Backscatter Statistics and Connections to Ocean Acoustics Measurements

The work in this chapter describes a more common statistical discrimination technique to classify schools of fish involving the use of the probability distribution function of the mean-squared backscattered pressure. Analysis of this probability distribution function has been previously considered extensively (see Chapter 1). However, this chapter will explore the utility of the probability distribution function of the backscatter returns for classifying schools of fish from other objects. Additionally, the normalized echo amplitude probability distribution function from simulation is compared with distributions obtained via *in situ* measurements from schools of rockfish and small pelagic fish[2]. The chapter begins by first describing the methods and techniques utilized for analysis of the simulation and *in situ* measurement. Additionally, it also explains how an assessment is made for the goodness of a fit. It then shows the probability distribution functions for an aggregation of scatterers and how the standard deviation of a subset of samples can be used to effectively distinguish an aggregation of scatterers from a single large object in a free space environment. The conclusions from these findings are extended to schools of fish from ocean acoustics measurements and the distribution is modified slightly via a weighting function to account for the natural variability in the fish schools. Some of the findings in this chapter appear in Mookerjee and Dowling (accepted for JASA).

[2] The *in situ* measurement data was provided by Dr. Kelly Benoit-Bird of Oregon State University and Monterey Bay Aquarium Research Institute.

6-1: Methods and Technique

In this chapter, simulations are done using the geometry of Fig. 4-2. A plane wave with wave vector $\vec{k}$ along the *x*-axis illuminates an aggregation of scatterers centered at the origin. Unlike in Chapter 4 where a far field receiving ring is used to evaluate the returns at each angle from -180 to +180 degrees, only the backscatter direction, φ = 0, is considered here. The aggregations considered are spherical aggregations with scattering strengths of $0.21 \leq k\sqrt{\sigma_s} \leq 3.2$, $2.9 \leq ks \leq 6.4$ and $12 \leq ka \leq 32$ and prolate and oblate spheroids, where the equatorial and polar radii are ka_e = 16 and ka_p = 32 for the prolate spheroid and vice versa for the oblate spheroid. As in the rest of this thesis, for the simulations, the Foldy (1945) equations discussed in Chapter 2 are used in their dimensionless forms with length scales scaled by incident wave number, *k*, and pressures scaled by incident amplitude, *A*. Additionally, in the backscatter direction, pressures are normalized in two ways: (1) normalized pressure magnitude squared in dB, $10log_{10}(|p_s(0)|^2/<|p_s(0)|^2>)$, and (2) normalized echo amplitude, $|p_s(0)|/<|p_s(0)|^2>^{1/2}$ to describe the distribution of backscattered field amplitudes from the aggregation of scatterers.

The measurements were performed off the Oregon coast in the North Pacific Ocean at a latitude of 44°09’51.8”N and a longitude of 124°55’57.4”W. Two types of fish schools are considered: (1) rock fish, which were located near the seabed at depths of 100-175 meters and (2) small pelagic fish [typically consisting of herring, anchovies, sardines, shad and menhaden (NOAA fisheries, 2014)] which were located near at depths of 4-50 meters. Frequencies considered which illuminated the schools of fish were 18, 38, 70, 120 and 200 kHz via a downward looking echosounder, Simrad EK60. Figure 6-1 shows the scattering cross section σ_s (in m^2) obtained from the Love (1978) model (2-11) for (a) rockfish (ka_s = 2.3-25.6) at 150m

depth (resonance frequency at 430Hz) and (b) small pelagics (assuming the school is primarily composed of herring, ka_s = 0.53-5.88) at 25m depth (resonance frequency at 880Hz) in the ocean's water column for the frequencies of interest. Because the wave number scaled effective radius of the swimbladder is greater than one, here, the Foldy (1945) equations would not be comparable. Though the dimensionless scattering strength of each rockfish ($k\sigma_s^{1/2}$ = 3.25-3.5449 for 18-200kHz) is slightly higher than for each small pelagic fish ($k\sigma_s^{1/2}$ = 1.6-3.5 for 18-200kHz), rockfish are also bigger in size (28cm, ks = 21.1-235) compared to small pelagics (18cm, ks = 13.5-150) (Froese et al., 2012, Gauthier and Rose, 2001). Therefore, for these frequencies, the multiple scattering effects would be comparable, assuming that the small pelagics are primarily composed of herring.

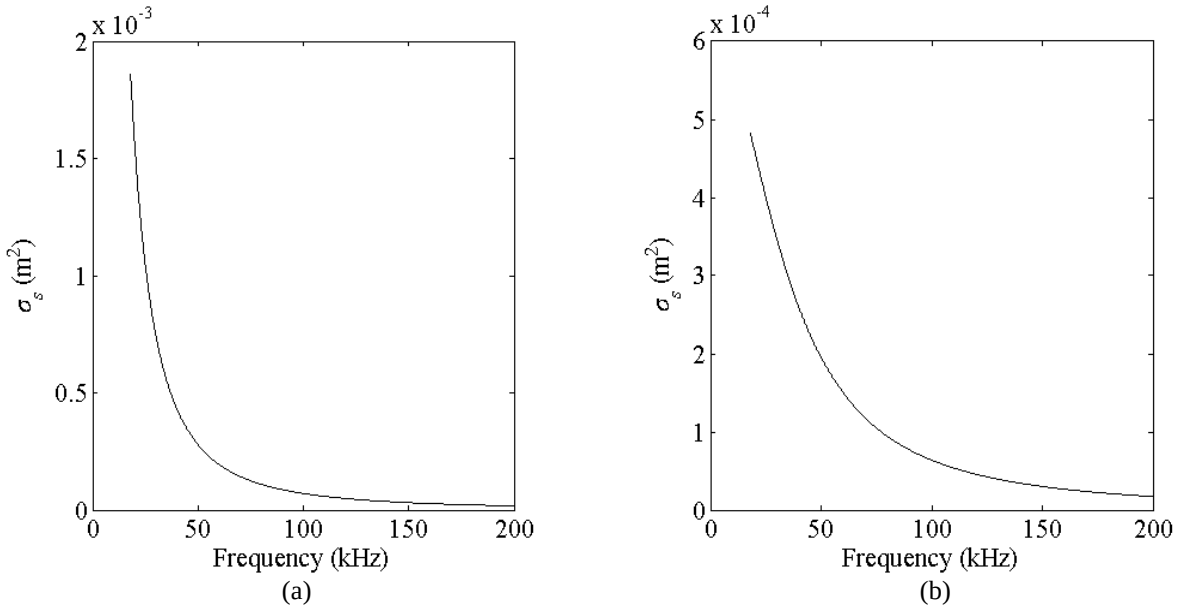

Figure 6-1: Dimensionless scattering strength as a function of frequency (in kHz) for a school of (a) rockfish at 150m depth (resonance at 430Hz) and (b) small pelagics at 25m depth (resonance at 880Hz) in the ocean's water column for the frequencies considered in the *in situ* measurements (18kHz-200kHz)

Returns were recorded in the form of volumetric scattering, S_v, in dB (Figure 6-2) using transducers 38-12 and 120-7C which were colocated broadcast transducer.

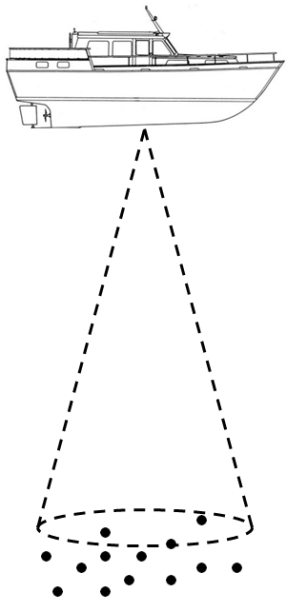

Figure 6-2: Ocean acoustic in situ measurement setup

The decibel S_v-values were converted to $|p|^2$ and then to pressure amplitude normalized by the root mean square of the pressure. Sample echograms, provided to the author by Dr. Kelly Benoit-Bird of the Monterey Bay Aquarium Research Institute, of typical shapes, orientation and composition of the fish school in the near bottom and in the near surface of the ocean are shown in Figure 6-3. In Fig. 6-3a), a school of rockfish illuminated at 38 and 70kHz is near the bottom of the ocean at a depth of 100-150m. Fig. 6-3b) shows a school of small pelagics at the same frequencies located near the surface of the ocean at 4-40m depth. The colors indicate the volumetric scattering strength, S_v, ranging from -60 to -30dB for the small pelagic fish schools and -80 to -40 dB for the rockfish. Color bars for the range for S_v values in the echogram were not provided, so the S_v dB ranges mentioned are extracted from the data set.

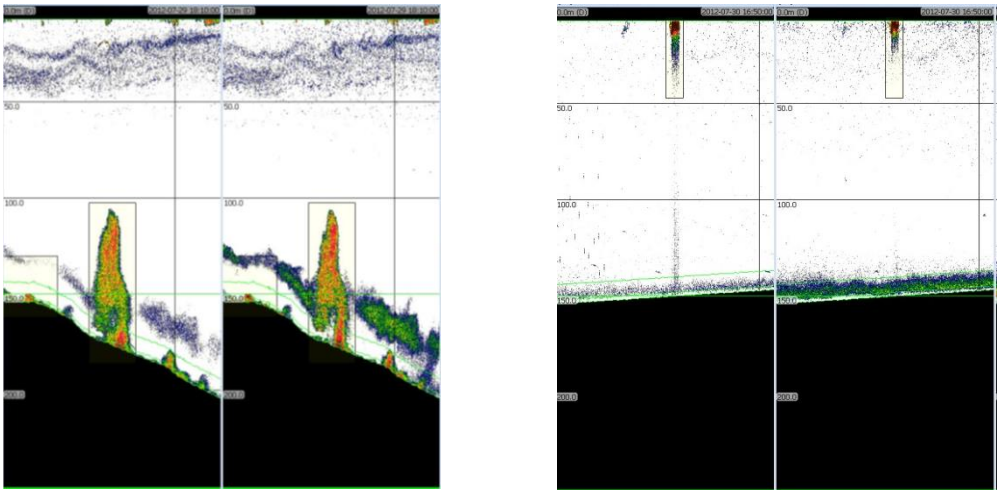

(a) (b)

Figure 6-3: Sample echograms from *in situ* measurements from fish schools located (a) near the bottom of the ocean and (b) near the surface of the ocean at frequencies of 38 kHz and 70kHz (prepared and provided by Dr. Kelly Benoit-Bird of the Monterey Bay Aquarium Research Institute)

In order to determine the distribution for the backscatter statistics, a histogram is prepared with 50-200 bins, depending of the number of samples collected of the fish school. The number of samples in the histogram is then normalized by the area under the histogram to produce a probability distribution function (PDF). Various types of fits are applied to the points which make up the probability distribution function from the aggregation of scatterers. The goodness of the fit, r^2, can be obtained by considering a data set with values, $y = [y_1 \ldots y_n]$ which has a mean of $\bar{y}$ and a model distribution consisting of values $f = [f_1 \ldots f_n]$:

$$r^2 \equiv 1 - \frac{\sum_i (y_i - f_i)^2}{\sum_i (y_i - \bar{y})^2}. \tag{6-1}$$

Typical values for r^2 range from $0 \leq r^2 \leq 1$ where $r^2 = 0$ indicates that there is no relationship between the data set and the prediction model and $r^2 = 1$ which suggests that the fitted model describes the data perfectly. Figure 6-4 shows some sample fits for low and high r^2 where the black hollow circles are the data and the black curve is of the model distribution. In Figure 6-4a),

the model misses all the points so it has an r^2 of only 0.0774. However, in Figure 6-4b), the model captures the points almost perfectly with an r^2 of 0.9975. Thus, r^2 needs to be as close to 1 as possible indicated the best fit to model to the actual distribution of the backscattering returns from the aggregation.

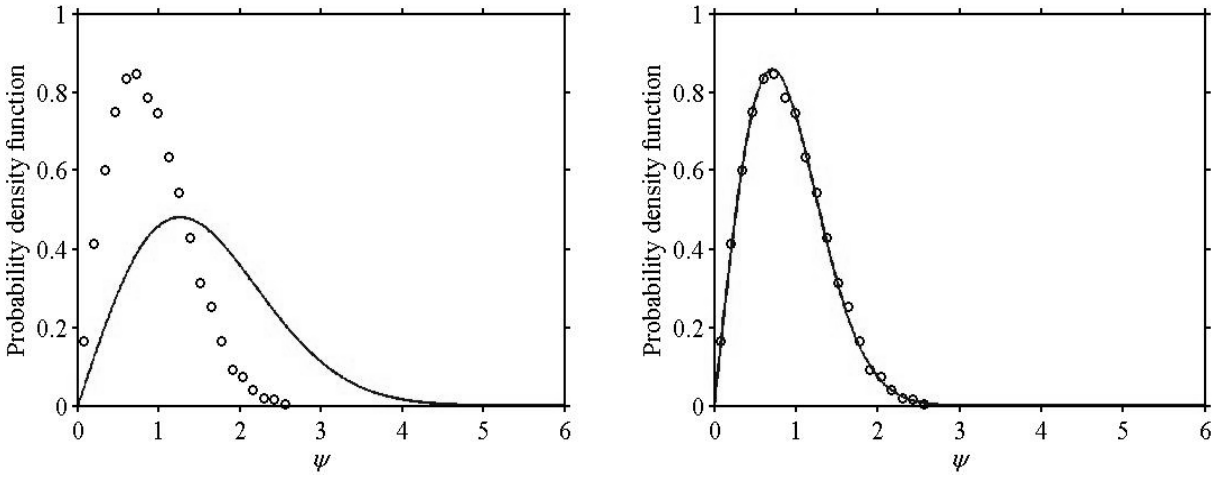

(a) (b)

Figure 6-4: Sample fits to model (—) the distribution of a data set (o) where the fit in (a) has a low r^2 of 0.0774 and (b) has a high r^2 of 0.9975

In this chapter, the probability distribution function for the backscattered returns from the simulation and the *in situ* measurements are plotted as points. A best fit distribution function is sought to fit these points. This distribution function is either a Rayleigh distribution or a smeared Rayleigh distribution (discussed in greater detail in Section 6-3). In order to assess how well the probability distribution function describes the backscattering, the goodness of fit parameter, r^2 is utilized. The best fit distribution visually passes through or is relatively near most of the points and has an r^2 as close to 1 as possible.

6-2: Simulation Results

In Chapter 4, the CBE peaks shown were determined as ensemble averages of $|p_s(\varphi)|^2$ from thousands of different realizations of the various random aggregations. For any particular scattering direction φ, the samples can be converted into a decibel value Ψ using their mean value: $\Psi = 10\log_{10}\left(|p_s(\varphi)|^2 \Big/ \left\langle |p_s(\varphi)|^2 \right\rangle\right)$. Then, the decibel values can be sorted into a histogram and normalized to form a probability density function (PDF) for Ψ. This conversion, sorting and normalization process was undertaken for the backscatter direction ($\varphi = 0$) for the 20 different random aggregation sets shown in Table 4-1. The results of this PDF construction process are shown on Figure 6-5(a) along with the extreme value distribution (Lawless 1982):

$$\mathrm{PDF}(\Psi) = \frac{1}{\sigma}\exp\left(\frac{\Psi}{\sigma} - \exp\left(\frac{\Psi}{\sigma}\right)\right) \tag{6-2}$$

having scale parameter, $\sigma = 10\log_{10}(e) \approx 4.34$. This distribution for the decibel-valued random variable Ψ is equivalent to a Rayleigh distribution, $\mathrm{PDF}(\psi) = 2\psi\exp\left(-\psi^2\right)$ for the amplitude ratio variable $\psi = |p_s(\varphi)| \Big/ \left\langle |p_s(\varphi)|^2 \right\rangle^{1/2}$ [see Fig. 6-5(b)], and both distributions have been considered in prior studies of backscattering from fish schools (Chu and Stanton 2010, Demer et al. 2009, Stanton et al. 2004, Mozynski 2002). Since the scatterers are randomly placed in the aggregation and a large number of samples are considered for these simulations ($O(10^3)$), via the central limit theorem, the real and imaginary parts of pressure are normally distributed. Thus, the $|p_s|$ is Rayleigh distributed (Abraham et al. 2011, Rice 2010). Here, the r^2 for the distribution fitting was 0.9975.

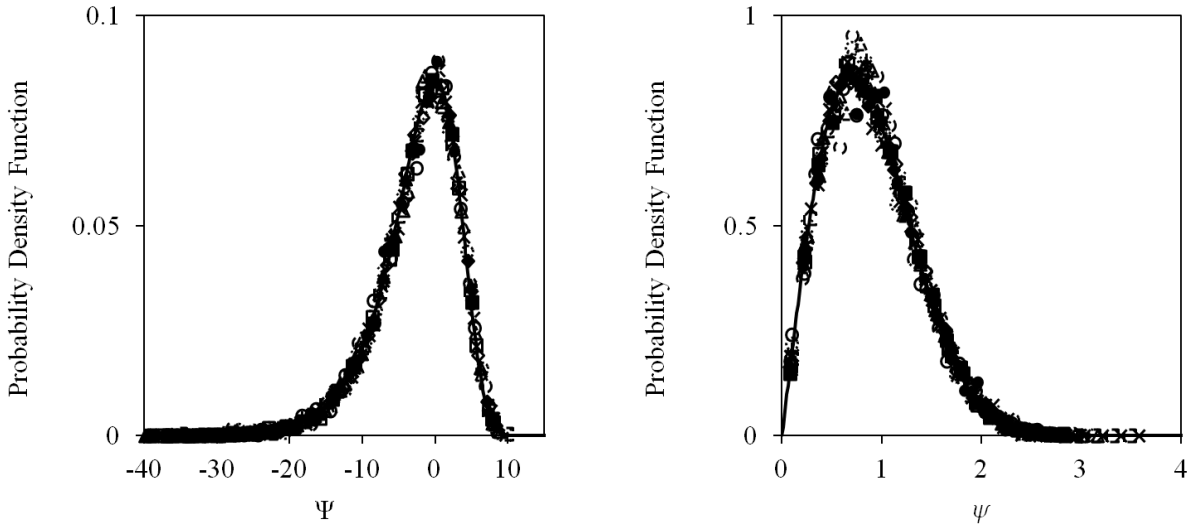

Figure 6-5: Probability distribution functions (PDFs) for $\Psi = 10\log_{10}(|p|^2/\langle|p|^2\rangle)$ in dB (a), and for $|p|/\langle|p|^2\rangle^{1/2}$ (b) from the 20 parameter sets considered in Chapter 4. The (a) extreme value distribution and (b) Rayleigh distribution appears as a solid curves. The PDFs from the simulations are statistically identical, regardless of aggregation geometry, dimensionless spacing and dimensionless scattering strength. Furthermore, all PDFs of Ψ are well-matched to the extreme value distribution, and all PDFs of ψ are well-matched to the Rayleigh distribution.

Interestingly, the Ψ- and ψ- distributions from the simulations are all well matched to the fitted extreme value (6-2) and Rayleigh distributions, respectively, regardless of the shape or orientation of the aggregation for all values of *ka*, *ks* and $k\sigma_s^{1/2}$ considered in this study. Thus, backscatter samples (in dB) from an aggregation of omnidirectional scatterers follow (6-2) independently of: the size and shape of the aggregation, the spacing and strength of the scatterers and the importance of multiple scattering within the aggregation.

The invariance of the distribution for Ψ shown in Fig. 6-5 suggests that a remote aggregation vs. large object discrimination technique might be possible when propagation fluctuations are weak or absent using a countable number of independent backscatter samples, perhaps obtained from multiple pings from a monostatic active sonar system. In real ocean remote sensing scenarios when variations in backscattered intensity are caused by target and

environmental fluctuations, echo statistics from hundreds or thousands of pings may be needed to discriminate between clutter and targets of interest (Abraham et al. 2011). Thus, the simpler objective of determining the number (q) of backscatter samples necessary to estimate the standard deviation of Ψ to within a specific dB tolerance (ε) with 95% confidence is pursued here for the ideal case when multipath propagation and propagation fluctuations are weak or absent. This ideal case may be applicable to the usual downward looking echosounder geometry where single path acoustic propagation is most important.

Seven values of q (4, 8, 16, 32, 64, 128 and 256) were considered for this sample size determination effort and statistical results were generated by direct interrogation of the Ψ-samples used to produce Figure 6-5(a). In particular, q samples of Ψ were repeatedly drawn at random from an ensemble of 15000 simulation samples. Then, the standard deviation, σ_q, computed from each set of q samples was compared to that of the extreme value distribution given by (6-2) which has a mean of -2.507 dB and a standard deviation of σ_{evd} = 5.570 dB. Using this information, the probability that $|\sigma_q - \sigma_{evd}| \leq \varepsilon$ was compiled as a function of ε and q. Finally, the tolerance ε for a probability of 95% was determined for the seven q values listed above and these results are shown in Table 6-1. As expected, the tolerance ε falls as q increases, descending below 2.0 dB at q = 32, reaching a value of 1.0 dB at q = 128 and falling to 0.7 dB at q = 256. Although these results were generated for an ideal (free space) environment, they should still be relevant when the acoustic propagation is single path and relatively stable. But more importantly, these results indicate that the inherent fluctuations associated with independent backscatter samples from an aggregation of scatterers might be adequately characterized by tens or hundreds of independent samples, while thousands of independent samples were needed over a nontrivial range of the scattering angle φ from the same

aggregations to reveal CBE peaks shown in Chapter 4. Thus, even when confronting real ocean scenarios rich with natural variations not included in the simulations, the conventional active sonar approach of documenting and assessing backscatter fluctuations as a means of remote aggregation vs. large object discrimination should be superior to determining the presence or absence of a CBE peak for the same task. This conclusion is additionally supported by the fact that an aggregation of scatterers may not produce a CBE peak if it is too small or has an insufficient density of scatterers or is composed of scatterers of insufficient cross section.

Table 6-1: 95% confidence tolerances (ε) for estimating the population standard deviation from q samples of Ψ, the normalized backscattered mean-square pressure in dB.

q	ε for 95% confidence (dB)
4	4.7
8	3.6
16	2.7
32	1.9
64	1.4
128	1.0
256	0.7

6-3: *In situ* measurement analysis

For the remainder of this chapter, *in situ* measurements are considered. Here, the comparisons are made in the ψ-distributions between an aggregation of scatterers in free space from a school of fish in the ocean. To perform this analysis, acoustic survey results are collected in the form of the volumetric scattering strength, S_v in dB (MacLennan et al. 2002):

$$S_v = 10\log_{10}\left(\frac{|p(0)|^2}{|p_{inc}|^2}\right). \tag{6-3}$$

Pings are sent downward as a ship moves over the fish school and the returns are recorded at different depths via the timing of the backscattered signals to determine S_v values at each driving distance and depth, both of which are in meters. Figure 6-6 shows a sample volumetric scattering data set for a near surface fish school. Higher S_v values indicate the region occupied by the fish school and lower S_v values correspond to background of weak tenuous scattering from the nearby ocean.

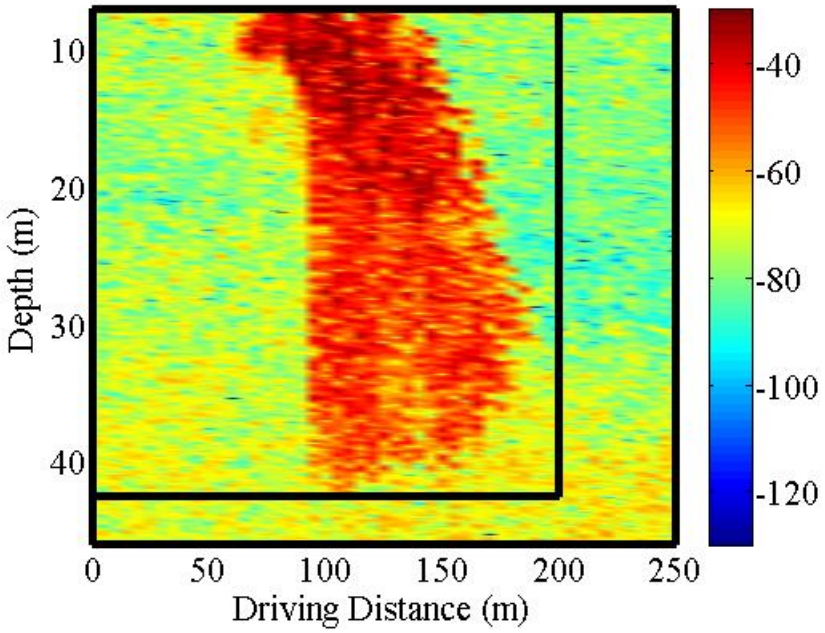

Figure 6-6: Sample *in situ* measurement S_v data from a near surface fish school in dB as a function of depth in meters and driving distance in meters. The samples in the black box make up the region which surrounds the aggregation in the calculation of the total backscattered pressure-magnitude-squared, $\sum_i \sum_j |p|^2$.

In order to isolate the fish school in an image such as Fig. 6-6, a threshold (6-4) is applied to ensure that 99% of the scattering from the fish school is considered. Here, $\sum_i \sum_j |p|^2$ is the total backscattered pressure-magnitude-squared in a rectangular region that surrounds the

aggregation, and $\sum_i \sum_j \eta_{ij} |p|^2$ is the total backscattered pressure-magnitude-squared from the background. Here, η_{ij} is chosen so that equality is most closely approached in (6-4); it can either be 0 or 1, with $\eta_{ij} = 0$ indicating a point within the fish school and $\eta_{ij} = 1$ indicating a point in background region surrounding the fish school. The indices (i, j) correspond to horizontal and vertical locations in the (depth, driving distance) coordinates shown in Fig. 6-6. After ensuring that 99% of the scattering from the fish school is captured, any holes in the school are filled in to make the school continuous (simply connected). For the fish school in Fig. 6-6, the final mask is shown in Fig. 6-7. The black region indicates where $\eta_{ij} = 0$ (the fish occupied region) and the while part indicates $\eta_{ij} = 1$ (the background region). The S_v-values from the background region were not included in the backscattered probability distribution function analysis.

$$\frac{\left| \sum_i \sum_j |p|^2 - \sum_i \sum_j \eta_{ij} |p|^2 \right|}{\sum_i \sum_j |p|^2} \geq 0.99 \tag{6-4}$$

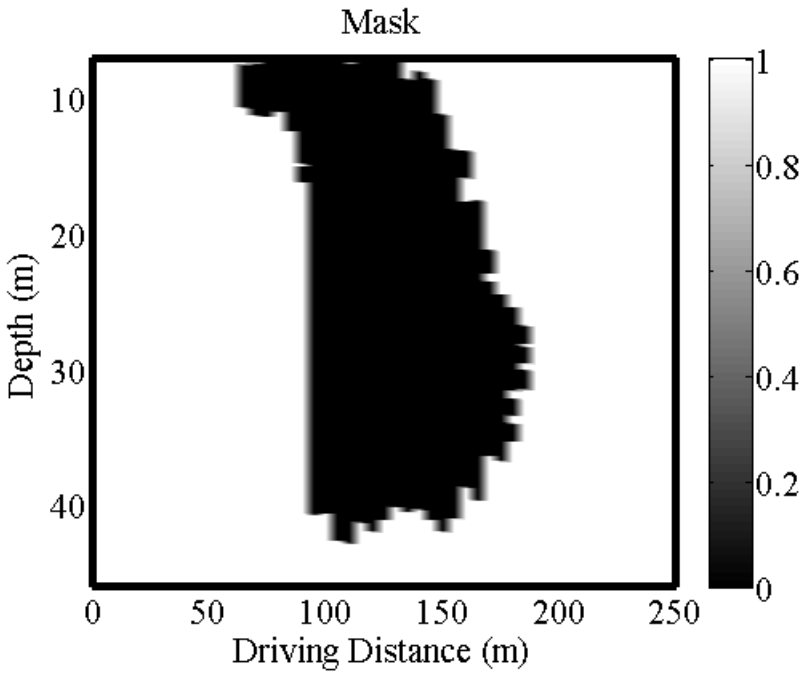

Figure 6-7: Mask for the fish school in Figure 6-6 where black (0) indicates the region considered to be a part of the fish school and white (1) indicates the background region

However, the (i, j) indices where $\eta_{ij} = 0$ are used to create a set of corresponding $|p|^2$ samples, that are then normalized by the root-mean-squared of this set, $\langle|p|^2\rangle^{1/2}$, to yield samples of the normalized echo amplitude, ψ.

6-4: *In situ* Measurement Results and Discussion

In this section, two different distributions will be considered for fitting the various samples sets of ψ. Fish schools are first fitted to a Rayleigh distribution, because it was found to describe the simulation results well. However, a single Rayleigh distribution does not account for natural spatial variability in fish density. Thus, the second part of this section considers a smeared distribution, in the form of a continuous sum, or integral, of Rayleigh distributions with a weighting function. This distribution does a much better job of capturing the natural variability of fish schools, and possible predictions on the fish school composition will be discussed.

1. Rayleigh Distribution

For the analysis of the distributions of the fish schools, the distributions of the backscattered returns from the aggregations are fitted to the Rayleigh distribution for 60 of the *in situ* measurement data sets which could be used for the 18, 38, 70, 120 and 200 kHz frequencies (6 schools and five frequencies for 30 data sets from the rockfish, and 6 schools and five frequencies for 30 data sets for the small pelagic fish schools). For this fitting, a Rayleigh distribution with mean $<\psi>$ is considered (6-5). Here, this mean value is considered the free parameter and therefore, this fitting is considered a one parameter fit (Papoulis 1991).

$$PDF(\psi) = \frac{\psi\pi}{2<\psi>^2} \exp\left(-\frac{\psi^2\pi}{4<\psi>^2}\right) \tag{6-5}$$

Figure 6-8 shows the best fit Rayleigh distribution for backscatter samples from a natural fish school in linear-linear (top) and log-log (bottom) coordinates for the probability distribution function of the fish school against the normalized echo amplitude, ψ. Visually, the distribution shape of the normalized echo amplitude for this fish school does appear to resemble that of a Rayleigh distribution (initial increase for smaller values of ψ and then a gradual decrease, approaching 0 for larger values of ψ). However, the best fit distribution for the points shown produces an r^2 of 0.51, and this indicates that the backscatter distribution for the particular fish school considered is not Rayleigh distributed. Results from the other *in situ* data sets are tabulated in Table 6-2. Here, $<\psi>$ and r^2 values are shown as the second and third columns in Table 6-2a) and b) for the rockfish and small pelagics, respectively. There are a few values in Table 6-2a) and b) which produce an r^2 near 1 (0.9543 and 0.9282). In Chu and Stanton (2010)

and Lee and Stanton (2014), it was found that the distribution may approach Rayleigh when the number density of the fish school is low. Therefore, this may be also the case for these schools.

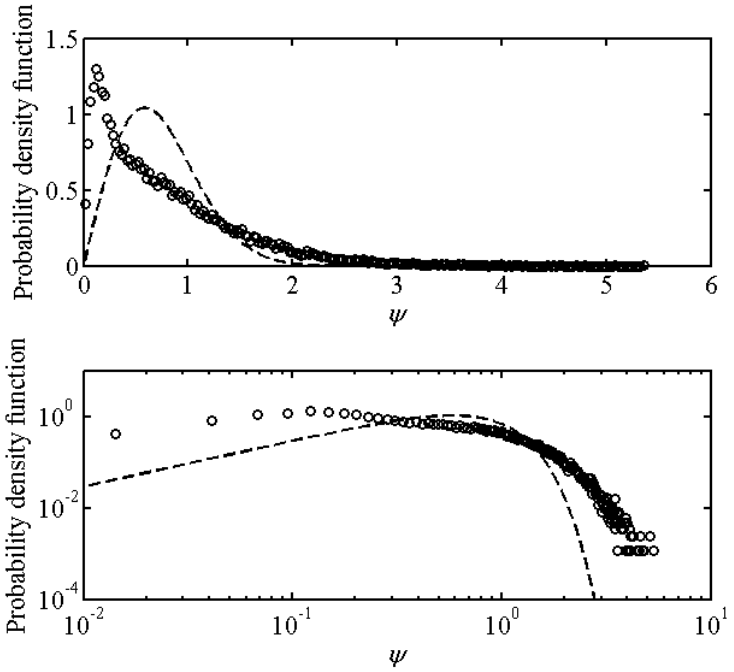

Figure 6-8: The probability distribution function is generated for $\psi = |p|/\langle|p|^2\rangle^{1/2}$ (o) obtained from a school of small pelagic fish at 38kHz frequency (2, 38 in Table 6-2b)). The best fit Rayleigh distribution is fitted to these points (----). The r^2 for this fitted distribution is 0.5081, which suggests that the echo amplitude for this fish school is non-Rayleigh, even though visually it appears that it might be Rayleigh.

Table 6-2: The Rayleigh distribution is fitted to the probability distribution function of the normalized echo amplitude for the (a) rockfish and (b) small pelagic fish schools. In all the cases considered, the best fitted Rayleigh distribution was a poor fit with an r^2 averaging around 0.51.

(a) Rockfish (School No., Frequency in kHz)	$\langle\psi\rangle$	r^2
1, 18	0.5	0.3681
1, 38	0.51	0.5252
1, 70	0.03	0.822
1, 120	0.03	0.8706
1, 200	0.02	0.6791
11, 18	0.68	0.3752
11, 38	0.59	0.3512
11, 70	0.65	0.3049
11, 120	0.65	0.3585
11, 200	0.63	0.4169

13, 18	0.57	0.6994
13, 38	0.59	0.7177
13, 70	0.21	0.6313
13, 120	0.33	0.7153
13, 200	0.42	0.7144
16, 18	0.48	0.2848
16, 38	0.42	0.5544
16, 70	0.24	0.2378
16, 120	0.4	0.3423
16, 200	0.42	0.467
20, 18	0.55	0.1783
20, 38	0.46	0.6379
20, 70	0.52	0.4768
20, 120	0.64	0.5441
20, 200	0.68	0.552
22, 18	0.75	0.8272
22, 38	0.52	0.9282
22, 70	0.46	0.7495
22, 120	0.45	0.817
22, 200	0.54	0.7408

(b) Small pelagics (School No., Frequency in kHz)	$<\psi>$	r^2
1, 18	0.34	0.3066
1, 38	0.09	0.5031
1, 70	0.15	0.3732
1, 120	0.17	0.2306
1, 200	0.22	0.2689
2, 18	0.72	0.3737
2, 38	0.09	0.5081
2, 70	0.15	0.3732
2, 120	0.17	0.2306
2, 200	0.2	0.2689
3, 18	0.39	0.4973
3, 38	0.2	0.5915
3, 70	0.15	0.6813
3, 120	0.18	0.854
3, 200	0.22	0.9513
5, 18	0.6	0.4002
5, 38	0.43	0.4569
5, 70	0.29	0.6672
5, 120	0.2	0.7013

5, 200	0.25	0.738
7, 18	0.03	0.5544
7, 38	0.28	0.4561
7, 70	0.03	0.5412
7, 120	0.05	0.8323
7, 200	0.03	0.917
9, 18	0.2	0.2837
9, 38	0.11	0.7855
9, 70	0.1	0.4872
9, 120	0.01	0.5629
9, 200	0.05	0.5892

In this section, the Rayleigh distribution was used to fit the distribution of the normalized echo amplitude. This was utilized since it appeared to describe the backscattered returns from the simulation data remarkably well. Additionally, for a large number of samples, as per the central limit theorem, it would make sense that the distribution would be Rayleigh. However, for the *in situ* measurements, the Rayleigh distribution fails to describe the distribution of the backscattered returns because there is natural variability in fish schools located in the ocean's water column that contribute to the differences in the backscattering returns. Consequently, to account for these differences, a smearing distribution is considered which allows an actual backscatter distribution to be composed of a continuous superposition of Rayleigh distributions having different values of $<\psi>$.

2. Smeared Rayleigh Distribution

In Section 1, a Rayleigh distribution was used to model the backscattering from the rockfish and small pelagic fish schools. This was utilized since it appeared to be successful in describing the normalized echo amplitude distribution for an aggregation of omnidirectional

point scatterers simulated via the Foldy (1945) equations. However, a single Rayleigh distribution is generally unsuccessful for describing the *in situ* measurements due to the natural variability of the ocean's water column and the fish school itself. Thus, a smeared Rayleigh distribution function is considered, where a weighting function, $A(<\psi>)$, and a continuous sum of varying-mean Rayleigh distributions is utilized to account for the natural variability.

The smeared Rayleigh distribution consists of a normalized weighting function multiplied with a variable-mean-value Rayleigh distribution that is integrated over all possible mean values. This distribution models the natural variability of the fish school by considering allowing $<\psi>$ to take on a range of values for a natural fish school. This approach generally performs well in fitting the 60 rockfish and pelagic fish data sets previously fitted with a Rayleigh distribution. This function appears as follows in (6-4) where $A(<\psi>)$ is the weighting function, $<\psi>$ is the mean, $<\psi>_{min}$ is the minimum mean considered, and $<\psi>_{max}$ is the maximum mean considered in the distribution. Here, the value for $<\psi>_{min}$ modulates the distribution function for the smaller values of ψ and $<\psi>_{max}$ adjusts the distribution function for larger values of ψ.

$$PDF(\psi) = \frac{\psi\pi}{2}\left[\int_{<\psi>=<\psi>_{min}}^{<\psi>_{max}} \frac{A(<\psi>)}{<\psi>^2}\exp\left(-\frac{\psi^2\pi}{4<\psi>^2}\right)d<\psi>\right] \Bigg/ \int_{<\psi>=<\psi>_{min}}^{<\psi>_{max}} A(<\psi>)d<\psi> \qquad (6\text{-}4)$$

Since $<\psi>_{max}$ controls the larger values of the distribution and most of the $PDF(\psi)$ values for large ψ approaches zero, for simplicity, $<\psi>_{max}$ is set to 2. This value was selected, because it appeared that in most cases, $<\psi>_{max}$ hovered between 1 and 3 to attain the maximum r^2. There were a few instances where $<\psi>_{max}$ exceeded 3 to obtain the best r^2, but for these cases, the r^2 only improved by a few ten thousandths.

Additionally, it was found, from numerical exploration of several polynomial weighting functions which maximized the r^2, that the Lorentzian most simply describes the weighting function for the small pelagics and rockfish. This weighting function was selected for this reason and because it is non-negative. Any biological relevance of the Lorentzian for the fish schools is not known and is suggested as future work in Chapter 7. Thus, the form of the weighting function considered to model the natural variability is shown as (6-6).

$$A(<\psi>) = (<\psi>^2 + b)^{-1} \tag{6-6}$$

For this function, b is a constant added to the mean squared $<\psi>^2$. When taken together, (6-4) and (6-5) describe a two parameter fit ($<\psi>_{min}$, and b are the parameters) to the measured *in situ* backscatter data.

Table 6-3 summarizes the specific parameters needed to produce a best fit for the backscattered distribution in the form of the normalized echo amplitude (a) for the rockfish and (b) for the small pelagic fish. In comparison to the Rayleigh distribution, the r^2 values have improved significantly averaging to 0.975. Additionally, it should also be noted that the normalized echo amplitude probability distribution function is frequency dependent for the fish schools, a finding consistent with that of Lee and Stanton (2016). Figure 6-9 shows the best fit distribution (----) in (top) linear scale and (bottom) logarithmic scale for the normalized echo amplitude of a school of the small pelagic fish school at 200kHz (o) with values of b = 0.0012 and $<\psi>_{min}$ = 0.009. This fitted distribution produces r^2 = 0.9486. Considering the logarithmic plot, it appears that the fit performs poorly because of the lowest bin of ψ. This may be due to the fact that at 120 and 200kHz, the scattering from krill is also the strongest (Miyashita et al., 1996). Thus, the probability distribution function of the normalized echo amplitude from the school of fish may have also been impacted by the superimposed echoes from krill. Additionally,

applying the threshold (6-3) to the fish school yielded only 1500 samples. Other instances of lower values of r^2 also occur at frequencies where other marine life are resonant (18kHz is also the resonance frequency of zooplankton (Korneliussen and Ona, 2003)) or when a limited number of samples are acquired from the *in situ* measurement.

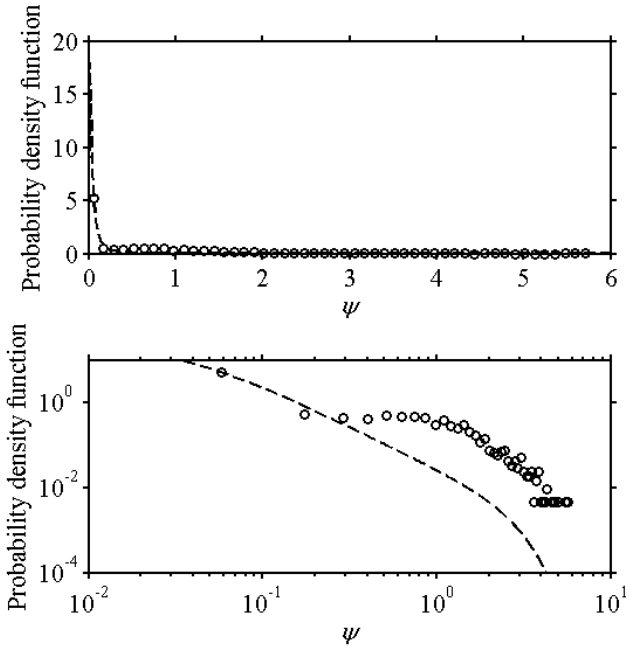

Figure 6-9: The probability distribution function of $\psi = |p|/\langle|p|^2\rangle^{1/2}$ in the backscatter direction for a small pelagic fish school at 200kHz (o) is considered. The points are fitted using a best fit smeared Rayleigh distribution (----). Of all the *in situ* measurement data considered, this distribution function had the worst fit to the points (r^2 is 0.9486). This is likely because the resonance frequency of krill (co-located with this school) is also at 200kHz which would have contributed to the poorly fit high amplitude scattering tail.

The average fit for the distribution of the backscattering from fish schools was $r^2 = 0.975$. Figure 6-10 shows the distribution of the backscattered returns from a school of rockfish at 18kHz (o) when fitted with the smeared Rayleigh distribution (----) for $b = 0.1868$ and $\langle\psi\rangle_{min} = 0.0196$. The r^2-value for the fitted smear distribution was 0.9712. In this case, the fit is looks significantly better in log-log coordinates compared to Fig. 6-9. In linear-linear coordinates, the distribution narrowly misses the maximum value for the measurement backscattered distribution.

For the other data sets considered, most of the fits appeared as in Figure 6-10 with just a couple of data points not lying on or near the fitted distribution.

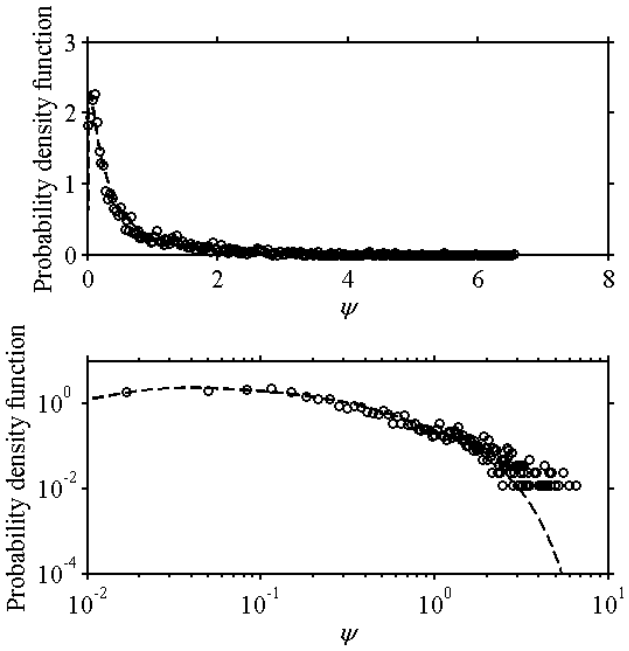

Figure 6-10: The probability distribution function of $\psi = |p|/\langle|p|^2\rangle^{1/2}$ in the backscatter direction for a school of rockfish at 18kHz (o) is considered. The points are fitted using a best fit smeared Rayleigh distribution (----). This smeared Rayleigh distribution yielded a goodness of fit value of $r^2 = 0.9712$ and is around the average r^2 for the smeared Rayleigh distribution fitted to the probability distribution function of $\psi = |p|/\langle|p|^2\rangle^{1/2}$ for the fish schools.

Figure 6-11 shows the distribution for the best fitted distribution. This school consisted of the rockfish which illuminated at a frequency of 70kHz. The parametric values for this fit were $\langle\psi\rangle_{min} = 0.0437$ and $b = 0.0955$. In this case, most of the points passed through the curve or were slightly above or below the curve. Additionally, since other marine life in the ocean which may contribute to the backscattering such as zooplankton and krill, are not resonant at this frequency, this fitting solely models the backscattered distribution from the rockfish with the scattering from other life forms minimized unlike in the cases where the r^2 is low.

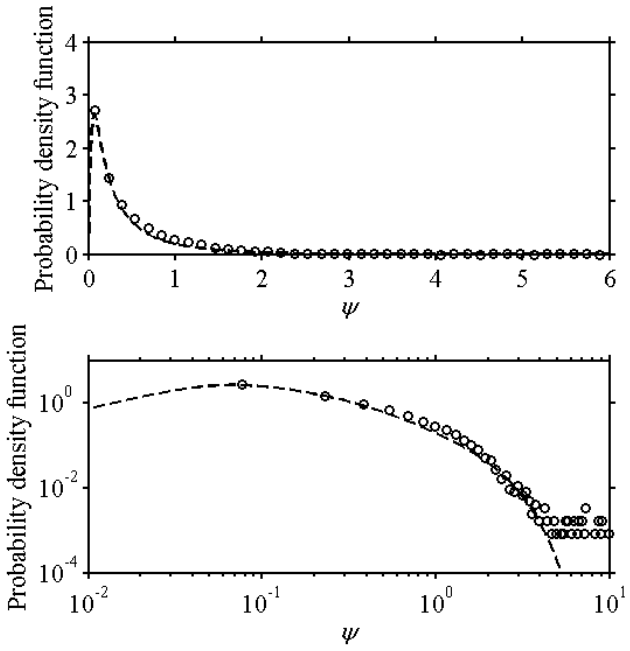

Figure 6-11: The probability distribution function of $\psi = |p|/\langle|p|^2\rangle^{1/2}$ in the backscatter direction for a school of rockfish at 70kHz (o) is considered. The points are fitted using a best fit smeared Rayleigh distribution (----). This smeared Rayleigh distribution yields a goodness of fit value of $r^2 = 0.9931$. This fitting was one of the best smeared Rayleigh distributions considered for the *in situ* measurements analyzed.

Table 6- 3: The smeared Rayleigh distribution is fitted to the probability distribution function of $\psi = |p|/\langle|p|^2\rangle^{1/2}$ of the *in situ* measurements for the fish schools. The fitting parameters in the smeared Rayleigh distribution of $\langle\psi\rangle_{min}$ and b for the schools of (a) rockfish and (b) small pelagics are tabulated. In all these cases, since the r^2 is close to 1, the fitted smeared distribution ($r^2_{avg} = 0.975$) is a significant improvement to the best fit Rayleigh distribution ($r^2_{avg} = 0.51$).

(a) Rockfish				
School No., Frequency in kHz	Sample Size	$\langle\psi\rangle_{min}$	b	r^2
1, 18	5800	0.0073	0.2916	0.9669
1, 38	5800	0.0165	0.3913	0.9848
1, 70	5800	0.0226	0.0139	0.9825
1, 120	5800	0.0219	0.0091	0.9832
1, 200	5800	0.0048	0.0081	0.9705
11, 18	5037	0.0050	1.1109	0.9818
11, 38	5037	0.0269	0.5062	0.9843
11, 70	5037	0.0180	0.4755	0.9667
11, 120	5037	0.0162	0.6969	0.9834
11, 200	5037	0.0243	0.7682	0.9852
13, 18	9456	0.0440	0.8115	0.9865
13, 38	9456	0.0371	0.9303	0.9816
13, 70	9456	0.0437	0.0955	0.9931

13, 120	9456	0.0699	0.1383	0.9903
13, 200	9456	0.0483	0.2812	0.9823
16, 18	6408	0.0000	0.2001	0.9723
16, 38	6408	0.0305	0.3759	0.9788
16, 70	6408	0.0000	0.0558	0.9922
16, 120	6408	0.0188	0.1843	0.9931
16, 200	6408	0.0247	0.3074	0.9917
20, 18	17311	0.0124	0.2438	0.9623
20, 38	17311	0.1135	0.3313	0.9929
20, 70	17311	0.0079	0.5533	0.9918
20, 120	17311	0.0065	1.3764	0.9765
20, 200	17311	0.0061	1.4966	0.9564
22, 18	66943	0.0402	4.0317	0.9633
22, 38	66943	0.2593	0.0694	0.9848
22, 70	66943	0.0926	0.3056	0.9854
22, 120	66943	0.1355	0.2067	0.9812
22, 200	66943	0.0587	0.5948	0.9815

(b) Small Pelagics				
School No., Frequency in kHz	Sample Size	$\langle\psi\rangle_{min}$	B	r^2
1, 18	2705	0.0196	0.1868	0.9712
1, 38	2705	0.0253	0.0083	0.9879
1, 70	2705	0.0273	0.0251	0.9716
1, 120	2705	0.0116	0.0278	0.9836
1, 200	2705	0.0000	0.0422	0.9738
2, 18	4209	0.0091	1.0952	0.9696
2, 38	4209	0.0353	0.1583	0.9608
2, 70	4209	0.0223	0.0795	0.9537
2, 120	4209	0.0000	0.1286	0.9853
2, 200	4209	0.0000	0.1755	0.9815
3, 18	1058	0.0542	0.3101	0.9843
3, 38	1058	0.0503	0.0461	0.9903
3, 70	1058	0.0553	0.0232	0.9907
3, 120	1058	0.0936	0.0033	0.9933
3, 200	1058	0.1264	0.0000	0.987
5, 18	1529	0.0193	0.5219	0.9553
5, 38	1529	0.0414	0.2981	0.9924
5, 70	1529	0.0638	0.0909	0.9911
5, 120	1529	0.0524	0.0862	0.9873
5, 200	1529	0.0679	0.1319	0.9862
7, 18	2378	0.0000	0.0885	0.9673
7, 38	2378	0.0408	0.2097	0.9849

7, 70	2378	0.0000	0.0366	0.9556
7, 120	2378	0.0219	0.0065	0.9536
7, 200	2378	0.0090	0.0012	0.9486
9, 18	5992	0.0379	0.0677	0.9506
9, 38	5992	0.0569	0.0024	0.9925
9, 70	5992	0.0303	0.0096	0.9751
9, 120	5992	0.0000	0.0116	0.9731
9, 200	5992	0.0000	0.0035	0.9736

In this section, two different fits were considered to model the backscattered distribution obtained from the *in situ* measurements. The first fit was a Rayleigh distribution which fitted the simulation backscattered probability distribution function remarkably well and the second fit was a smeared Rayleigh distribution function which is a continuous sum of weighted Rayleigh distributions for varying means. The goodness of fit for the Rayleigh distribution typically averaged at $r^2 = 0.51$, whereas the goodness of fit for the smeared Rayleigh distribution averaged at $r^2 = 0.975$. For all the data sets considered, the smeared Rayleigh distribution was a clear improvement to a single Rayleigh distribution fit.

6-5: Summary and Conclusions

Unlike in Chapters 3-5 where the coherent backscatter enhancement was considered to simulate and analyze the backscattered returns from aggregations of omnidirectional point scatterers, this chapter (6) has focused on using only the returns in the backscatter direction to classify schools of fish. Via simulation, it has been shown that the distribution of the backscattered normalized pressure magnitude squared, $10\log_{10}(|p_s|^2/\langle|p_s|^2\rangle)$, in dB, is the extreme value distribution, or a product of exponentials, and the distribution of the normalized echo amplitude, $|p_s|/\langle|p_s|^2\rangle^{1/2}$, is the Rayleigh distribution. Using the expected standard deviation of the fitted extreme value distribution, σ_{evd}, and the standard deviation of a subset of simulation

samples, σ_q, it has been shown that as few as 32 samples were needed to get within 2dB of the standard deviation of the extreme value distribution 95% confidence. In contrast, thousands of samples were needed to observe a peak from the coherent backscatter enhancement, which was only observed if the multiple scattering effects were strong. Therefore, it was observed that classification using a standard deviation of the backscattered normalized pressure magnitude square is a more robust technique than using the mean of the pressure magnitude squared. The second part of this chapter focused on using *in situ* measurements from schools of rockfish and small pelagics in the water column. In this set up, it was found that a single Rayleigh distribution does not fit *in situ* measured probability distribution functions, yielding best fits with average r^2 values of 0.51. However, a weighted continuous sum of varying-mean Rayleigh distributions (a smeared Rayleigh distribution), is a better fit with average r^2 values 0.975. The weighting function considered to describe the returns from the different fish schools was a Lorentzian.

The findings in this chapter suggest the following: (*i*) Using simulation, the probability distribution function describing the backscattered normalized pressure magnitude squared in dB is the extreme value distribution and the normalized echo amplitude is the Rayleigh distribution. These two findings are unsurprising since the two random variables, ψ and Ψ, are algebraically related. (*ii*) Fewer samples are needed to classify an aggregation of omnidirectional point scatterers using the standard deviation of the samples. While thousands of realizations were needed to notice a peak using the ensemble average of scattered pressure magnitude squared, as few as 32 samples were needed to estimate the population's standard deviation to within 2 dB at the 95% confidence level. (*iii*) When considering normalized echo amplitude, using *in situ* measurements, the Rayleigh distribution fails to model the backscattered distribution for rockfish or small pelagics. Instead, a weighted continuous sum of Rayleigh distributions of varying means

is utilized and this distribution performs significantly better for the data sets considered. (*iv*) This continuous sum is expressed as an integral and the weighting function for the rockfish and small pelagics was the Lorentzian function. Thus, two free fitting parameters are used for the fitting. Both the fitting parameters $<\psi>_{min}$ and b influence the probability distribution function for smaller values of the normalized echo amplitude. While $<\psi>_{min}$ gives a rough estimate of the lower values of ψ, b fine tunes the function so that the distribution better fits the points. Since it was observed that the maximum mean of the normalized echo amplitude was around two, $<\psi>_{max}$ was set to two. (*v*) Lower r^2 values primarily occur at frequencies where zooplankton (18kHz) or krill (120 and 200kHz) are also resonant. This suggests that in addition to determining the presence of a fish school in the ocean, multi-frequency echo sounder investigations have the potential to determine the homogeneity of the marine life also within the region considered the fish school.

In comparison to using the coherent backscatter enhancement to classify schools of fish, the statistical techniques for analyzing backscatter returns are superior. Measuring a coherent backscatter enhancement peak requires thousands of realizations and many angular measurements which are typically not possible. Additionally, if a school of fish consists of weak scatterers, there may not necessarily be a CBE peak, whereas the probability distribution function would always exist, regardless of the strength of the multiple scattering effects.

In this chapter, the method of using the probability distribution function to characterize the backscattered returns from schools of fish was considered, an approach has been utilized for the last 30 years (Huang and Clay, 1980). During this time, the distributions fitted to the normalized echo amplitude probability distribution functions have been as Rayleigh (Huang and Clay 1980), Ricean (Stanton and Clay 1986), mixture (Abraham et al 2011) or k-distributions

(Stanton and Chu 2010). The work shown in this chapter suggests a distribution not previously considered in the literature, which is an integral of the product of a weighting function and a Rayleigh distribution for varying means (6-4). There are still many directions and developments that can come from it. Thus far, while there have been a several distributions of interest to describe the backscattered normalized echo amplitude of the probability distribution function, a specific connection of the measured distributions to the fish school behavior has yet to be considered (Stanton and Chu, 2010, Lee and Stanton, 2014, Lee and Stanton 2016). The work presented in this chapter is the first which starts to consider the contribution of the natural variability of the school of interest. Chapter 7 highlights some more of the future directions this study can go in and summarizes this chapter along with the findings discussed in the rest of this thesis.

CHAPTER 7

Summary and Conclusions

This chapter reiterates the findings from each of the previous chapters and summarizes some of the conclusions discussed in Chapters 3-6. It will also propose and suggest some future directions the work in this thesis can go in and some of the expected challenges which would need to be overcome based on the work documented in this thesis.

7-1: Summary

When sound is projected into the ocean, the backscattered signal may provide information about the object(s) from which the sound is scattered. When the backscattered sound comes from an aggregation of strong scatterers, such as a school of fish at their swimbladder resonant frequency, a phenomenon called the Coherent Backscatter Enhancement (CBE) occurs, and this phenomenon could aid in discriminating fish schools from other similar-strength scatterers in the ocean water column. This phenomenon is studied in this thesis to determine under which conditions a strong CBE peak occurs and the backscattered mean squared pressure is compared with the backscattered pressure magnitude squared of an idealized object, modeled as spheres in this thesis. Additionally, the use of a probability distribution function is also considered to gather statistical information on the backscattered amplitude from an aggregation

of scatterers. The normalized echo amplitude distribution from an aggregation of scatterers is compared with that of actual fish schools.

It has been shown that coherent backscatter enhancement can be simulated both in the near and far fields of random aggregations of omnidirectional point scatterers. The scattering from the fish schools were modeled through the use of the Foldy (1945) equations, which are applicable for fish with an effective swimbladder size, a_s, that are illuminated by an incident wave, with wave number, k, when $ka_s << 1$. Comparisons of the scattering were made with idealized spheres considered in van Bladel (1968) and in Hahn (2007).

In addition, coherent backscatter enhancement from aggregations of omnidirectional point scatterers can be simulated using single frequencies and frequency sweeps. Since a frequency sweep is composed of single frequency signals, the results obtained from single frequency signals are also applicable when considering broadband pulses as long as the length scales are adjusted accordingly.

To discriminate the backscatter returns fish schools against other isolated objects present in the ocean, the probability distribution function of the normalized echo amplitude or magnitude pressure squared from an aggregation of scatterers or a fish school is considered. The backscattered probability distribution function for a simulated aggregation of omnidirectional point scatterers is a Rayleigh distribution. For actual fish schools, the backscattered probability distribution function is a smeared Rayleigh distribution. Although there is not an exact or approximate reasoning that justifies the Lorentzian to be the weighting function, it has been used primarily for convenience, thereby resulting in a continuous sum of weighted Rayleigh distributions with varying means.

7-2: Conclusions

Several very important conclusions are arrived at from the chapters in this thesis which have already been mentioned at the end of each chapter, but are summarized here in the table below.

Table 7-1: Overall conclusions from each of the chapters in this thesis

Conclusion Number	Conclusion	Chapter	Figures	Tables
1	An aggregation of omnidirectional point scatterers simulated via the Foldy (1945) equations conserve energy. • While Foldy's paper showed the conservation of energy for a single omnidirectional point scatterer, the dissertation extends it to show the same for an aggregation of point scatterers with negligible amount of error	3	3-6	3-1, 3-2
2	The Foldy (1945) equations can be used to simulate the coherent backscatter enhancement under the following conditions: • dimensionless scattering strength of an individual scatterer is high • wave number scaled spacing between scatterers is small • sufficient number of scatterers • In the far field, the CBE peak is also more prominent when the aggregation is bigger in size.	3, 4	3-13, 4-6, 4-10, 4-11, 4-12, 4-13, 4-14	
3	Existing optics and acoustics CBE experiments can be replicated using simulation. • Wolf et al 1988 and Bayer Niederdrank 1993 experiments were replicated	3	3-8, 3-10, 3-11, 3-12	
4	In the near field, the CBE peak height increases with increasing $(k^2\sigma_s)^{1/4}(ks)^{-1}$.	3	3-13	

	• An enhancement exceeding a factor of two was also shown in the near field			
5	CBE can also be simulated and observed in the far field. • Due to a low Rayleigh far field parameter a simulation geometry involving a receiving ring was appropriate • For strong multiple scattering effects, a CBE peak emerged	4, 5	4-10, 4-11, 4-12, 5-2, 5-3, 5-7, 5-12, 5-17	4-1
6	In the far field, the peak width is dependent on the aggregation geometry.	4	4-9	
7	When comparing a spherical aggregation of scatterers with a single spherical scatterer by matching backscattered pressure magnitude square in the frequency domain, an overestimate of size may occur when the multiple scattering effects are strong.	4	4-13, 4-14	4-1
8	An aggregation of scatterers compares well with the Hahn (2007) sphere when the wave number scaled spacing is high and the dimensionless scattering strength is low, so that $\lvert 4\pi(kg_1)^2/(ks)^3\rvert << 1$. • As the multiple scattering effects increase, there is a significant difference in the magnitude pressure from the Hahn (2007) sphere and the magnitude average pressure from simulating the aggregation of scatterers. This occurs because $\lvert 4\pi(kg_1)^2/(ks)^3\rvert$ approaches 1 (Frisch, 1968).	4	4-15	
9	When considering broadband pulses, the CBE peak is dependent on the same parameters (ks, ka and $k\sigma_s^{1/2}$) as when considering simulations of CBE using single frequency signals.	5	5-7, 5-12, 5-17	
10	When considering the time dependence of the backscattered mean square pressure of the aggregation of scatterers, there are several features that are different from the	5	5-3-5-17	

	backscattered pressure magnitude squared of an idealized sphere. These differences can be obtained from a single realization, 64 realizations and thousands of realizations.			
11	A herring fish school can be simulated in the free space and does exhibit CBE, if enough samples and angles are considered. The depth of the fish school also plays a role in the strength of the multiple scattering effects. • Three different depths in the pelagic zone (60m, 236m and 430m) were simulated at different frequencies surrounding the resonance peak • The CBE peak was widest and least prominent at 60m depth and narrowest and most prominent at 430m depth.	5	5-7, 5-12, 5-17	
12	The returns from a school of fish are very different from that of a single spherical scatterer of the same size. • Peak corresponding to the time of the resonant frequency is the distinguishing feature. • The time dependent signal is slightly longer for the school of fish which is not present in the spherical scatterer. • When considering the angular dependence, CBE may occur for strong multiple scattering effects.	4, 5	5-5-5-17	4-1
13	Regardless of dimensionless spacing, aggregation size and scatterer strength, via simulation, the distribution is always Rayleigh or extreme value, depending on the normalization, as long as the scattering parameters are consistent over all the realizations. • The use of the distribution can be another way to classify an aggregation of scatterers from a single scattering object and may	6	6-5	

	be a more robust method for classification, especially since the distribution is always the same regardless of the strength of the multiple scattering.			
14	In contrast to simulation, the distribution of the backscattered pressure amplitude for *in situ* measurements can best be fitted using a continuous sum of Lorentzian weighted Rayleigh distributions for varying means for the fish schools considered. Using this distribution commentary may also be provided on the homogeneity of the fish school.	6		6-3, 6-10, 6-11, 6-12
15	Observing a CBE peak is not a robust alternative to existing conventional methods based on backscatter statistics for the task of remotely discriminating between an aggregation of scatterers and single isolated scatterer • Many backscatter samples are needed over an extended angular range to observe a CBE peak	4,6	4-10, 4-11, 4-12	6-1

7-3: Future Work

The research presented in this thesis is about the utility of the coherent backscatter enhancement and the probability distribution function of the backscattered returns for remote aggregation-vs.-single-object discrimination in active sonar scenarios. Most of the results have been presented in the form of feasibility studies conducted via simulation and many of these simulations were limited by runtime. Therefore, the conclusions in this dissertation are based on what was computationally feasible and could be completed in a timely fashion. Therefore, there are many directions that the future work can take.

The possible problem statements are summarized in bullets in bold and are briefly discussed:

- **Broadband Near Field CBE**

The primary aim of this thesis was to simulate the coherent backscatter enhancement with sufficient fidelity so that its likely utility for remote aggregation-vs.-single-object discrimination in active sonar scenarios could be assessed. As a result, much of the analysis has been focused on far field scattering. However, near field CBE has been of interest in optics (Akkermans et al. 1986) and ultrasound applications (Aubry et al. 2007). While experimental studies have been done with broadband, near field CBE, simulation studies, particularly with the Foldy (1945) equations have yet to be considered or explored. Additionally, simulation studies involving optics have been few so this may be an area which could be of interest in optics and ultrasound.

- **Adding other anatomical features of the fish**

Reeder et al. (2004) found that the swimbladder and skull yields the most scattering from the fish. This thesis only considered the swimbladder as the contributing factor of the fish school. If both the swimbladder and skull are considered together, it may be that fewer realizations may be necessary to get a peak and the scattering may be stronger for a distinct CBE peak. In this case, however, the Foldy (1945) equations may not suffice since they assume omnidirectional point scatterers. Alternatively, finite element or more complex boundary element techniques may be needed which are likely more time consuming than the currently-required N by N matrix inversion. In practice, adding more anatomical features of the fish would provide a better representation of the scattering from fish schools.

- **Inclusion of the fluid-structure interactions instead of the van Bladel (1968) or Hahn (2007) spheres**

In this thesis, the hard, soft and Hahn (2007) spheres are idealized and their scattering characteristics are computed from standard textbook formulae (Morse and Ingard, 1968) due to its relative simplicity for evaluation. In practice, however, the mechanics of an actual sphere in the ocean would have static pressure effects involving expansion and contraction due to variations in depth. Better models for the spheres would include these fluid-structure interactions and might change the backscatter returned pressure magnitude squared for the soft and hard spheres. However, for simplicity, such complex interactions were not considered in this thesis.

- **Inclusion of the ocean waveguide into the simulations**

In this thesis, it was assumed that a downward looking echosounder need only consider direct path propagation. However, in reality, active sonar systems are commonly horizontal looking and the ocean water column includes many complications: plant life, bottom and surface roughness, along with other fish and marine life. Adding these features may impact the strength or width, if applicable, of the peak. Inclusion of the ocean waveguide would further increase the run time of the simulations which is why it was not considered in this thesis.

- **Improvement of the simulation runtime**

In this project, a major limitation for the simulations has been the runtime. While the codes were optimized to the author's ability to produce results in a reasonable duration, there have definitely been instances where shorter runtimes were needed, especially when considering broadband pulses. For fully converged results, broadband simulations took approximately 8-10 months on the supercomputing cluster (Flux) provided by the Advanced

Research Computing group at the University of Michigan. If the runtime can be further improved either via a different programming language or through parallelization, additional simulations could be considered, particularly with many scatterers or larger aggregations, with different waveforms as the illuminating signal or through inclusion of an ocean waveguide.

- **Additional Far Field Broadband CBE Studies**

If more simulations of broadband CBE could be performed, the parametric scalings considered in Chapters 3 and 4 could be further improved to include depth of the fish school. Additionally, if high resolution receivers can be considered, analysis of the impact of the slightly longer signal could be considered. This was briefly explored, but it was determined that for the resolutions considered for the receivers, it was computationally infeasible to simulate or study further. Additionally, it was also observed that the fluctuations in cross correlation of the original signal with the scattered signal seemed to increase with the number of scatterers. Lastly, while the work in this thesis considered scattering from herring fish schools, other schools could certainly be considered.

- **Impact of the scattering from scatterers with different strengths**

Here, a primary assumption was that all the scatterers composing the aggregation have the same dimensionless scattering strengths. However, in reality, an aggregation may have scatterers with different strengths (i.e. fish in a school may be of different sizes or have different swim bladder sizes). While this was considered at the very beginning of this project, ultimately, this was not explored very thoroughly and this change could impact the

prominence of the CBE peak, parametric scalings, and the echo statistics distribution, even, may no longer be Rayleigh.

- **More detailed investigations on the impact of geometry of the aggregation on the prominence of the CBE peak**

In Chapter 4, aggregations which are realistic to fish schools, particularly spheres and spheroids (Partridge, 1980) were considered. However, when simulating the rectangular aggregation, there were definite differences in the appearance of the CBE peak strength and width. Additionally, when the aggregation was rotated, there were peaks present at angles other than in the backscatter direction. This was attributed to edge effects, but the importance of the edge effects on the CBE peak was not thoroughly explored. Additionally, it was assumed that the aggregation is perfectly spherical or spheroidal with no changes in the shape over the realizations. In actual fish schools, the geometry may change slightly.

- **Consideration of Other Fish Schools**

In Chapter 6, the *in situ* data obtained were for rockfish and small pelagic fish schools. Therefore, the distributions considered to model the fish schools are specific to rockfish and small pelagics. If more types of fish schools were considered, while the Rayleigh distribution portion of the function may be the same, the weighting function, $A(\langle\psi\rangle)$ and the maximum mean, $\langle\psi\rangle_{max}$, may change and be no longer set to two.

- **Biological Relevance of the Parameters Considered**

In Chapter 6, the smeared Rayleigh distribution was utilized with a weighting function, $A(\langle\psi\rangle)$, which was a Lorentzian function. The role of the weighting function was to

separately distinguish the natural variability of fish schools in the ocean's water column from other objects in the ocean.

This smeared distribution function is a new function considered for the probability distribution function of the backscattered normalized pressure magnitude. This is the first distribution function considered thus far which may provide insight into the statistical homogeneity of the fish schools. However, biological implications or interpretation of the parameters b, $\langle\psi\rangle_{min}$ and $\langle\psi\rangle_{max}$, and a scientific rationale of selecting the Lorentzian are still unknown. These specifics of connecting the distribution with the fish schooling behavior has not yet been considered previously in the echo statistics modeling literature, though estimating of the density of a fish school from the backscattered probability distribution function has been studied (Chu and Stanton, 2010, Lee and Stanton, 2014). Therefore, additional work in this area might strengthen the utility of the smeared Rayleigh distribution, giving a more representative model for the fish school.

- **Extensions to other fields and applications**

While use of the probability distribution functions of the backscattering from fish schools has been widely used in fish school classification, this tool may also be explored and analyzed in optics, ultrasound or other applications where the coherent backscatter enhancement was considered. It would be interesting to see if the probability distribution function stemming from the sample considered in Wolf et al. (1988) or Aubry et al. (2007) also produces a Rayleigh distribution since the setup is more controlled compared to the fish school in the water column. Additionally, radar applications involving flocks of birds or other objects as the scattering medium may also be of interest and could even provide a

stronger comparison with the simulation results using the Foldy (1945) equations for the frequencies of interest.

APPENDIX A

Fundamental Equations of Acoustics

The fundamental equations in acoustics consist of the lossless linearized equations, representing conservation of mass (A-1), conservation of momentum (A-2), conservation of energy (A-3) and the constitutive relations (A-4), where $p(\vec{r},t)$ = acoustic pressure at a point, c_o = speed of sound, t = time, ρ_o = density at a point, $\vec{u}(\vec{r},t)$ = particle velocity of a fluid element, γ = ratio of specific heats, R_g = gas constant, P_o = ambient pressure at a point, T_o = ambient absolute temperature at a point, determined by the ideal gas law, $T'(\vec{r},t)$ = temperature fluctuation, c_v = specific heat with constant volume, $\rho'(\vec{r},t)$ = density fluctuation, $\vec{u}'(\vec{r},t)$ = velocity fluctuation, $e'(\vec{r},t)$ = specific energy, $\dot{M}(\vec{r},t)$ = rate of mass addition per unit volume, $\vec{F}(\vec{r},t)$ = force per unit mass applied to the fluid and $\dot{E}(\vec{r},t)$ = rate of energy addition per unit mass. Here the molecular transport coefficients as assumed to be too small to consider, while the forcing terms on the right sides of (A-1), (A-2) and (A-3) serve as idealizations of real physical processes that may lead to acoustic waves.

$$\frac{\partial \rho'(\vec{r},t)}{\partial t} + \rho_o \vec{\nabla} \cdot \vec{u}'(\vec{r},t) = \dot{M}(\vec{r},t) \tag{A-1}$$

$$\rho_o \frac{\partial \vec{u}'(\vec{r},t)}{\partial t} + \vec{\nabla} p(\vec{r},t) = \rho_o \vec{F}(\vec{r},t) \tag{A-2}$$

$$\rho_o \frac{\partial e'(\vec{r},t)}{\partial t} + P_o \vec{\nabla} \cdot \vec{u}'(\vec{r},t) = \rho_o \dot{E}(\vec{r},t) \tag{A-3}$$

$$\begin{aligned} e'(\vec{r},t) &= c_v T'(\vec{r},t) \\ c_o^2 &= \gamma R_g T_o = \gamma \frac{P_o}{\rho_o} \\ p(\vec{r},t) &= \rho_o R_g T'(\vec{r},t) + R_g T_o \rho'(\vec{r},t) \end{aligned} \tag{A-4}$$

Through algebraic manipulation and cross differentiation of (A-1)-(A-4), the following forced acoustic wave equation in the time domain may be deduced:

$$\nabla^2 p(\vec{r},t) - \frac{1}{c_o^2} \frac{\partial^2 p(\vec{r},t)}{\partial t^2} = -\frac{1}{\gamma} \frac{\partial \dot{M}(\vec{r},t)}{\partial t} - \frac{(\gamma - 1)\rho_o}{c_o^2} \frac{\partial \dot{E}(\vec{r},t)}{\partial t} + \rho_o \vec{\nabla} \cdot \vec{F}(\vec{r},t) \tag{A-5}$$

The forcing (right hand side) terms in (A-5) can be expressed by a function $q(\vec{r},t)$. When (A-5) is transformed from the time domain to the frequency domain using the Fourier transform definitions discussed in Chapter 2, the forced Helmholtz equation (A-6) results.

$$\nabla^2 p(\vec{r},\omega) + k^2 p(\vec{r},\omega) = -q(\vec{r},\omega) \tag{A-6}$$

Here, $p(\vec{r},\omega)$ = pressure in the frequency domain, $k = \omega / c_o$ = acoustic wave number and $q(\vec{r},\omega)$ = source terms in the frequency domain (the Fourier transform of the source terms in (A-5)). The Foldy equations discussed in Chapter 2 are a direct solution to (A-6) with $q(\vec{r},\omega) = 0$.

APPENDIX B

The Scattering Coefficient and Its Role in Acoustic Energy Conservation

The definition of the scattering coefficient, g_1, (shown in Chapter 2) is to ensure that energy is conserved. This is done by having both a real and imaginary part for g_1. This is not readily obvious from Foldy's (1945) paper, but is implicit in evaluating the multiple scattering equations when selecting values for the dimensionless scattering strength, $k\sqrt{\sigma_s}$. Therefore, Appendix B will show the problem set up and derivation of the scattering coefficient. Additionally, it will also discuss the limitations in the selection of the dimensionless scattering strength and explain why any arbitrary value cannot be selected for the dimensionless scattering strength.

B-1: Problem Setup and Geometry

In order to derive the scattering coefficient, g_1, a single scatterer and an incident harmonic plane wave with wave number $\vec{k}$ is considered. For simplicity, unlike in the rest of the thesis, the incident wave is traveling along the $+kz$ axis and the listening location is at the origin. The scatterer, designated as a black dot, is located at the position

$(kr\sin(\theta)\cos(\varphi), kr\sin(\theta)\sin(\varphi), kr\cos(\theta))$, in spherical coordinates based on Figure B-1. Additionally, the polar angle is defined as θ with respect to the *kz* axis and the azimuthal angle is defined as φ with respect to the *kx* axis. The location *kr* is the radial position for the single scatterer.

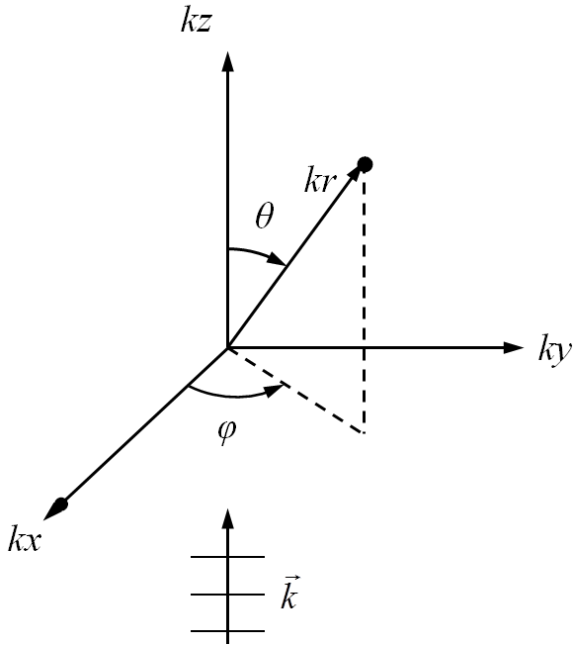

Figure B-1: Problem geometry used to derive the scattering coefficient

The pressure field from the incident plane wave interacting with a single scatterer can be expressed as the sum of the incident pressure field and a spherical wave emanating from the single scatterer (B-1). Here, *A* is the amplitude of the incident plane wave and *B* is the complex amplitude from the spherical wave resulting from the plane wave interacting with the single scattterer.

$$p(\vec{r},\omega) = A\exp(-ikr\cos(\theta)) + B\frac{e^{-ikr}}{r} \tag{B-1}$$

Using (B-1), the velocity can be determined using (A-2) with $\vec{F}(\vec{r},t)=0$ as (B-2):

$$u_r(\vec{r},\omega)=\frac{A\cos(\theta)}{\rho_o c}e^{-ikr}+\frac{B}{\rho_o c}\left(1+\frac{1}{ikr}\right)\frac{e^{-ikr}}{r} \tag{B-2}$$

With (B-1) and (B-2), the radial intensity, I_r, can be determined using (B-3) where * denotes the complex conjugate:

$$I_r=\frac{1}{2}\mathrm{Re}\left([\,p(\vec{r},\omega)]^* u_r(\vec{r},\omega)\right) \tag{B-3}$$

The power, Π, can be calculated by taking an integral of (B-3) over a sphere as (B-4):

$$\Pi=\int_{sphere} I_r dA=2\pi r^2\int_{\theta=0}^{\pi} I_r\sin(\theta)d\theta \tag{B-4}$$

Using the formula for (B-4) and some additional algebraic manipulation, it is possible to show that in order for energy to be conserved ((B-4) = 0), that the definitions given by Foldy (1945) result, ultimately, yielding the definition for g_1. The next section will show the simplified result from (B-1)-(B-4) and the definitions given in Foldy's (1945) paper for the scattering terms.

B-2: Simplification and Foldy (1945) Definitions

After (B-1) and (B-2) have been considered in the formula for (B-4), the resulting simplified expression for (B-4) is listed as (B-5).

$$\Pi=4\pi\frac{|B|^2}{2\rho_o c}+4\pi\frac{A\,\mathrm{Im}(B)}{2\rho_o ck} \tag{B-5}$$

Thus far, the scatterer resembles a single point source. In order for this scatterer to have omndirectional point scattering properties, Foldy (1945) relates the amplitude of the spherical

wave *B* to the incident amplitude *A* via the scattering coefficient to be $B = g_1 A$. Simplifying (B-5) further gives (B-6):

$$\Pi = \frac{4\pi A^2 |g_1|^2}{2\rho_o c} + \frac{4\pi A^2 \,\mathrm{Im}(g_1)}{2\rho_o c k} \tag{B-6}$$

Dividing (B-6) by incident intensity gives the expression in Foldy (1945) as well:

$$\sigma_c = \frac{\Pi}{I_i} = 4\pi |g_1|^2 + \frac{4\pi}{k}\,\mathrm{Im}(g_1) \tag{B-7}$$

The first term in (B-7) is the scattering cross section, σ_s ($\sigma_s = 4\pi |g_1|^2$). In order to ensure that acoustic energy is conserved, the following system of equations can be expanded and solved:

$$\sigma_s + \frac{4\pi}{k}\,\mathrm{Im}(g_1) = 0 \tag{B-8}$$

$$\sigma_s = 4\pi\left([\mathrm{Re}(g_1)]^2 + [\mathrm{Im}(g_1)]^2\right) \tag{B-9}$$

Simplifying (B-8) and (B-9) yields the following two constraints for the real (B-10) and imaginary parts (B-11) of g_1:

$$\mathrm{Re}(g_1) = \sqrt{\frac{\sigma_s}{4\pi} - \frac{k^2 \sigma_s^2}{16\pi^2}} \tag{B-10}$$

$$\mathrm{Im}(g_1) = -\frac{k\sigma_s}{4\pi} \tag{B-11}$$

Therefore, in order for energy to be conserved both a real and imaginary part of g_1 need to exist. Consequently, the selection of values for *k* and σ_s needs to be carefully done so that the scattering coefficient is such that it is not purely imaginary since this would violate conservation

of energy for the point scatterer. The next section will discuss the constraints for the values and show why there is an upper bound in selecting a value for the dimensionless scattering strength for a point scatterer.

B-3: Limitations in the Foldy (1945) Equations

In the previous section, it was shown that the scattering coefficient needs to be a complex constant with both real and imaginary parts to ensure that energy is conserved. Thus, arbitrary selection of σ_s is not feasible since it can violate acoustic energy conservation. Additionally, since the scattering cross section is defined as $\sigma_s = 4\pi|g_1|^2$, it must be a positive, real number. Therefore, the scattering cross section needs to be greater than 0 and less than a maximum value, $(\sigma_s)_{\max}$ such that (B-10) is greater than 0. This maximum value is (B-12):

$$(\sigma_s)_{\max} = \frac{4\pi}{k^2} \tag{B-12}$$

or in terms of dimensionless scattering strength, $k\sqrt{\sigma_s}$:

$$k\sqrt{(\sigma_s)_{\max}} = 2\sqrt{\pi} \approx 3.5449 \tag{B-13}$$

Therefore, the Foldy (1945) equations can be used to simulate omnidirectional point scatterers which have dimensionless scattering strength $0 < k\sqrt{\sigma_s} < 2\sqrt{\pi}$. This constraint successfully ensures that energy is conserved for a single scatterer interacting with a harmonic incident plane wave. In Chapter 3, this is checked by simulation to ensure that simulations are implemented correctly and also expanded to check that that energy is still conserved for an

aggregation of scatterers interacting with a harmonic incident plane wave for dimensionless scattering strengths $k\sqrt{\sigma_s}$ = 0.21, 1 and 3.5.

Bibliography

Abraham, D.A.; Gelb, J.M.; Oldag, A.W.; Background and Clutter Mixture Distributions for Active Sonar Statistics. *IEEE J. Oceanic Eng*, 36 (2), 2011, 231-247.

Akkermans, E; Wolf, P.E.; Maynard, R.; Coherent Backscattering of Light by Disordered Media: Analysis of the Peak Line Shape. *Physical Review Letters*, 56 (14), 1986, 1471-1474.

Akkermans, E; Wolf, P.E.; Maynard, R.; Maret, G.; Theoretical study of the coherent backscattering of light by disordered media. *J. Phys. France*, 49, 1988, 77-98.

Alfaro, S.E.; Cellio, J.; Raveau, M. P.; Feuillade, C.; Low frequency scattering from dynamic fish schools based on collective animal behavior modeling. *Proceedings of Meetings on Acoustics*, 23, 2015, 1-9.

Andrews, M; Gong, Z.; Ratilal, P.; Effects of multiple scattering, attenuation and dispersion in waveguide sensing of fish. *J. Acoust. Soc. Am.*, 130 (3), 2011, 1253-1271.

Aubry, A.; Derode, A.; Roux, P.; Tourin, A.; Coherent backscattering and far-field beamforming in acoustics. *J. Acoust. Soc. Am.*, 121 (1), 2007, 70-77.

Bayer, G.; Niederdränk, T.; Weak Localization of Acoustic Waves in Strongly Scattering Media. *Physical Review Letters*, 70 (25), 1993, 3884-3887.

Benoit-Bird, K.J.; McIntosh, N.E.; Heppell, S. A.; Nested scaled of spatial heterogeneity in juvenile walleye pollock Theragra chalcogramma in the southeastern Bering Sea. *Mar Ecol Prog Ser.*, 484, 2013, 219-238.

Benoit-Bird, K.J.; Lawson, G.L.; Ecological Insights from Pelagic Habitats Acquired Using Active Acoustic Techniques. *Annu. Rev. Mar. Sci.* 8, 2016, 463-490.

Billingsley, P.; Probability and Measure. *John Wiley & Sons*, 3, 1995, 182-185.

Bragg, W.L.; The Structure of Some Crystals as Indicated by Their Diffraction of X-rays. *Proc. R. Soc. Lond. A*, 89, 1913, 248-277.

Catheline, S.; Gallot, T.; Roux, P.; Ribay, G.; de Rosny, J.; Coherent backscattering

enhancement in cavities The simple-shape cavity revisited. *Wave Motion*, 48, 2011, 214-222.

Charef, A.; Ohshimo, S.; Aoki, I.; Al Absi, N.; Classification of fish schools based on evaluation of acoustic descriptor characteristics. *Fish Sci*., 76, 2010, 1-11.

Chu, D.; Stanton, T.K.; Statistics of Echoes From a Directional Sonar Beam Insonifying Finite Numbers of Single Scatterers and Patches of Scatterers. *IEEE Journal of Oceanic Engineering*, 35 (2), 2010, 267-277.

Costello, M.J.; Cheung, A.; De Hauwere, N.; Surface Area and the Seabed Area, Volume, Depth, Slope and Topographic Variation of the World's Seas, Oceans and Countries. *Environ. Sci. Technol*, 44, 2010, 44, 8821-8828.

de Hoop, M.V.; Garnier, J.; Solna, K.; Enhanced and specular backscattering in random media. *Waves in Random and Complex Media*, 22 (4), 2012, 505-530.

Demer, D.A.; Cutter, G.R.; Renfree, J.S.; Butler, J.L.; A statistical-spectral method for echo classification, *ICES Journal of Marine Science*, 66, 2009, 1081-1090.

Derode, A.; Mamou, V.; Padilla, F.; Jenson, F.; Laugier, P.; Dynamic coherent backscattering in a heterogeneous absorbing medium: Application to human trabecular bone characterization, *Appl. Phys. Lett.* 87 (114101), 2005, 114101-1-114101-3.

Derode, A.; Mamou, V.; Tourin, A.; Influence of correlations between scatterers on the attenuation of the coherent wave in a random medium, *Physical Review E*, 74, 2006, 036606-1-036606-8.

Devin Jr., C.; Survey of Thermal, Radiation and Viscous Damping of Pulsating Air Bubbles in Water, *The Journal of the Acoustical Society of America*, 31 (12), 1959, 1654-1667.

Eddowes, M.H.; Millis, T.N.; Delpy, D.T.; Monte Carlo simulations of coherent backscatter for identification of the optical coefficients of biological tissues in vivo, *Applied Optics*, 34 (13), 1995, 2261-2267.

Fässler, S.M.M.; Gorska, N.; Ona, E.; Fernandes, P.G.; Differences in swimbladder volume between Baltic and Norwegian spring-spawning herring: Consequences for mean target strength, *Fisheries Research*, 92(2-3), 2008, 314-321.

Feuillade, C.; Scattering from collective modes of air bubbles in water and the physical mechanism of superresonances, *J. Acoust. Soc. Am.*, 98 (2), 1995, 1178-1190.

Feuillade, C.; Nero, R.W.; Love, R.H.; A low-frequency acoustic scattering model for small schools of fish, *J. Acoust. Soc. Am.*, 99 (1), 1996, 196-208.

Foldy, L.L.; The Multiple Scattering of Waves I. General Theory of Isotropic Scattering by Randomly Distributed Scatterers, *Physical Review*, 67 (3, 4), 1945, 107-119.

Foote, K.G.; Importance of the swimbladder in acoustic scattering by fish: A comparison of gadoid and mackerel target strengths, *J. Acoust. Soc. Am.*, 67 (6), 1980, 2084-2069.

Foote, K.G.; Averaging of fish target strength functions, *J. Acoust. Soc. Am.*, 67 (2), 1980, 504-515.

Foote, K.G.; Rather-high-frequency sound scattering by swimbladdered fish, *J. Acoust. Soc. Am.*, 78 (2), 1985, 688-700.

Frisch, U.; Wave Propagation in Random Media. *Probabilistic Methods in Applied Mathematics Applied Press, Inc.* 1, 1968, 75-198.

Froese; Rainer; Pauly, D.; Opisthonema berlangai. *Fishbase*, 2012.

Gallot, T.; Catheline, S.; Roux, P.; Coherent backscattering enhancement in cavities. Highlights of the role of symmetry, *J. Acoust. Soc. Am.*, 129 (4), 2011, 1963-1971.

Garnier, J.; Sølna, K.; Effective Transport Equations and Enhanced Backscattering in Random Waveguides, *SIAM J. Appl. Math.*, 68 (6), 2008, 1574-1599.

Gauthier, S.; Rose, G.A.; Target Strength of encaged Atlantic redfish (Sebastes spp.), *ICES Journal of Marine Science*, 58, 2001, 562-568.

Gorska, N.; Ona, E.; Modelling the effect of swimbladder compressing on the acoustic backscattering from herring at normal or near-normal dorsal incidences, *ICES Journal of Marine Science*, 60, 2003, 1381-1391.

Hahn, T.R.; Low frequency sound scattering from spherical assemblages of bubbles using effective medium theory, *J. Acoust. Soc. Am.*, 122 (6), 2007, 3252-3267.

Hay, A. E.; Burling, R.W.; On sound scattering and attenuation in suspensions, with marine applications, *J. Acoust. Soc. Am.*, 72 (3), 1982, 950-959.

Hemelrijk, C. K.; Hildenbrandt, H.; Schools of fish and flocks of birds: their shape and internal structure by self-organization, *Interface Focus*, 2, 2012, 726-737.

Henyey, F.S.; Corrections to Foldy's effective medium theory for propagation bubble clouds and other collections of very small scatterers, *J. Acoust. Soc. Am.*, 105 (4), 1999, 2149-2154.

Huang, K.; Clay, C.S.; Backscattering cross sections of live fish: PDF and aspect, *J. Acoust. Soc. Am.*, 67 (3), 1980, 795-802.

Hwang, P.A.; Teague, W.J.; Low-Frequency Resonant Scattering of Bubble Clouds, *Journal of Atmospheric and Oceanic Technology*, 17, 847-853.

Jaffe, J.; Using multi-angle scattered sound to size fish swimbladders, *ICES Journal of Marine*

Science, 64, 2006, 1397-1404.

Jain, A. D.; Ignisca, A.; Yi, D. H; Ratilal, P.; Makris, N.C.; Feasibility of Ocean Acoustic Waveguide Remote Sensing (OAWRS) of Atlantic Cod with Seafloor Scattering Limitations, *Remote Sens.*, 6, 2014, 180-208.

Jendrzejewski, F.; Müller, K.; Richard, J.; Date, A.; Plisson, T.; Bouyer, P.; Aspect, A.; Josse, V.; Coherent Backscattering of Ultracold Atoms, *Physical Review Letters*., 109 (19), 2012, 1-5.

Jensen, F.B.; Kuperman, W.A.; Porter, M.B.; Schmidt, H.; Computational Ocean Acoustics, *Springer Science+Business Media, LLC*, 2, 2011, 714-724.

Jones, B.A.; Colosi, J.A.; Stanton, T.K; Echo statistics of individual and aggregations of scatterers in the water column of a random, oceanic waveguide, *J. Acoust. Soc. Am.*, 136 (1), 2014, 90-108.

Jørgensen, R.; The effects of swimbladder size, condition and gonads on the acoustic target strength of mature capelin, *ICES Journal of Marine Science*, 60, 2003, 1056-1062.

Kang, M.; Furusawa, M.; Miyashita, K.; Effective and accurate use of difference in mean volume backscattering strength to identify fish and plankton, *ICES Journal of Marine Science*, 59, 2002, 794-804.

Kinsler, L.E.; Frey, A.R.; Coppens, A.B.; Sanders, J.V.; Fundamentals of Acoustics, John Wiley & Sons, Inc., 4, 2000, 238-241.

Kirkup, S.M.; The Boundary Element Method in Acoustics. *Integrated Sound Software*, 2, 2007, 32-42.

Korneliussen, R.J.; Ona, E.; Synthetic echograms generated from the relative frequency response, *ICES Journal of Marine Sciences*. 60(3), 636-640.

Kuga, Y.; Ishimaru, A.; Retroreflectance from a dense distribution of spherical particles, *J. Opt. Soc. Am. A.* 1 (8), 1984, 831-835.

Larose, E.; Margerin, L.; van Tiggelen, B. A.; Campillo, M.; Weak Localization of Seismic Waves, *Physical Review Letters*. 93 (4), 2004, 048501-1-048501-4.

Larose, E.; Lobkis, O.I.; Weaver, R.L.; Coherent backscattering of ultrasound without a source, *Europhysics Letters*, 76, 2007, 1-6.

Lawless, J.F.; Statistical Models and Methods for Lifetime Data. *Wiley Series and Probability and Statistics*, 2, 2003, 20-23.

Lax, M.; Multiple Scattering of Waves, *Reviews of Modern Physics*. 23 (4), 1951, 287-310.

Lax, M.; Multiple Scattering of Waves. II. The Effective Field in Dense Systems, *Physical Review*. 85 (4), 1952, 621-629.

Lee, W.-J.; Stanton, T.K.; Statistics of Echoes from Mixed Assemblages of Scatterers With Different Scattering Amplitudes and Numerical Densities, *IEEE Journal of Oceanic Engineering*. 39(4), 2014, 740-754.

Lee, W.-J.; Stanton, T.K.; Statistics of Broadband Echoes: Application to Acoustic Estimates of Numerical Density Fish, *IEEE Journal of Oceanic Engineering*. 41(3) 2016, 709-723.

Linton, C.M.; Martin, P.A.; Multiple Scattering By Multiple Spheres: A New Proof of the Lloyd-Berry Formula For The Effective Wavenumber, *SIAM J. Appl. Math.* 66 (5), 2006, 1649-1668.

Lobkis, O. I.; Weaver, R.L.; Anderson localization of ultrasound in plates: Further experimental results, *J. Acoust. Soc. Am.*, 124 (6), 2008, 3528-3533.

Love, R. H.; Resonant acoustic scattering by swimbladder-bearing fish, *J. Acoust. Soc. Am.*, 64 (2), 1978, 571-580.

Lurton, X.; An Introduction to Underwater Acoustics, *Science*, 2002, 1-5.

Machias, A.; Tsimenides, N.; Biological factors affecting the swimbladder volume of sardine (Sardina pilchardus), *Marine Biology*, 123, 1995, 859-867.

MacLennan, D.N.; Menz, A.; Interpretation of *in situ* target-strength data, *ICES Journal of Marine Science*, 53, 1996, 233-236.

MacLennan, D.N.; Fernandes, P.G.; Dalen, J.; A consistent approach to definitions and symbols in fisheries acoustics, *ICES Journal of Marine Science*, 59, 2002, 365-369.

Makris, N.C.; Jagannathan, S.; Ignisca, A.; Box 11 Ocean Acoustic Waveguide Remote Sensing: Visualizing Life Around Seamounts, *Oceanography*, 23(1), 2010, 204-205.

Margerin, L.; Campillo, M.; van Tiggelen, B.A.; Coherent backscattering of acoustic waves in the near field, *Geophys. J. Int.*, 145, 2001, 593-603.

McClatchie, S.; Ye, Z.; Target strength of an oily deep-water fish, orange roughy (Hoplostethus atlanticus) II. Modeling, *J. Acoust. Soc. Am.*, 107 (3), 2000, 1280-1285.

Melvin, G. D.; Cochrane, N. A.; Li Y.; Extraction and comparison of acoustic backscatter from a calibrated multi- and single-beam sonar, *ICES Journal of Marine Science*, 60, 2003, 669-677.

Misund, O.A.; Dynamics of moving masses: variability in packing density, shape and size among herring, sprat, and saithe schools, *ICES J. mar. Sci.*, 50, 1993, 145-160.

Minnaert, M.; XVI. On musical air-bubbles and the sounds of running water, *The London, Edinburgh, and Dublin Philosophical Magazine and Journal of Science*, 7, 1933, 235-248.

Miyashita, K.; Aoki, I.; Inagaki, T.; Swimming behaviour and target strength of isada krill (Euphausia pacifica), *ICES Journal of Marine Science*, 53, 1996, 303-308.

Mookerjee, A.; Dowling, D. R.; Simulating acoustic coherent backscattering enhancement from random aggregations of omnidirectional scatterers. *The Journal of the Acoustical Society of America*, 138 (2), 2015, 758-768.

Morse, P.M.; Ingard, K.U.; Theoretical Acoustics. *McGraw Hill, Inc*., 1968, 418-441.

Moszynski, M.; Fish Target Strength Estimation Using Multiple Echo Statistics. *Acoustical Physics*, 48 (2), 2002, 201-208.

Myrberg Jr., A.A.; The effects of man-made noise on the behavior of marine animals. *Environment International*, 16(4-6), 1990, 575-586.

Nero, R.W.; *Model Estimates of Acoustic Scattering from Schools of Large Yellowfin Tuna*. Report NRL/MR/774-95-7708. Stennis Space Center, MS: Naval Research Laboratory, Ocean Acoustics Branch, Acoustics Division, 1996, 1-21.

NOAA Fisheries.; What are pelagic fish?. *National Ocean Service*. National Oceanic and Atmospheric Administration. US Department of Commerce, 2014, 1.

Norris, A.N.; Conoir, J-M.; Multiple scattering by cylinders immersed in fluid: High order approximations for the effective wavenumbers. *J. Acoust. Soc. Am*., 129 (1), 2011, 104-113.

Papoulis, A.; Probability, Random Variables and Stochastic Processes. *McGraw-Hill Series in Electrical Engineering*, 3, 1991, 73-83.

Partridge, B.L.; Pitcher, T.; Cullen, J.M.; Wilson, J.; The Three Dimensional Structure of Fish Schools. *Behav. Ecol. Sociobiol.*, 6, 1980, 277-288.

Partridge, B.L.; The Structure and Function of Fish Schools. *Scientific American, Inc.*, 1982, 114-123.

Picard, G.; Toan, T.L.; Mattia, F.; Gatti, A.-M.; Posa, F.; D'alessio, A.; Notarnicola, C.; Sabatelli, E.; A Backscatter Model for Wheat Canopies. Comparison with C-Band Multiparameter Scatterometer Measurements. *European Space Agency*. 2002, 291-296.

Pierce, A.D.; Acoustics. *Acoustical Society of America*, 1989, 435-439.

Pitcher, T.J.; Functions of Shoaling Behaviour in Teleosts. *The Behavior of Teleost Fishes*, 1993, 294-297.

Proni, J.; Stamates, J.; Carsey, T.; Zhang, J.-Z.; Sinigalliano, C.; Sullivan, K.; Acoustic methods for water mass delineation in coastal marine ecosystems. *Acoustics'08*, 2008, 1-6.

Raveau, M.; Feuillade, C.; Sound extinction by fish schools: Forward scattering theory and data analysis. *J. Acoust. Soc. Am.*, 137 (2), 2015, 539-555.

Raveau, M.; Feuillade, C.; Resonance scattering by fish schools: A comparison of two models. *J. Acoust. Soc. Am.*, 139 (1), 2016, 163-175.

Reeder, D.B.; Jech, J.M.; Stanton, T.K.; Broadband acoustic backscatter and high-resolution morphology of fish: Measurement and modeling. *J. Acoust. Soc. Am.*, 116 (2), 2004, 747-761.

Rice, J.A.; Mathematical Statistics and Data Analysis. *Thomson Brooks/Cole*, 3, 2010, 181-184.

Sabra, K.G.; Coherent backscattering effect from mid-frequency shallow water reverberation. *J. Acoust. Soc. Am.*, 127 (5), 2010, EL192-EL196.

Sakai, K.; Yamamoto, K.; Takagi, K.; Observation of acoustic coherent backscattering. *Physical Review B.*, 56 (17), 1997, 10930-10933.

Sargent,R.G.; Verification and Validation of Simulation Models. *Proceedings of the 2003 Winter Simulation Conference*. 2003, 37-48.

Schlesinger, S.; Crosbie, R.E.; Gagne, R.E.; Innis, G.S.; Lalwani, C.S.; Loch, J.; Sylvester, R.J.; Wright, R.D.; Kheir, N.; Bartos, D.; Terminology for model credibility. *Simulation*, 32(3), 103-104.

Simmonds, M.P.; Lopez-Jurado, L.F.; Whales and the military. *Nature Publishing Group*, 351, 1991, 448.

Singer, W.; Totzeck, M.; Gross, H.; Handbook of Optical Systems. *Wiley-VCH Verlag GmbH & Co. KGaA*, 2005, 360-363.

Smith, S.W.; The Scientist and Engineer's Guide to Digital Signal Processing. *California Technical Pub*, 1, 1997, 11-34.

Stanton, T.K.; Multiple scattering with applications to fish-echo processing. *J. Acoust. Soc. Am.*, 73 (4), 1983, 1164-1169.

Stanton, T.K.; Volume scattering: Echo peak PDF. *J. Acoust. Soc. Am.*, 77 (4), 1985, 1358-1366.

Stanton, T.K.; Sound scattering by cylinders of finite length. III. Deformed cylinders. *J. Acoust. Soc. Am.*, 86 (2), 1989, 691-705.

Stanton, T.K.; Chu, D.; Reeder, D.B.; Non-Rayleigh Acoustic Scattering Characteristics of Individual Fish and Zooplankton. *IEEE Journal of Oceanic Engineering*., 29 (2), 2004, 260-268.

Stanton, T.K.; Chu, D.; Non-Rayleigh Echoes from Resolved Individuals and Patches of Resonant Fish at 2-4kHz. *IEEE Journal of Oceanic Engineering*, 35 (2), 2010, 152-163.

Tourin, A.; Derode, A.; Roux, P.; van Tiggelen, B.A.; Fink, M.; Time-Dependent Coherent Backscattering of Acoustic Waves. *Physical Review Letters*, 79 (19), 1997, 3637-3639.

Towler, R.H.; Jech, J.M.; Horne, J.K.; Visualizing fish movement, behavior and acoustic backscatter. *Aquatic Living Resources*, 16, 2003, 277-282.

Tsang, L.; Kong, J.A.; Habashy, T.; Multiple scattering of acoustic waves by random distribution of discrete spherical scatterers with quasicrystalline and Percus-Yevick approximation. *J. Acoust. Soc. Am.*, 71 (3), 1982, 552-558.

Tsang, L.; Ding, K.-H.; Zhang, G.; Hsu, C.C.; Kong, J.A.; Backscattering Enhancement and Clustering Effects of Randomly Distributed Dielectric Cylinders Overlying a Dielectric Half Space Based on Monte-Carlo Simulations. *IEEE Transactions on Antennas and Propagation*, 43 (5), 1995, 488-499.

Turley, S.; Acoustic Scattering from a Sphere. *Brigham Young University*, 2006, 1-31.

Twersky, V.; On Scattering and Reflection of Sound by Rough Surfaces. *The Journal of the Acoustical Society of America*, 29 (2), 1957, 209-225.

Überall, H.; Acoustic scattering from elastic cylinders and spheres: surface waves (Watson transform) and transmitted waves. *Traitement du Signal*, 2 (5), 1985, 353-357.

Urick, R.J.; Principles of Underwater Sound. *Peninsula Pub*., 1996 (3).

Van Albada, M.P.; van der Mark, M.B.; Legendijk, A.; Observation of Weak Localization of Light in a Finite Slab: Anisotropy Effects and Light-Path Classification. *Physical Review Letters*, 58 (4), 1987, 361-364.

Van Albada, M.P.; van der Mark, M.B.; Lagendijk, A.; Polarisation effects in weak localisation of light. *J. Phys. D: Appl. Phys*., 21, 1988, S28-S31.

Van Bladel, J.; Low-Frequency Scattering by Hard and Soft Bodies. *The Journal of the Acoustical Society of America*, 44 (4), 1968, 1069-1073.

Walker, S.C.; Buckingham, M.J.; Spatial coherence and cross correlation of three-dimensional ambient noise fields in the ocean. *The Journal of the Acoustical Society of America*, 131(2), 2012, 1079-1086.

Waterman, P.C.; Truell, R.; Multiple Scattering of Waves. *Journal of Mathematical Physics*, 2 (4), 1961, 512-537.

Weaver, R.L.; Burkhardt, J.; Weak Anderson localization and enhanced backscatter in reverberation rooms and quantum dots. *J. Acoust. Soc. Am.*, 96 (5), 1994, 3186-3190.

Wolf, P.-E.; Maret, G.; Weak Localization and Coherent Backscattering of Photons in Disordered Media. *Physical Review Letters*, 55 (24), 1985, 2696-2699.

Wolf, P.E.; Maret, G.; Akkermans, E.; Maynard, R.; Optical coherent backscattering by random media: an experimental study. *J. Phys. France*., 49, 1988, 63-75.

Yasuma, H.; Sawada, K.; Ohshima, T.; Miyashita, K.; Aoki, I.; Target strength of mesopelagic lanternfishes (family Myctophidae) based on swimbladder morphology. *ICES Journal of Marine Science*, 60, 2003, 584-591.

Ye, Z.; Ding, L.; Acoustic dispersion and attenuation relations in bubbly mixture. *J. Acoust. Soc. Am.*, 98 (3), 1995, 1629-1633.

Ye, Z.; Curran, T.; Lemon, D.; Fish detection by the acoustic scintillation technique. *ICES Journal of Marine Science*. 53, 1996, 317-321.

Zhu, J-G.; Jiang, Y.; Stancil, D.D.; Moura, J.; A Novel Time Reversal Method for Target Detection in Cluttered Media. *IEEE Antennas and Propagation Society International Symposium*, 2005, 135-138.